EPJ manuscript No.
(will be inserted by the editor)

CERN-PH-EP-2011-117 Submitted to Eur. Phys. J. C

Electron performance measurements with the ATLAS detector using the 2010 LHC proton-proton collision data

The ATLAS Collaboration

Received: October 14, 2011 / Revised version: February 17, 2012

Abstract. Detailed measurements of the electron performance of the ATLAS detector at the LHC are reported, using decays of the Z, W and J/ψ particles. Data collected in 2010 at $\sqrt{s}$=7 TeV are used, corresponding to an integrated luminosity of almost 40 pb^{-1}. The inter-alignment of the inner detector and the electromagnetic calorimeter, the determination of the electron energy scale and resolution, and the performance in terms of response uniformity and linearity are discussed. The electron identification, reconstruction and trigger efficiencies, as well as the charge misidentification probability, are also presented.

1 Introduction

The precise determination of the electron performance of the ATLAS detector at the LHC is essential both for Standard Model measurements and for searches for Higgs bosons and other new phenomena. Physics processes of prime interest at the LHC are expected to produce electrons from a few GeV to several TeV. Many of them, such as Higgs-boson production, have small cross-sections and suffer from large background, typically from jets of hadrons. Therefore an excellent electron identification capability, with high efficiency and high jet rejection rate, is required over a broad energy range to overcome the low signal-to-background ratio. For example, in the moderate transverse energy region $E_{\mathrm{T}} = 20-50$ GeV a jet-rejection factor of about 10^5 is desirable to extract a pure signal of electrons above the residual background from jets faking electrons. In the central region up to $|\eta| < 2.5$, this challenge is faced by using a powerful combination of detector technologies: silicon detectors, a transition radiation tracker and a longitudinally layered electromagnetic calorimeter system with fine lateral segmentation.

A further strength of the ATLAS detector is its ability to reconstruct and identify electrons outside the tracking coverage up to $|\eta| < 4.9$. This brings several advantages. For example, it improves the sensitivity of the measurement of forward-backward asymmetry, and therefore the weak mixing angle, in $Z \to ee$ events, and it enlarges the geometrical acceptance of searches for Higgs bosons and other new particles.

To realize the full physics potential of the LHC, the electron energy and momentum must be precisely measured. Stringent requirements on the alignment and on the calibration of the calorimeter come, for example, from the goal of a high-precision W mass measurement.

This paper describes the measurements of the electron energy scale and resolution and of the efficiency to trigger, reconstruct and identify electrons using $Z \to ee$, $W \to e\nu$ and $J/\psi \to ee$ events observed in the data collected in 2010 at a centre-of-mass energy of $\sqrt{s} = 7$ TeV, corresponding to an integrated luminosity of almost 40 pb^{-1}. As the available statistics are significantly lower for isolated electrons from $J/\psi \to ee$ decays and these electrons are also more difficult to extract, only a subset of the measurements were performed in this channel.

The structure of the paper is the following. In Section 2, a brief reminder of the inner detector and calorimeter system is presented. The data and Monte Carlo (MC) samples used in this work are summarized in Section 3. Section 4 starts with the introduction of the trigger, reconstruction and identification algorithms and then proceeds by presenting the inclusive single and dielectron spectra in Subsection 4.5. The inter-alignment of the inner detector and the electromagnetic (EM) calorimeter is discussed in Subsection 4.6. The in-situ calibration of the electron energy scale is described in Section 5 followed by its performance in terms of resolution, linearity in energy, and uniformity in ϕ. The measurement of the electron selection efficiencies with the tag-and-probe technique is presented in Section 6. The identification efficiency determination is discussed in detail in Subsection 6.2, and the differences observed between data and MC predictions are attributed to imperfections of the MC description of the main discriminating variables. The reconstruction efficiency is reported in Subsection 6.4, followed by the charge misidentification probability in Subsection 6.5, and the trigger efficiency in Subsection 6.6. Conclusions and an outlook are given in Section 7.

2 The ATLAS detector

A complete description of the ATLAS detector is provided in Ref. [1].

ATLAS uses a right-handed coordinate system with its origin at the nominal pp interaction point at the centre of the detector. The positive x-axis is defined by the direction from the interaction point to the centre of the LHC ring, with the positive y-axis pointing upwards, while the beam direction defines the z-axis. The azimuthal angle ϕ is measured around the beam axis and the polar angle θ is the angle from the z-axis. The pseudorapidity is defined as $\eta = -\ln\tan(\theta/2)$.

The inner detector (ID) provides a precise reconstruction of tracks within $|\eta| < 2.5$. It consists of three layers of pixel detectors close to the beam-pipe, four layers of silicon microstrip detector modules with pairs of single-sided sensors glued back-to-back (SCT) providing eight hits per track at intermediate radii, and a transition radiation tracker (TRT) at the outer radii, providing about 35 hits per track (in the range $|\eta| < 2.0$). The TRT offers substantial discriminating power between electrons and charged hadrons over a wide energy range (between 0.5 and 100 GeV) via the detection of X-rays produced by transition radiation. The inner-most pixel vertexing layer (also called the *b-layer*) is located just outside the beam-pipe at a radius of 50 mm. It provides precision vertexing and significant rejection of photon conversions through the requirement that a track has a hit in this layer.

A thin superconducting solenoid, contributing 0.66 radiation length at normal incidence to the amount of passive material before the EM calorimeter, surrounds the inner detector and provides a 2 T magnetic field.

The electromagnetic calorimeter system is separated into two parts: a presampler detector and an EM calorimeter, a lead–liquid-argon (LAr) detector with accordion-shaped kapton electrodes and lead absorber plates. The EM calorimeter has three longitudinal layers (called *strip, middle* and *back* layers) and a fine segmentation in the lateral direction of the showers within the inner detector coverage. At high energy, most of the EM shower energy is collected in the middle layer which has a lateral granularity of 0.025×0.025 in $\eta \times \phi$ space. The first (strip) layer consists of finer-grained strips in the η-direction with a coarser granularity in ϕ. It offers discrimination against multiple photon showers (including excellent $\gamma - \pi^0$ separation), a precise estimation of the pseudorapidity of the impact point and, in combination with the middle layer, an estimation of the photon pointing direction [2]. These two layers are complemented by a presampler detector placed in front with a granularity of 0.025×0.1 covering only the range $|\eta| < 1.8$ to correct for energy lost in the material before the calorimeter, and by the back layer behind, which collects the energy deposited in the tail of very high energy EM showers. The transition region between the barrel (EMB) and endcap (EMEC) calorimeters, $1.37 < |\eta| < 1.52$, has a large amount of material in front of the first active calorimeter layer. The endcap EM calorimeters are divided into two wheels, the outer (EMEC-OW) and the inner (EMEC-IW) wheels covering the ranges $1.375 < |\eta| < 2.5$ and $2.5 < |\eta| < 3.2$, respectively.

Hadronic calorimeters with at least three longitudinal segments surround the EM calorimeter and are used in this context to reject hadronic jets. The forward calorimeters (FCal) cover the range $3.1 < |\eta| < 4.9$ and also have EM shower identification capabilities given their fine lateral granularity and longitudinal segmentation into three layers.

3 Data and Monte Carlo samples

The results are based on the proton-proton collision data collected with the ATLAS detector in 2010 at $\sqrt{s}$=7 TeV. After requiring good data-quality criteria, in particular those concerning the inner detector and the EM and hadronic calorimeters, the total integrated luminosity used for the measurements is between 35 and 40 pb^{-1} depending on the trigger requirements.

The measurements are compared to expectations from MC simulation. The $Z \to ee$, $J/\psi \to ee$ and $W \to e\nu$ MC samples were generated by `PYTHIA` [3] and processed through the full ATLAS detector simulation [4] based on `GEANT4` [5]. To study the effect of multiple proton-proton interactions different pile-up configurations with on average about two interactions per beam crossing were also simulated.

In addition, MC samples were produced with additional passive material in front of the EM calorimeter representing a conservative estimate of the possible increases in the material budget based on various studies using collision data, including studies of track reconstruction efficiency [6,7,8,9], the measurement of the photon conversion rate [10], studies of the energy flow in the EM calorimeter [11], EM shower-shape variables and the energy to momentum ratio. In these samples, the amounts of additional material with respect to the nominal geometry, expressed in units of radiation length (X_0) and given at normal incidence, are $0.05X_0$ in the inner detector, $0.2X_0$ in its services, $0.15X_0$ at the end of the SCT and TRT endcaps and at the ID endplate, $0.05X_0$ between barrel presampler detector and the strip layer of the EM calorimeter, and $0.1X_0$ in front of the LAr EM barrel calorimeter in the cryostat.

The distribution of material as a function of η in front of the presampler detector and the EM calorimeter is shown on the left of Figure 1 for the nominal and extra-material geometries. The contributions of the different detector elements up to the ID boundaries, including the services and thermal enclosures, are detailed on the right.

The peak in the amount of material before the electromagnetic calorimeter at $|\eta| \approx 1.5$, corresponding to the transition region between the barrel and endcap EM calorimeters, is due to the cryostats, the corner of the barrel electromagnetic calorimeter, the inner detector services and the tile scintillator. The sudden increase of material at $|\eta| \approx 3.2$, corresponding to the separation between the endcap calorimeters and the FCal, is mostly due to the

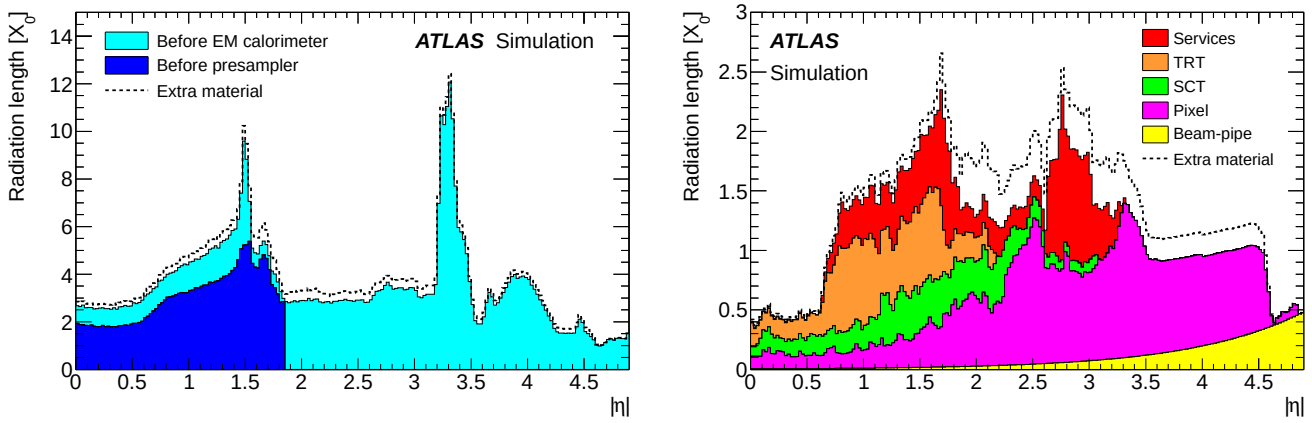

Fig. 1. Amount of material, in units of radiation length X_0, traversed by a particle as a function of η: (left) material in front of the presampler detector and the EM calorimeter, and (right) material up to the ID boundaries. The contributions of the different detector elements, including the services and thermal enclosures are shown separately by filled color areas. The extra material used for systematic studies is indicated by dashed lines. The primary vertex position has been smeared along the beamline.

cryostat that acts also as a support structure. It runs almost projective at the low radius part of EMEC IW.

4 Electron trigger, reconstruction and identification

4.1 Trigger

The ATLAS trigger system [12] is divided into three levels. The hardware-based first-level trigger (L1) performs a fast event selection by searching for high-p_{T} objects and large missing or total energy using reduced granularity data from the calorimeters and the muon system and reduces the event rate to a maximum of 75 kHz. It is followed by the software-based second-level trigger (L2) and event filter (EF), collectively referred to as the high-level trigger (HLT). The reconstruction at L2 is seeded by the L1 result. It uses, with full granularity and precision, all the available detector data (including the information from the inner detector) but only in the regions identified by the L1 as Regions of Interest (RoI). After L2 selection, the event rate is about 3 kHz. In the EF, more complex algorithms seeded by the L2 results and profiting from offline-like calibration and alignment are used to reduce the event rate to about 200 Hz.

At L1, electromagnetic objects are selected if the total transverse energy deposited in the EM calorimeter in two adjacent towers of $\Delta\eta \times \Delta\phi = 0.1 \times 0.1$ size is above a certain threshold. Fast calorimeter and tracking reconstruction algorithms are deployed at L2. The L2 calorimeter reconstruction is very similar to the offline algorithm, with the notable difference that clusters are seeded by the highest E_{T} cell in the middle calorimeter layer instead of applying the full offline sliding-window algorithm described in Subsection 4.2. The L2 track reconstruction algorithm was developed independently to fulfill the more stringent timing requirements. The EF uses the offline reconstruction and identification algorithms described in Subsections 4.2 and 4.4. It applies similar (typically somewhat looser) cuts in order to remain fully efficient for objects identified offline.

During the 2010 proton-proton collision data taking period, the trigger menu continuously evolved in order to fully benefit from the increasing LHC luminosity. Initially, the trigger relied on the L1 decision only while the HLT decisions were recorded but not used to reject events. As the luminosity increased, the HLT began actively rejecting events with higher and higher E_{T} thresholds and more stringent selections. A detailed description of the trigger configuration and selection criteria applied in 2010 can be found in Refs. [12,13].

4.2 Reconstruction

Electron reconstruction [14] in the *central region* of $|\eta| < 2.47$ starts from energy deposits (clusters) in the EM calorimeter which are then associated to reconstructed tracks of charged particles in the inner detector.

To reconstruct the EM clusters, seed clusters of longitudinal towers with total transverse energy above 2.5 GeV are searched for by a *sliding-window* algorithm. The window size is 3×5 in units of 0.025×0.025 in $\eta \times \phi$ space, corresponding to the granularity of the calorimeter middle layer. The cluster reconstruction is expected to be very efficient for true electrons. In MC simulations, the efficiency is about 95% at $E_{\mathrm{T}} = 5$ GeV and 100% for electrons with $E_{\mathrm{T}} > 15$ GeV from W and Z decays.

In the tracking volume of $|\eta| < 2.5$, reconstructed tracks extrapolated from their last measurement point to the middle layer of the calorimeter are very loosely matched to the seed clusters. The distance between the track impact point and the cluster position is required to

satisfy $\Delta\eta < 0.05$. To account for bremsstrahlung losses, the size of the sign corrected $\Delta\phi$ window is 0.1 on the side where the extrapolated track bends as it traverses the solenoidal magnetic field and is 0.05 on the other side. An electron is reconstructed if at least one track is matched to the seed cluster. In the case where several tracks are matched to the same cluster, tracks with silicon hits are preferred, and the one with the smallest $\Delta R = \sqrt{\Delta\eta^2 + \Delta\phi^2}$ distance to the seed cluster is chosen.

The electron cluster is then rebuilt using 3×7 (5×5) longitudinal towers of cells in the barrel (endcaps). These lateral cluster sizes were optimized to take into account the different overall energy distributions in the barrel and endcap calorimeters. The cluster energy is then determined [2] by summing four different contributions: (1) the estimated energy deposit in the material in front of the EM calorimeter, (2) the measured energy deposit in the cluster, (3) the estimated external energy deposit outside the cluster (lateral leakage), and (4) the estimated energy deposit beyond the EM calorimeter (longitudinal leakage). The four terms are parametrised as a function of the measured cluster energies in the presampler detector (where it is present) and in the three EM calorimeter longitudinal layers based on detailed simulation of energy deposition in both active and inactive material in the relevant detector systems. The good description of the detector in the MC simulation is therefore essential in order to correctly reconstruct the electron energy.

The four-momentum of *central electrons* is computed using information from both the final cluster and the best track matched to the original seed cluster. The energy is given by the cluster energy. The ϕ and η directions are taken from the corresponding track parameters at the vertex.

In the *forward region*, $2.5 < |\eta| < 4.9$, where there are no tracking detectors, the electron candidates are reconstructed only from energy deposits in the calorimeters by grouping neighbouring cells in three dimensions, based on the significance of their energy content with respect to the expected noise. These *topological clusters* [15] have a variable number of cells in contrast to the fixed-size sliding-window clusters used in the central region. The direction of *forward electrons* is defined by the barycentre of the cells belonging to the cluster. The energy of the electron is determined simply by summing the energies in the cluster cells and is then corrected for energy loss in the passive material before the calorimeter. An electron candidate in the forward region is reconstructed only if it has a small hadronic energy component and a transverse energy of $E_{\mathrm{T}} > 5$ GeV.

4.3 Requirements on calorimeter operating conditions

The quality of the reconstructed energy of an electron object relies on the conditions of the EM calorimeter. Three types of problems arose during data taking that needed to be accounted for at the analysis level:

- Failures of electronic front-end boards (FEBs). A few percent of the cells are not read out because they are connected to non-functioning FEBs, on which the active part (VCSEL) of the optical transmitter to the readout boards has failed [16]. As this can have an important impact on the energy reconstruction in the EM calorimeter, the electron is rejected if part of the cluster falls into a dead FEB region in the EM calorimeter strip or middle layer. If the dead region is in the back layer or in the presampler detector, which in general contain only a small fraction of the energy of the shower, the object is considered good and an energy correction is provided at the reconstruction level.
- High voltage (HV) problems. A few percent of the HV sectors are operated under non-nominal high voltage, or have a zero voltage on one side of the readout electrode (for redundancy, each side of an EM electrode, which is in the middle of the LAr gap, is powered separately) [16]. In the very rare case when a part of the cluster falls into a dead high-voltage region, the cluster is rejected. Non-nominal voltage conditions increase the equivalent noise in energy but do not require special treatment for the energy reconstruction.
- Isolated cells producing a high noise signal or no signal at all. These cells are masked at the reconstruction level, so that their energy is set to the average of the neighbouring cells. Nonetheless an electron is rejected, if any of the cells in its core, defined as the 3x3 cells in the middle layer, is masked.

The loss of acceptance due to these object quality requirements was about 6% per electron on average dominated by losses due to non-functioning FEBs (replaced during the 2010/2011 LHC winter shutdown).

These requirements are also applied to the MC samples when performing comparisons with data. Nonetheless, differences arise between data and MC, induced for example by the treatment of clusters around dead FEBs. While the barycentre of such clusters tends to be shifted in the data, this behaviour is not fully reproduced by MC when the dead area has not been simulated. The total uncertainty on the loss of acceptance is estimated to be about 0.4% per electron.

4.4 Identification

The baseline electron identification in the central $|\eta| < 2.47$ region relies on a cut-based selection using calorimeter, tracking and combined variables that provide good separation between isolated or non-isolated signal electrons, background electrons (primarily from photon conversions and Dalitz decays) and jets faking electrons. The cuts can be applied independently. Three reference sets of cuts have been defined with increasing background rejection power: *loose*, *medium* and *tight* [14] with an expected jet rejection of about 500, 5000 and 50000, respectively, based on MC simulation. Shower shape variables of the EM calorimeter middle layer and hadronic leakage variables are used in the *loose* selection. Variables from the

Table 1. Definition of variables used for *loose*, *medium* and *tight* electron identification cuts for the central region of the detector with $|\eta| < 2.47$.

Type	Description	Name
Loose selection		
Acceptance	$\|\eta\| < 2.47$	
Hadronic leakage	Ratio of E_T in the first layer of the hadronic calorimeter to E_T of the EM cluster (used over the range $\|\eta\| < 0.8$ and $\|\eta\| > 1.37$)	$R_{\rm had1}$
	Ratio of E_T in the hadronic calorimeter to E_T of the EM cluster (used over the range $\|\eta\| > 0.8$ and $\|\eta\| < 1.37$)	$R_{\rm had}$
Middle layer of EM calorimeter	Ratio of the energy in 3×7 cells over the energy in 7×7 cells centred at the electron cluster position	R_η
	Lateral shower width, $\sqrt{(\Sigma E_i \eta_i^2)/(\Sigma E_i) - ((\Sigma E_i \eta_i)/(\Sigma E_i))^2}$, where E_i is the energy and η_i is the pseudorapidity of cell i and the sum is calculated within a window of 3×5 cells	$w_{\eta 2}$
Medium selection (includes loose)		
Strip layer of EM calorimeter	Shower width, $\sqrt{(\Sigma E_i (i - i_{\rm max})^2)(\Sigma E_i)}$, where i runs over all strips in a window of $\Delta\eta \times \Delta\phi \approx 0.0625 \times 0.2$, corresponding typically to 20 strips in η, and $i_{\rm max}$ is the index of the highest-energy strip	$w_{\rm stot}$
	Ratio of the energy difference between the largest and second largest energy deposits in the cluster over the sum of these energies	$E_{\rm ratio}$
Track quality	Number of hits in the pixel detector (≥ 1)	$n_{\rm pixel}$
	Number of total hits in the pixel and SCT detectors (≥ 7)	$n_{\rm Si}$
	Transverse impact parameter ($\|d_0\|$ <5 mm)	d_0
Track–cluster matching	$\Delta\eta$ between the cluster position in the strip layer and the extrapolated track ($\|\Delta\eta\| < 0.01$)	$\Delta\eta$
Tight selection (includes medium)		
Track–cluster matching	$\Delta\phi$ between the cluster position in the middle layer and the extrapolated track ($\|\Delta\phi\| < 0.02$)	$\Delta\phi$
	Ratio of the cluster energy to the track momentum	E/p
	Tighter $\Delta\eta$ requirement ($\|\Delta\eta\| < 0.005$)	$\Delta\eta$
Track quality	Tighter transverse impact parameter requirement ($\|d_0\|$ <1 mm)	d_0
TRT	Total number of hits in the TRT	$n_{\rm TRT}$
	Ratio of the number of high-threshold hits to the total number of hits in the TRT	$f_{\rm HT}$
Conversions	Number of hits in the b-layer (≥ 1)	$n_{\rm BL}$
	Veto electron candidates matched to reconstructed photon conversions	

EM calorimeter strip layer, track quality requirements and track-cluster matching are added to the *medium* selection. The *tight* selection adds E/p, particle identification using the TRT, and discrimination against photon conversions via a b-layer hit requirement and information about reconstructed conversion vertices [17]. Table 1 lists all variables used in the *loose*, *medium* and *tight* selections. The cuts are optimised in 10 bins of cluster η (defined by calorimeter geometry, detector acceptances and regions of increasing material in the inner detector) and 11 bins of cluster E_T from 5 GeV to above 80 GeV.

Electron identification in the forward $2.5 < |\eta| < 4.9$ region, where no tracking detectors are installed, is based solely on cluster moments[1] and shower shapes [14]. These provide efficient discrimination against hadrons due to the good transverse and longitudinal segmentation of the calorimeters, though it is not possible to distinguish between electrons and photons. Two reference sets of cuts are defined, *forward loose* and *forward tight* selections. Table 2 lists the identification variables.

[1] The cluster moment of degree n for a variable x is defined as:

$$\langle x^n \rangle = \frac{\sum_i E_i \, x_i^n}{\sum_i E_i}, \qquad (1)$$

where i runs over all cells of the cluster.

4.5 Inclusive single and dielectron spectra

To illustrate the electron identification performance, the left of Figure 2 shows the $E_{\rm T}$ distribution of all electron candidates passing the *tight* identification cuts and having $|\eta| < 2.47$ excluding the transition region, $1.37 < |\eta| < 1.52$. The data sample was collected by single electron triggers with varying thresholds. The Jacobian peak at $E_{\rm T} \approx 40$ GeV from W and Z decays is clearly visible above the sum of contributions from semi-leptonic decays of beauty and charm hadrons, electrons from photon conversions and hadrons faking electrons.

Table 2. Definition of variables used for *forward loose* and *forward tight* electron identification cuts for the $2.5 < |\eta| < 4.9$ region of the detector.

Type	Description	Name
Forward loose selection		
Acceptance	$2.5 < \|\eta\| < 4.9$	
Shower depth	Distance of the shower barycentre from the calorimeter front face measured along the shower axis	λ_{centre}
Longitudinal second moment	Second moment of the distance of each cell to the shower centre in the longitudinal direction (λ_i)	$\langle\lambda^2\rangle$
Transverse second moment	Second moment of the distance of each cell to the shower centre in the transverse direction (r_i)	$\langle r^2\rangle$
Forward tight selection (includes forward loose)		
Maximum cell energy	Fraction of cluster energy in the most energetic cell	$f_{\max}$
Normalized lateral moment	w_2 is the second moment of r_i setting $r_i = 0$ for the two most energetic cells, while $w_{\max}$ is the second moment of r_i setting $r_i = 4$ cm for the two most energetic cells and $r_i = 0$ for the others	$\frac{w_2}{w_2+w_{\max}}$
Normalized longitudinal moment	l_2 is the second moment of λ_i setting $\lambda_i = 0$ for the two most energetic cells, while $l_{\max}$ is the second moment of λ_i setting $\lambda_i = 10$ cm for the two most energetic cells and $\lambda_i = 0$ for the others	$\frac{l_2}{l_2+l_{\max}}$

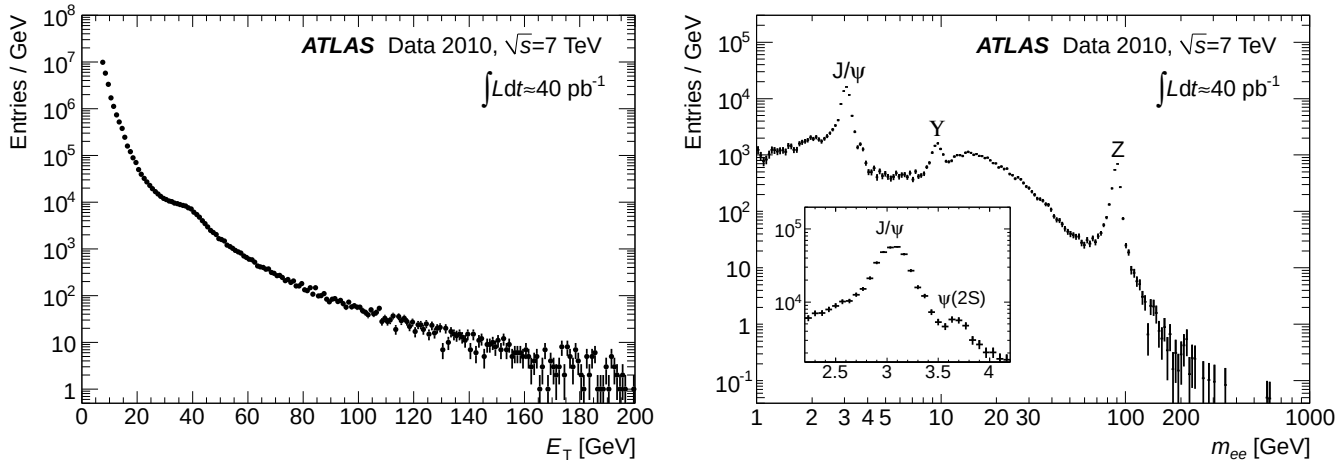

Fig. 2. (left) E_{T} distribution of electron candidates passing the *tight* identification cuts for events selected by single electron triggers with varying E_{T} thresholds. Data with $E_{\text{T}} < 20$ GeV correspond to lower integrated luminosity values and were rescaled to the full luminosity. (right) Reconstructed dielectron mass distribution of electron candidate pairs passing the *tight* identification cuts for events selected by low E_{T} threshold dielectron triggers. The number of events is normalised by the bin width. Errors are statistical only.

The measurement of known particles decaying into dielectron final states is an important ingredient in order to calibrate and measure the performance of the detector. The dielectron mass spectrum is plotted on the right of Figure 2 using a selection of unprescaled, low E_{T} threshold dielectron triggers. Both electrons are required to pass the *tight* selection, to be of opposite sign, and to have $E_{\text{T}} > 5$ GeV and $|\eta| < 2.47$. The J/ψ, Υ and Z peaks are clearly visible, and evidence for the ψ(2S) meson is also apparent. The shoulder in the region of $m_{ee} \approx 15$ GeV is caused by the kinematic selection.

4.6 Inter-alignment of the inner detector and the electromagnetic calorimeter

A global survey of the positions of the LAr cryostats and of the calorimeters inside them was performed with an accuracy of about $1-2$ mm during their integration and installation in the ATLAS cavern[2]. Since the intrinsic accuracy of the EM calorimeter shower position measurement is expected to be about 200 μm for high energy electrons[1],

[2] Measurements were performed when warm and predictions are used to estimate the calorimeter positions inside the cryostats when cold.

accurate measurements of the in-situ positions of the EM calorimeters are prerequisites to precise matching of the extrapolated tracks and the shower barycentres.

For most ATLAS analyses using track–cluster matching cuts (as described in Table 1), or photon pointing, a precision of the order of 1 mm is sufficient. A precision as good as 100 μm is very valuable to improve bremsstrahlung recovery for precision measurements, such as the W mass measurement.

The relative positions of the four independent parts of the EM calorimeter (two half-barrels and two endcaps) were measured with respect to the inner detector position, assuming that the ID itself is already well-aligned. About 300000 electron candidates with $p_{\mathrm{T}} > 10$ GeV, passing the *medium* identification cuts, were used.

The comparison of the cluster position and the extrapolated impact point of the electron track on the calorimeter provides a determination of the calorimeter translations and tilts with respect to their nominal positions. A correction for the sagging of the calorimeter absorbers (affecting the azimuthal measurement of the cluster) has been included for the barrel calorimeter with an amplitude of 1 mm. The derived alignment constants are then used to correct the electron cluster positions.

To illustrate the improvements brought by this first alignment procedure, the $\Delta\eta$ track–cluster matching variable used in electron reconstruction and identification is shown in Figure 3. Here, a sample of electron candidates collected at the end of the 2010 data taking period with $p_{\mathrm{T}} > 20$ GeV, passing the *medium* identification cuts and requirements similar to the ones described in Subsection 5.1.1 to select W and Z candidates, is used. The two-peak structure for $-2.47 < \eta < -1.52$ visible on the left is due to the transverse displacement of the endcap by about 5 mm which is then corrected by the alignment procedure. On the right of Figure 3, $\Delta\phi$ for the barrel $-1.37 < \eta < 0$ is also shown. After including corrections for sagging, a similar precision is reached in ϕ in the endcaps, as well. After the inter-alignment, the *tight* track–cluster matching cuts ($|\Delta\eta| < 0.005$ and $|\Delta\phi| < 0.02$) can be applied with high efficiency.

These inter-alignment corrections are applied for all datasets used in the following sections.

5 Electron energy scale and resolution

5.1 Electron energy-scale determination

The electromagnetic calorimeter energy scale was derived from test-beam measurements. The total uncertainty is 3% in the central region covering $|\eta| < 2.47$, and it is 5% in the forward region covering $2.5 < |\eta| < 4.9$. The dominant uncertainty, introduced by the transfer of the test-beam results to the ATLAS environment, comes from the LAr absolute temperature normalization in the test beam cryostat.

Even with the limited statistics of $Z \to ee$ and $J/\psi \to ee$ decays available in the 2010 dataset, the well known masses of the Z and J/ψ particles can be used to improve considerably the knowledge of the electron energy scale and to establish the linearity of the response of the EM calorimeter. An alternative strategy to determine the electron energy scale is to study the ratio of the energy E measured by the EM calorimeter and the momentum p measured by the inner detector, E/p. This technique gives access to the larger statistics of $W \to e\nu$ events but depends on the knowledge of the momentum scale and therefore the alignment of the inner detector.

The strategy to calibrate the EM calorimeter is described in Refs. [2,18]. It was validated using test-beam data [19,20,21]. The energy calibration is divided into three steps:

1. The raw signal extracted from each cell in ADC counts is converted into a deposited energy using the electronic calibration of the EM calorimeter [18,22,23].
2. MC-based calibration [2] corrections are applied at the cluster level for energy loss due to absorption in the passive material and leakage outside the cluster as discussed in Subsection 4.2. For the central region, $|\eta| < 2.47$, additional fine corrections depending on the η and ϕ coordinates of the electron are made to compensate for the energy modulation as a function of the impact point.
3. The in-situ calibration using $Z \to ee$ decays determines the energy scale and intercalibrates, as described in Subsection 5.1.1, the different regions of the calorimeters covering $|\eta| < 4.9$.

For calibrated electrons with transverse energy larger than 20 GeV, the ratio between the reconstructed and the true electron energy is expected to be within 1% of unity for almost all pseudorapidity regions. The energy resolution is better than 2% for $E_{\mathrm{T}} > 25$ GeV in the most central region, $|\eta| < 0.6$, and only exceeds 3% close to the transition region of the barrel and endcap calorimeters where the amount of passive material in front of the calorimeter is the largest.

This section describes the in-situ measurement of the electron energy scale and the determination of the energy resolution. The in-situ calibration is performed using $Z \to ee$ decays both for central and forward electrons. The linearity of response versus energy is cross-checked in the central region using $J/\psi \to ee$ and $W \to e\nu$ decays, but only with limited accuracy. Due to the modest $Z \to ee$ statistics in the 2010 data sample, the intercalibration is performed only among the calorimeter sectors in η. The non-uniformities versus ϕ are much smaller, as expected. They are shown in Subsection 5.1.5.

5.1.1 Event selection

High-E_{T} electrons from Z and W decays are collected using EM triggers requiring a transverse energy above about $15 - 17$ GeV in the early data taking periods and a high-level trigger also requiring *medium* electron identification criteria in later periods. Low-E_{T} electrons from J/ψ are

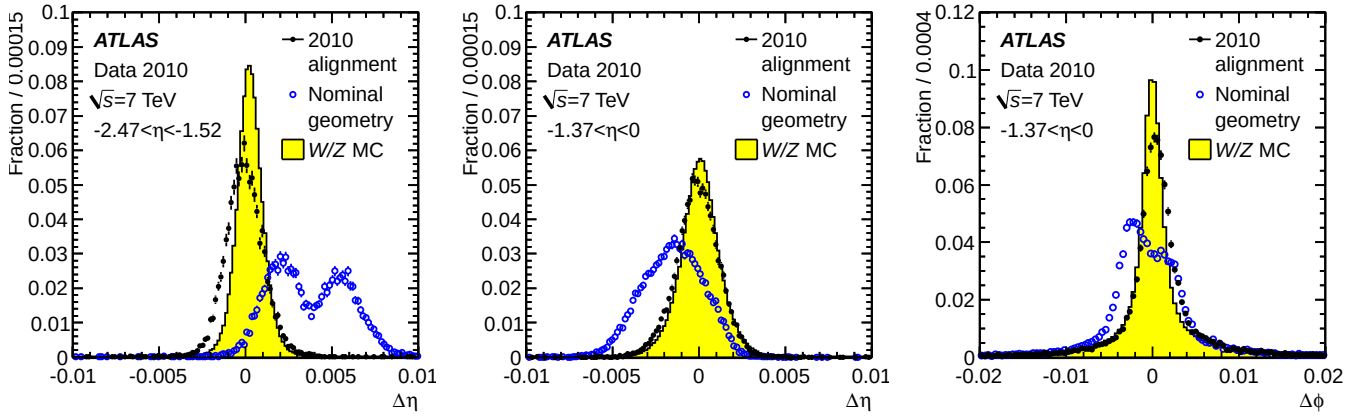

Fig. 3. Track–cluster matching variables of electron candidates from W and Z decays for reconstruction with nominal geometry and after the 2010 alignment corrections have been applied: (left) $\Delta\eta$ distributions for $-2.47 < \eta < -1.52$ and (middle) $-1.37 < \eta < 0$; (right) $\Delta\phi$ distributions for $-1.37 < \eta < 0$. The MC prediction with perfect alignment is also shown.

selected by a mixture of low E_{T} threshold EM triggers depending on the data taking period. All events must have at least one primary vertex formed by at least 3 tracks.

Electrons are required to be within $|\eta| < 2.47$ excluding the transition region of $1.37 < |\eta| < 1.52$ for central, and within $2.5 < |\eta| < 4.9$ for forward candidates. Electrons from W and Z (resp. J/ψ) decays must have $E_{\mathrm{T}} > 20$ GeV (resp. $E_{\mathrm{T}} > 5$ GeV).

For central–central Z selection, the *medium* identification cut is applied for both electrons, and for the central–forward Z selection, a central *tight* and a *forward loose* electron are required. To suppress the larger background *tight–tight* pairs are selected for the J/ψ analysis. For Z and J/ψ selections in the central region, only oppositely charged electrons are considered (no charge information is available in the forward region). The dielectron invariant mass should be in the range $80-100$ GeV for $Z \to ee$ and $2.5-3.5$ GeV for $J/\psi \to ee$ candidates.

For the W selection, a *tight* electron is required with additional cuts applied on jet cleaning [24], missing transverse momentum $E_{\mathrm{T}}^{\mathrm{miss}} > 25$ GeV and transverse mass[3] $m_{\mathrm{T}} > 40$ GeV. $Z \to ee$ events are suppressed by rejecting events containing a second *medium* electron.

In total, about 10000 central–central Z and 3100 central–forward Z candidates are selected in the reconstructed dielectron mass range $m_{ee} = 80-100$ GeV. The number of J/ψ candidates is about 8500 in the mass range $m_{ee} = 2.5-3.5$ GeV. The largest statistics, about 123000 candidates, comes from W decays.

The amount of background contamination is estimated from data to be about 1% for the central–central electron pairs and 14% for the central–forward electron pairs for the $Z \to ee$ selection. It is significantly higher, 23%, for the $J/\psi \to ee$ selection. It amounts to 7% for the $W \to e\nu$ selection.

[3] The transverse mass is defined as

$$m_{\mathrm{T}} = \sqrt{2E_{\mathrm{T}}^{e}E_{\mathrm{T}}^{\mathrm{miss}}(1-\cos(\phi^{e}-\phi^{\mathrm{miss}}))},$$

where E_{T}^{e} is the electron transverse energy, $E_{\mathrm{T}}^{\mathrm{miss}}$ is the missing transverse momentum, ϕ^{e} is the electron direction and ϕ^{miss} is the direction of $E_{\mathrm{T}}^{\mathrm{miss}}$ in ϕ.

5.1.2 Energy-scale determination using dielectron decays of Z and J/ψ particles

Any residual miscalibration for a given region i is parametrised by

$$E^{\mathrm{meas}} = E^{\mathrm{true}}(1+\alpha_i), \qquad (2)$$

where E^{true} is the true electron energy, E^{meas} is the energy measured by the calorimeter after MC-based energy-scale correction, and α_i measures the residual miscalibration. The α energy-scale correction factors are determined by a fit minimizing the negative unbinned log-likelihood [2]:

$$-\ln L_{\mathrm{tot}} = \sum_{i,j}\sum_{k=1}^{N_{ij}^{\mathrm{events}}} -\ln L_{ij}\left(\frac{m_k}{1+\frac{\alpha_i+\alpha_j}{2}}\right), \qquad (3)$$

where the indices i, j denote the regions considered for the calibration with one of the electrons from the $Z \to ee$ decay being in region i and the other in region j, N_{ij}^{events} is the total number of selected $Z \to ee$ decays with electrons in regions i and j, m_k is the measured dielectron mass in a given decay, and $L_{ij}(m)$ is the probability density function (pdf) quantifying the compatibility of an event with the Z lineshape. This pdf template is obtained from `PYTHIA` MC simulation and smoothed to get a continuous distribution. Since the experimental distribution of the dielectron invariant mass depends strongly on the cluster η of the two electrons, mainly due to the material in front of the calorimeter, the pdf is produced separately for different bins in $|\eta|$ of the two electron clusters.

The procedure described above was applied to the full 2010 dataset in 58 η bins over the full calorimeter coverage of $|\eta| < 4.9$ and is considered as the *baseline calibration* method. The resulting α values are shown on the left of

Figure 4. They are within ±2% in the barrel region and within ±5% in the forward regions. The rapid variations with η occur at the transitions between the different EM calorimeter systems as indicated in Figure 4. The variations within a given calorimeter system are due to several effects related to electronic calibration, high-voltage corrections (in particular in the endcaps[4]), additional material in front of the calorimeter, differences in the calorimeter and presampler energy scales, and differences in lateral leakage between data and MC.

The same procedure was applied using $J/\psi \to ee$ events to determine the electron energy scale. The resulting α values are in good agreement with the $Z \to ee$ measurement and the observed small differences are used in the following to estimate the uncertainty specific to low-E_{T} electrons.

5.1.3 Systematic uncertainties

The different sources of systematic uncertainties affecting the electron energy-scale measurement are summarized in Table 3 and discussed below:

- **Additional material** The imperfect knowledge of the material in front of the EM calorimeter affects the electron energy measurement since the deposited energy in any additional material is neither measured, nor accounted for in the MC-based energy calibration. Nonetheless, if additional material were present in data, the α correction factors extracted from $Z \to ee$ events would restore the electron energy scale on average. However, electrons from Z decays have an E_{T} spectrum with a mean value around 40 GeV. For other values of E_{T}, a residual uncertainty arises due to the extrapolation of the calibration corrections, as passive material affects lower-energy electrons more severely. This effect is estimated in two steps. First the calibration procedure is applied on a $Z \to ee$ MC sample produced, as explained in Section 3, with a dedicated geometry model with additional material in front of the calorimeters using the nominal MC sample to provide the reference Z lineshape, as performed on data. Then the non-linearity is measured using MC truth information by comparing the most probable value of the $E_{\mathrm{reco}}/E_{\mathrm{truth}}$ distributions between the nominal MC and the one with additional material in bins of electron E_{T}. The systematic uncertainty varies from -2% to $+1.2\%$. As expected and by construction, it vanishes for $E_{\mathrm{T}} \sim 40$ GeV corresponding to the average electron E_{T} in the $Z \to ee$ sample. This dominant uncertainty is therefore parametrised as a function of E_{T} for the different η regions.
- **Low-E_{T} electrons** The energy-scale calibration results obtained for $J/\psi \to ee$ and $Z \to ee$ decays can be compared. As shown on the right of Figure 4, the α correction factors extracted using $J/\psi \to ee$ decays after applying the baseline calibration using $Z \to ee$ decays are within 1% of unity, despite the very different E_{T} regimes of the two processes (the mean electron E_{T} in the J/ψ selection is about 9 GeV). This demonstrates the good linearity of the EM calorimeter and also that the amount of material before the calorimeter is modelled with reasonable accuracy. Nonetheless, a 1% additional uncertainty is added for electrons with $E_{\mathrm{T}} = 10$ GeV, decreasing linearly to 0% for $E_{\mathrm{T}} = 20$ GeV.
  Note, that the systematic uncertainties affecting the $J/\psi \to ee$ calibration are evaluated in the same manner as described here for the $Z \to ee$ analysis and are shown in Figure 4. The dominant uncertainty comes from the imperfect knowledge of the material in front of the calorimeter and varies between 0.2% in the central barrel and 1% close to the transition region between the barrel and endcap calorimeters.
- **Presampler detector energy scale** The sensitivity of the calibration to the measured presampler energy is significant because it is used to correct for energy lost upstream of the active EM calorimeter. Since the in-situ calibration only fixes one overall scale, it cannot correct for any difference between the presampler detector and the EM calorimeter energy scales. By comparing the energy deposited in the presampler by electrons from $W \to e\nu$ decays between data and MC simulation, one can extract an upper limit[5] on the presampler detector energy-scale uncertainty: it is about 5% in the barrel and 10% in the endcap regions up to $|\eta| = 1.8$. The impact on the electron energy scale due to the uncertainty on the presampler energy scale depends on η via the distribution of material in front of the calorimeter and on E_{T}, since the fraction of energy deposited in the presampler decreases as the electron energy increases. For very high-E_{T} electrons, this uncertainty should decrease asymptotically to zero. As for the material uncertainty, the α coefficients extracted from $Z \to ee$ data correct the electron energy scale on average for any bias on the presampler energy scale (giving by construction no bias at $E_{\mathrm{T}} \sim 40$ GeV) but will not improve the response linearity in energy. The largest uncertainty is 1.4%, found for the region $1.52 < |\eta| < 1.8$ and for $E_{\mathrm{T}} = 1$ TeV (due to the large extrapolation from $E_{\mathrm{T}} = 40$ GeV to this energy).
- **Calorimeter electronic calibration and cross-talk** Cells belonging to different sampling layers in the EM calorimeters may have slightly different energy scales due to cross-talk and uncertainties arising from an imperfect electronic calibration. The uncertainties on the energy scale relative to the middle layer for cells in the strip and back layers of the calorimeter are es-

[4] The form of the accordion in the endcap varies as a function of the radius. This implies a variation in the size of the LAr gap. Even though the HV is varied as a function of the radius to compensate this, the compensation is not perfect and residual effects are present.

[5] As this limit is extracted from data–MC comparisons, it will include contributions from the uncertainty on the material and therefore lead to some double-counting of this material uncertainty.

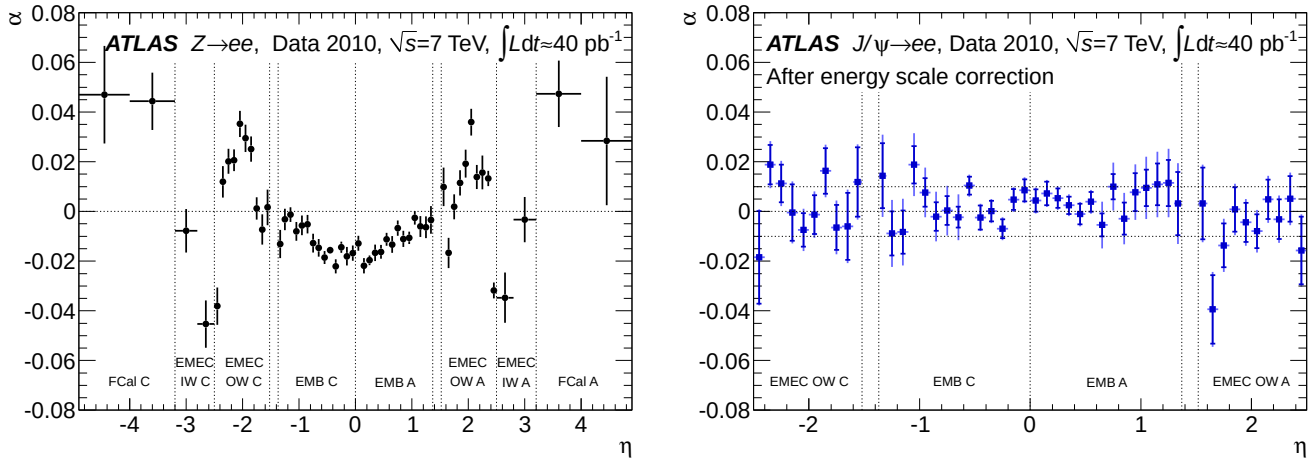

Fig. 4. The energy-scale correction factor α as a function of the pseudorapidity of the electron cluster derived from fits (left) to $Z \to ee$ data and (right) to $J/\psi \to ee$ data. The uncertainties of the $Z \to ee$ measurement are statistical only. The $J/\psi \to ee$ measurement was made after the $Z \to ee$ calibration had been applied. Its results are given with statistical (inner error bars) and total (outer error bars) uncertainties. The boundaries of the different detector parts defined in Section 2 are indicated by dotted lines.

timated to be 1% and 2%, respectively [25,26]. Using the same method as discussed above for the presampler detector energy scale, the uncertainty on the strip layer energy scale is found to be 0.1% for all η and E_{T}, while it is negligible on the back layer energy scale (as the energy deposited there is small).

– **Non-linearities in the readout electronics** The readout electronics provide a linear response to typically 0.1% [27]. This is taken as a systematic uncertainty on the extrapolation of the electron energy scale extracted from $Z \to ee$ events to higher energies.
– **Requirements on calorimeter operating conditions** To check the possible bias due to these requirements, a tighter veto was applied on electrons falling close to dead regions and electrons in regions with non-nominal high voltage were excluded. No significant effect is observed for the barrel and endcap calorimeters, while differences of $0.6 - 0.8\%$ are seen in the forward region.
– **Background and fit range** The effect of the background, predominantly from jets, on the extracted α values was studied by tightening the electron selection thereby decreasing the amount of background significantly. In addition, the fit range was also changed from $80 - 100$ GeV to $75 - 105$ GeV and $85 - 95$ GeV. The resulting uncertainty due to the electron selection is $+0.1\%$ in the barrel region and reaches $+1\%$ in the forward region, while due to the fit range it is 0.1% in the barrel region and grows to 0.6% in the forward region. These uncertainties are treated as uncorrelated.
– **Pile-up** The effect of pile-up is studied by determining the α coefficients as a function of the number of reconstructed primary vertices (from 1 to 4). The average $\langle\alpha\rangle$ increases very slightly with the number of primary vertices and a systematic uncertainty of 0.1% is assigned.
– **Possible bias of the method** The bias of the method is assessed by repeating the fit procedure on simulated data, resulting in a systematic uncertainty of 0.1% (0.2%) in the central (forward) region. Moreover, the results of alternative fit methods were compared on data and agree within $0.1 - 0.5\%$ ($0.8 - 1.0\%$). This is added as an additional uncertainty due to possible biases of the method.
– **Theoretical inputs** In the extraction of the α coefficients from the data, the MC simulation, which uses a certain model of the Z lineshape, serves as a reference. Uncertainties related to the imperfect physics modelling of QED final state radiation, of the parton density functions in the proton, and of the underlying event are found to be negligible.

To summarize, the overall systematic uncertainty on the electron energy scale is a function of E_{T} and η. It is illustrated in Figure 5 for two η-regions. For central electrons with $|\eta| < 2.47$, the uncertainty varies from 0.3% to 1.6%. The systematic uncertainties are smallest for $E_{\mathrm{T}} = 40$ GeV, typically below 0.4%. Below $E_{\mathrm{T}} = 20$ GeV, the uncertainty grows linearly with decreasing E_{T} and slightly exceeds 1% at $E_{\mathrm{T}} = 10$ GeV. For forward electrons with $2.5 < |\eta| < 4.9$, the uncertainties are larger and vary between 2% and 3%.

5.1.4 Energy-scale determination using E/p measurements

A complementary in-situ calibration method compares the energy E measured by the electromagnetic calorimeter to the momentum p measured by the inner detector. It allows to take advantage of the larger statistics of $W \to e\nu$ decays.

The ratio E/p is shown on the left of Figure 6 for electrons selected in the barrel EM calorimeter in $W \to e\nu$

Table 3. Systematic uncertainties (in %) on the electron energy scale in different detector regions.

	Barrel	Endcap	Forward
Additional material	E_{T}- and η-dependent, from -2% to $+1.2\%$		
Low-E_{T} region	E_{T}-dependent, from 1% at 10 GeV to 0% at 20 GeV		
Presampler energy scale	E_{T}- and η-dependent, $0-1.4\%$		
Strip layer energy scale	0.1	0.1	0.1
Electronic non-linearity	0.1	0.1	0.1
Object quality requirements	<0.1	<0.1	0.6−0.8
Background and fit range	0.1	0.3	1.2
Pile-up	0.1	0.1	0.1
Bias of method	0.1	0.1−0.5	0.8−1.0

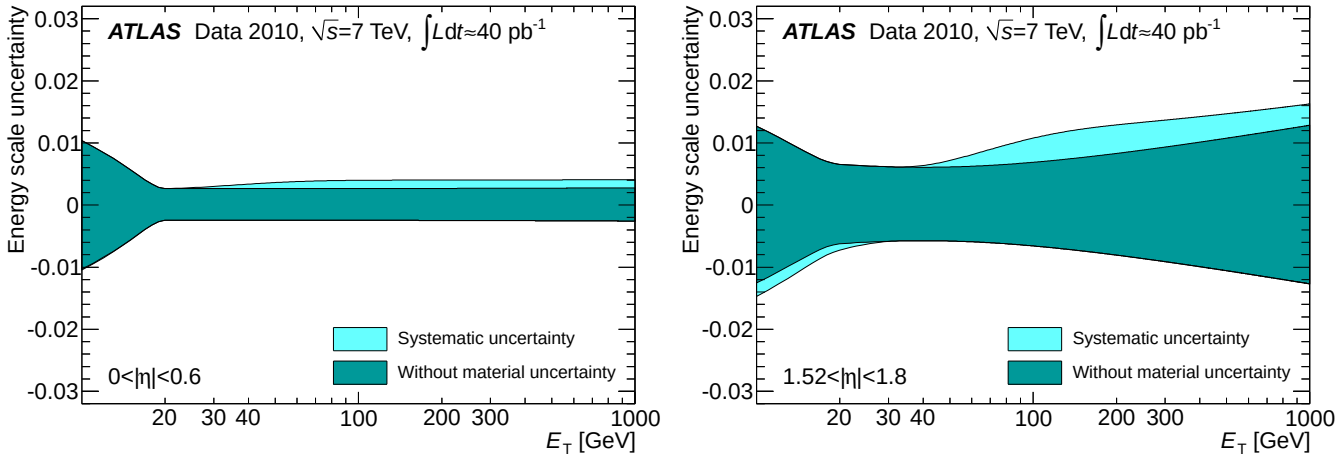

Fig. 5. Total systematic uncertainty on the electron energy scale (left) for the region $|\eta| < 0.6$ which has the smallest uncertainty. and (right) for $1.52 < |\eta| < 1.8$ which has the largest uncertainty within the central region. The uncertainty is also shown without the contribution due to the amount of additional material in front of the EM calorimeters.

events. E/p is close to unity, with a significant tail at large values due to Bremsstrahlung occurring in the inner detector. The core of the distribution can be described by a Gaussian whose width corresponds to the measurement error due to both the EM cluster energy and the track curvature resolutions.

The unbinned E/p distributions are fitted by a Crystal Ball function [28,29] and the most probable value, $\widehat{E/p}$, is extracted. The fit range, $0.9 < E/p < 2.2$, was chosen to be fully contained within the E_{T}- and η-dependent lower (0.7−0.8) and upper $(2.5-5.0)$ cuts applied in the *tight* electron selection. The correction factors $\alpha_{E/p}$ are then derived by

$$\widehat{E/p}_{\mathrm{data}} = \widehat{E/p}_{\mathrm{MC}}(1+\alpha_{E/p}). \quad (4)$$

On the right of Figure 6 the η dependence of the $\alpha_{E/p}$ coefficients measured using electrons and positrons from $W \to e\nu$ decays are shown after the baseline calibration had been applied. As expected, $\alpha_{E/p} \approx 0$ within about 1%. The fluctuations are larger in the endcaps, where the statistics are poorer.

The dominant systematic uncertainties on the measured $\alpha_{E/p}$ values arise from the fit procedure, (0.1-0.9)%, the description of the material in front of the EM calorimeter, (0.3-0.9)%, the background contamination in the selected electron sample, (0.2-1)%, and the track momentum measurement in the inner detector, (0.6-1.5)%. The total uncertainty increases with η and amounts to about 1% in the barrel and 2% in the endcaps.

The determination of the electron energy scale using the E/p distributions measured in $W \to e\nu$ decays agrees, within its larger systematic uncertainties, with the baseline method using the invariant mass distribution in $Z \to ee$ events, as shown on the right of Figure 6.

5.1.5 Energy response uniformity and linearity

The azimuthal uniformity of the calorimeter response is studied using both the dielectron invariant mass distributions of $Z \to ee$ events and the E/p distributions of $W \to e\nu$ events, after applying the η-dependent baseline calibration. The results are shown in Figure 7 for two η regions. They demonstrate a ϕ non-uniformity of less than about 1%.

The linearity of the calorimeter response is studied, after applying the η-dependent baseline calibration, by determining the α coefficients in bins of electron energy.

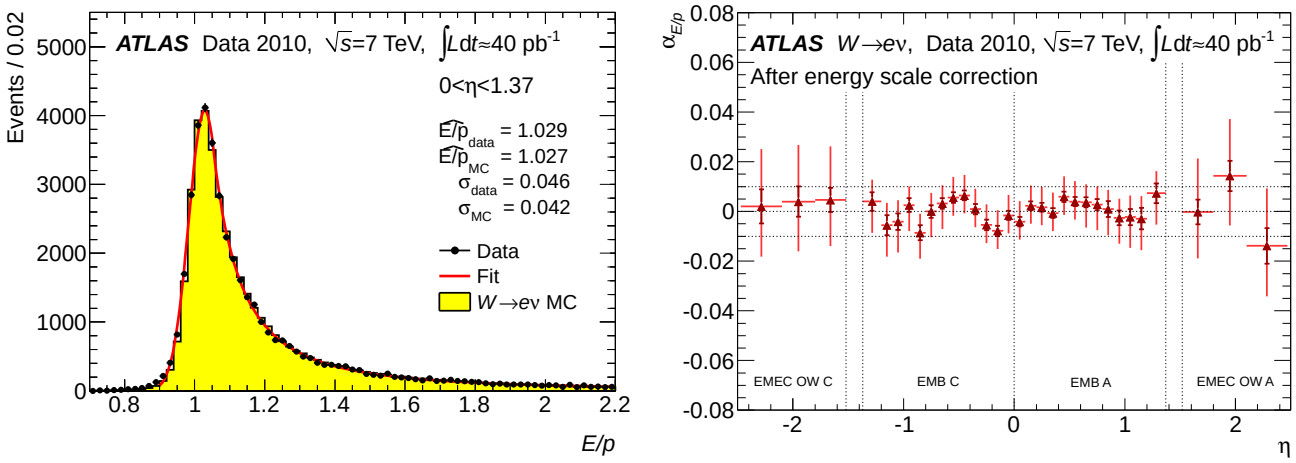

Fig. 6. (left) E/p distributions of electrons and positrons from $W \to e\nu$ decays for $0. < \eta < 1.37$ in data (full circles with statistical error bars) and $W \to e\nu$ MC (filled histogram). The result of the fit with a Crystal Ball function to the data is also shown (full line). The most probable value ($\widehat{E/p}$) and the Gaussian width (σ) of the fitted Crystal Ball function are given both for the data and the signal MC. (right) The $\alpha_{E/p}$ energy-scale correction factors derived from fits to E/p distributions of $W \to e\nu$ electron and positron data, after the baseline calibration had been applied. The inner error bars show the statistical uncertainty, while the outer error bars indicate the total uncertainty. The boundaries of the different detector parts defined in Section 2 are indicated by dotted lines.

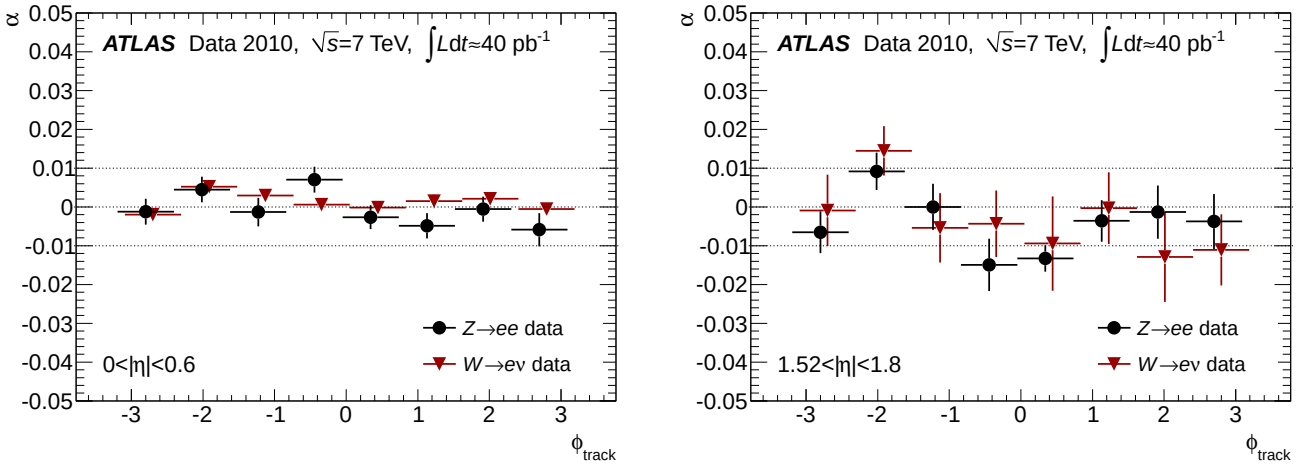

Fig. 7. The α energy-scale correction factor as a function of the electron track ϕ for (left) $|\eta| < 0.6$ and (right) $1.52 < |\eta| < 1.8$ determined by the baseline calibration using $Z \to ee$ decays (circles) and by the E/p method using $W \to e\nu$ decays (triangles). Errors are statistical only.

The $Z \to ee$ results are complemented at low energy by a $J/\psi \to ee$ calibration point as shown in Figure 8 for two regions: on the left the region $|\eta| < 0.8$ which has the smallest uncertainties, and on the right the region $1.52 < |\eta| < 1.8$ which is affected by the largest material uncertainties. Compared to E_{T} independent calibration, calibration factors obtained as a function of E_{T} are more sensitive to the description of the energy resolution. This effect was estimated by varying the energy resolution in MC simulation within its uncertainty and was found to be about 0.1% in the central region and up to 0.8% in the forward region. All measurements are found to be within the uncertainty bands assigned to the electron energy scale. For the central region, the results are cross-checked with the E/p method using $W \to e\nu$ events, averaged over the electron charge. Within the larger systematic uncertainties of the $W \to e\nu$ measurement, the linearity measurements agree well with the $Z \to ee$ data.

5.2 Electron energy resolution

The fractional energy resolution in the calorimeter is parametrised as

$$\frac{\sigma_E}{E} = \frac{a}{\sqrt{E}} \oplus \frac{b}{E} \oplus c. \qquad (5)$$

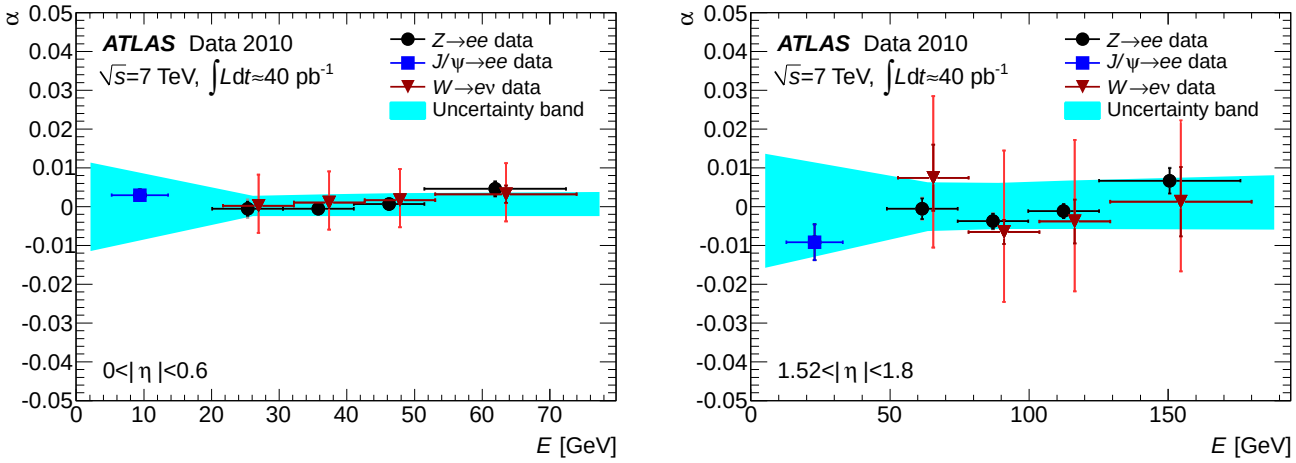

Fig. 8. The α energy-scale correction factor as a function of the electron energy for (left) $|\eta| < 0.6$ and (right) $1.52 < |\eta| < 1.8$ determined by the baseline calibration method using $Z \to ee$ (circles) and $J/\psi \to ee$ (square) decays and by the E/p method described in Subsection 5.1.4 using $W \to e\nu$ decays (triangles). For the $Z \to ee$ data points, the inner error bar represents the statistical uncertainty and the outer gives the combined error when bin migration effects are also included. The error on the $J/\psi \to ee$ measurements are statistical only. The band represents the systematic errors on the energy scale for the baseline calibration method as discussed in Table 3. For the E/p method, the inner error bar represents the statistical and the outer the total uncertainty.

Here a, b and c are η-dependent parameters: a is the sampling term, b is the noise term and c is the constant term.

Great care was taken during the construction of the calorimeter to minimise all sources of energy response non-uniformity, since any non-uniformity has a direct impact on the constant term of the energy resolution. The construction tolerances and the electronic calibration system ensure that the calorimeter response is locally uniform, with a local constant term below 0.5% [20] over regions of typical size $\Delta\eta \times \Delta\phi = 0.2 \times 0.4$. These regions are expected to be intercalibrated in situ to 0.5% achieving a global constant term[6] around 0.7% for the EM calorimeter, which is well within the requirement driven by physics needs, for example the $H \to \gamma\gamma$ sensitivity [18].

To extract the energy resolution function from data, more statistics are needed than available in the 2010 data sample. Therefore, only the constant term is determined here from a simultaneous analysis of the measured and predicted dielectron invariant mass resolution from $Z \to ee$ decays, taking the sampling and noise terms from MC simulation.

As shown in Figure 9, the measured dielectron mass distribution of electrons coming from $J/\psi \to ee$ decays is in good agreement with the MC prediction (both for the mean and the width). Since the electron energy resolution at these low energies is dominated by the contribution from the sampling term, it is assumed that the term a is well described, within a 10% uncertainty, as a function of η by the MC simulation. The noise term has a significant contribution only at low energies. Moreover, its effect on the measurement of the constant term cancels out to first order, since the noise description in the MC simulation is derived from calibration data runs. The above assumptions lead to the formula:

$$c_{\mathrm{data}} = \sqrt{2 \cdot \left(\left(\frac{\sigma}{m_Z} \right)^2_{\mathrm{data}} - \left(\frac{\sigma}{m_Z} \right)^2_{\mathrm{MC}} \right) + c^2_{\mathrm{MC}}} \ , \quad (6)$$

where c_{MC} is the constant term of about 0.5% in the MC simulation. The parameter c_{data} is an effective constant term which includes both the calorimeter constant term and the effect of inhomogeneities due to possible additional material. m_Z denotes the Z mass [30], and σ is the Gaussian component of the experimental resolution.

The resolutions are derived from fits to the invariant mass distributions using a Breit-Wigner convolved with a Crystal Ball function in the mass range $80 - 100$ GeV for central-central events and in the mass range $75 - 105$ GeV for central-forward events. The Breit-Wigner width is fixed to the measured Z width [30], and the experimental resolution is described by the Crystal Ball function. Figure 10 shows the invariant mass distributions of the selected $Z \to ee$ decays: the measured Gaussian components of the experimental resolution are always slightly worse than those predicted by MC, with the smallest deviation observed for barrel–barrel events (top left) and the largest one for central–EMEC-IW events (bottom left).

In central–forward events the two electrons belong to different detector regions. Therefore, when extracting the constant term in the forward region, a smearing is applied to the central electrons using the results of the barrel–barrel and endcap–endcap measurements.

[6] The long-range constant term is the residual miscalibration between the different calorimeter regions, and the global constant term is the quadratic sum of the local and long-range constant terms.

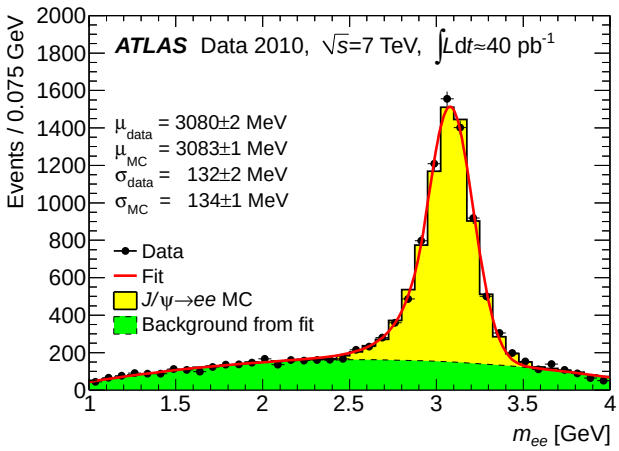

Fig. 9. Reconstructed dielectron mass distribution for $J/\psi \to ee$ decays, as measured after applying the baseline $Z \to ee$ calibration. The data (full circles with statistical error bars) are compared to the sum of the MC signal (light filled histogram) and the background contribution (darker filled histogram) modelled by a Chebyshev polynomial. The mean (μ) and the Gaussian width (σ) of the fitted Crystal Ball function are given both for data and MC.

Table 4. Measured effective constant term $c_{\rm data}$ (see Eq. 6) from the observed width of the $Z \to ee$ peak for different calorimeter η regions.

Sub-system	η-range	Effective constant term, $c_{\rm data}$
EMB	$\lvert\eta\rvert < 1.37$	$1.2\% \pm 0.1\%$ (stat) $^{+\ 0.5\%}_{-\ 0.6\%}$ (syst)
EMEC-OW	$1.52 < \lvert\eta\rvert < 2.47$	$1.8\% \pm 0.4\%$ (stat) $\pm 0.4\%$ (syst)
EMEC-IW	$2.5 < \lvert\eta\rvert < 3.2$	$3.3\% \pm 0.2\%$ (stat) $\pm 1.1\%$ (syst)
FCal	$3.2 < \lvert\eta\rvert < 4.9$	$2.5\% \pm 0.4\%$ (stat) $^{+\ 1.0\%}_{-\ 1.5\%}$ (syst)

The results obtained for the effective constant term are shown in Table 4. Several sources of systematic uncertainties are investigated. The dominant uncertainty is due to the uncertainty on the sampling term, as the constant term was extracted assuming that the sampling term is correctly reproduced by the simulation. To assign a systematic uncertainty due to this assumption, the simulation was modified by increasing the sampling term by 10%. The difference in the measured constant term is found to be about 0.4% for the EM calorimeter and 1% for the forward calorimeter. The uncertainty due to the fit procedure was estimated by varying the fit range. The uncertainty due to pile-up was investigated by comparing simulated MC samples with and without pile-up and was found to be negligible.

6 Efficiency measurements

In this section, the measurements of electron selection efficiencies are presented using the tag-and-probe method [31, 32]. $Z \to ee$ events provide a clean environment to study all components of the electron selection efficiency discussed in this paper. In certain cases, such as identification or trigger efficiency measurements, the statistical power of the results is improved using $W \to e\nu$ decays, as well. To extend the reach towards lower transverse energies, $J/\psi \to ee$ decays are also used to measure the electron identification efficiency. However the available statistics of $J/\psi \to ee$ events after the trigger requirements in the 2010 data sample are limited and do not allow a precise separation of the isolated signal component from b-hadron decays and from background processes.

6.1 Methodology

A measured electron spectrum needs to be corrected for efficiencies related to the electron selection in order to derive cross-sections of observed physics processes or limits on new physics. This correction factor is defined as the product of different efficiency terms. For the case of a single electron in the final state one can write:

$$C = \epsilon_{event} \cdot \alpha_{reco} \cdot \epsilon_{ID} \cdot \epsilon_{trig} \cdot \epsilon_{isol}. \qquad (7)$$

Here ϵ_{event} denotes the efficiency of the event preselection cuts, such as primary vertex requirements and event cleaning. α_{reco} accounts for the basic reconstruction efficiency to find an electromagnetic cluster and to match it loosely to a reconstructed charged particle track in the fiducial region of the detector and also for any kinematic and geometrical cuts on the reconstructed object itself. ϵ_{ID} denotes the efficiency of the identification cuts relative to reconstructed electron objects. ϵ_{trig} stands for the

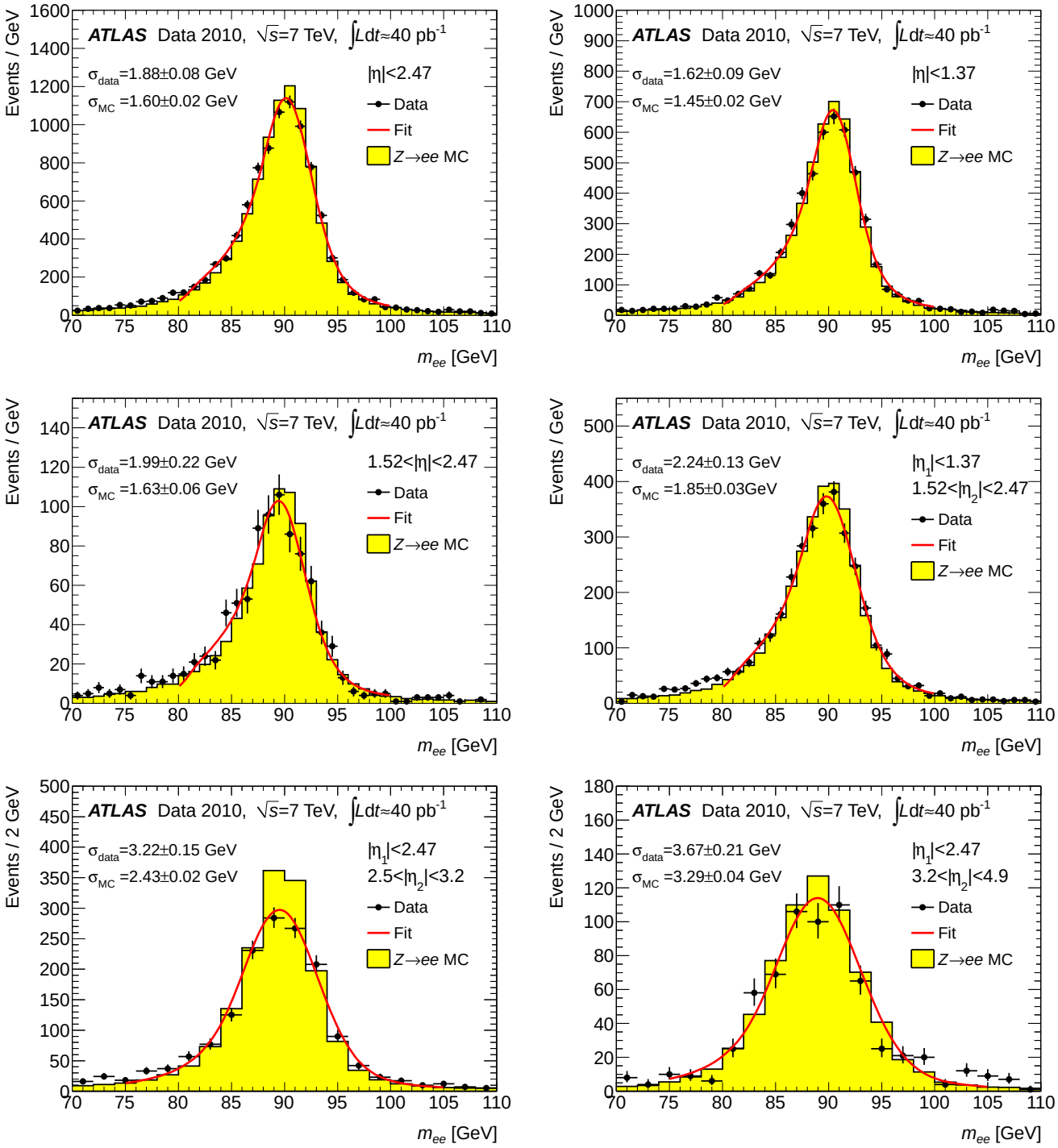

Fig. 10. Reconstructed dielectron mass distributions for $Z \to ee$ decays for different pseudorapidity regions after applying the baseline $Z \to ee$ calibration. The transition region $1.37 < |\eta| < 1.52$ is excluded. The data (full circles with statistical error bars) are compared to the signal MC expectation (filled histogram). The fits of a Breit-Wigner convolved with a Crystal Ball function are shown (full lines). The Gaussian width (σ) of the Crystal Ball function is given both for data and MC simulation.

the trigger efficiency with respect to all reconstructed and identified electron candidates. ϵ_{isol} is the efficiency of any isolation requirement, if applied, limiting the presence of other particles (tracks, energy deposits) close to the identified electron candidate.

In this paper, three of the above terms are studied: the dominant term of α_{reco} that accounts for the efficiency to loosely match a reconstructed track fulfilling basic quality criteria to a reconstructed cluster, the identification efficiency ϵ_{ID}, and the trigger efficiency ϵ_{trig} for the most important single electron triggers used in physics analyses based on 2010 data.

Note that the above decomposition is particularly useful as it allows the use of data-driven measurements of the above independent efficiency terms, such as the ones presented in this paper using the tag-and-probe (T&P) technique, in physics analyses, and therefore limits the reliance on MC simulation. This is usually done by correcting the MC predicted values of the above efficiency terms for a given physics process in bins (of typically E_{T} and η) by the measured ratios of the data to MC efficiencies in the T&P sample in the same bins. The range of validity of this method depends on the kinematic parameters of the electrons used in the physics analysis itself and on more implicit observables such as the amount of jet activity in the events considered in the analysis with respect to that observed in the T&P sample.

The T&P method aims to select a clean and unbiased sample of electrons, called *probe* electrons, using selection cuts, called *tag* requirements, primarily on other objects in the event. The efficiency of any selection cut can then be measured by applying it to the sample of probe electrons. In the following, a well-identified electron is used as the tag in the $Z \to ee$ and $J/\psi \to ee$ measurements and high missing transverse momentum is used in the $W \to e\nu$ measurements.

For most efficiency measurements presented here, the contamination of the probe sample by background (for example hadrons faking electrons, or electrons from heavy flavour decays, or electrons from photon conversions) requires the use of some background estimation technique (usually a side-band or a template fit method). The number of electron candidates is then independently estimated both at the probe level and at the level where the probe passes the cut of interest. The efficiency is then equivalent to the fraction of probe candidates passing the cut of interest.

Depending on the background subtraction method, different formulae for computing the statistical uncertainties on the efficiency measurements have been used as discussed in Ref. [33]. These formulae are approximate but generally conservative. When no background subtraction is necessary, the simple binomial formula is replaced by a Bayesian evaluation of the uncertainty.

The statistics available with the full 2010 dataset are not sufficient to measure any of the critical efficiency components as a function of two parameters, so the measurements are performed separately in bins of η and E_{T} of the probe. The bins in η are adapted to the detector geometry, while the E_{T}-binning corresponds to the optimization bins of the electron identification cuts.

6.2 Electron identification efficiency in the central region

The measurements of the efficiency of electron identification with the predefined sets of requirements, called *medium* and *tight* and described in Table 1, were performed on three complementary samples of $W \to e\nu$, $Z \to ee$ and $J/\psi \to ee$ events. While the electrons from $W \to e\nu$ and $Z \to ee$ decays are typically well-isolated, the $J/\psi \to ee$ signal is a mix of isolated and non-isolated electrons. Both prompt ($pp \to J/\psi X$) and non-prompt ($b \to J/\psi X'$) production contribute, and in the latter case the electrons from the $J/\psi \to ee$ decay are typically accompanied by other particles from the decay of the b-hadron. This, coupled with the higher background levels in the low-E_{T} region, makes the J/ψ analysis more demanding. The measurements cover the central region of the EM calorimeter within the tracking acceptance, $|\eta| < 2.47$, and the electron transverse energy range $E_{\mathrm{T}} = 4{-}50$ GeV. Electrons in the forward region, $2.5 < |\eta| < 4.9$, are discussed in Subsection 6.3.

6.2.1 Probe selection

The three data samples were obtained using a variety of triggers:

1. $W \to e\nu$ decays are collected using a set of $E_{\mathrm{T}}^{\mathrm{miss}}$ triggers. These triggers had an increasing $E_{\mathrm{T}}^{\mathrm{miss}}$ threshold from approximately 20 GeV initially at low luminosity to 40 GeV at the highest luminosities obtained in 2010. The total number of unbiased electron probes in this sample after background subtraction amounts to about 27500.
2. $Z \to ee$ decays are obtained using a set of single inclusive electron triggers with an E_{T} threshold of 15 GeV. The total number of unbiased electron probes in this sample is about 14500 after background subtraction.
3. $J/\psi \to ee$ decays are selected using a set of low-E_{T} single electron triggers with thresholds between 5 and 10 GeV. Towards the end of 2010, these triggers had to be heavily prescaled and a different trigger was used, requiring an electromagnetic cluster with $E_{\mathrm{T}} > 4$ GeV in addition to the single electron trigger. The total number of unbiased electron probes in this sample amounts to about 6000 after background subtraction. As already noted, they are a mix of isolated and non-isolated electrons from prompt and non-prompt J/ψ decays, respectively, with their fractions depending on the transverse energy bin.

Only events passing data-quality criteria, in particular concerning the inner detector and the calorimeters, are considered. At least one reconstructed primary vertex with at least three tracks should be present in the

event. Additional cuts were applied to minimise the impact of beam backgrounds and to remove electron candidates pointing to problematic regions of the calorimeter readout as discussed in Subsection 4.3.

Unbiased samples of electron probes, with minimal background under the signal, were obtained by applying stringent cuts to the trigger object in the event (a neutrino in the case of $W \to e\nu$ decays and one of the two electrons in the case of $Z \to ee$ and $J/\psi \to ee$ decays), which is thus the tag, and by selecting the electron probe following very loose requirements on the EM calorimeter cluster and the matching track:

- In the case of $W \to e\nu$ decays, simple kinematic requirements were made: $E_{\mathrm{T}}^{\mathrm{miss}} > 25$ GeV and $m_{\mathrm{T}} > 40$ GeV. For the fake electron background from multi-jet events, there is usually a strong correlation in the transverse plane between the azimuthal angle of the $E_{\mathrm{T}}^{\mathrm{miss}}$ vector and that of one of the highest E_{T} reconstructed jets. Thus a large rejection against fake electrons from hadrons or photon conversions can be obtained by requiring $E_{\mathrm{T}}^{\mathrm{miss}}$ isolation: the difference between the azimuthal angles of the missing transverse momentum and any jet having $E_{\mathrm{T}} > 10$ GeV was required to be $\Delta\phi > 2.5$ for the baseline analysis. This $\Delta\phi$ threshold was varied between 0.7 and 2.5 to assess the sensitivity of the measurements to the level of background under the $W \to e\nu$ signal.
- In the case of $Z \to ee$ (resp. $J/\psi \to ee$) decays, the tag electron was required to have $E_{\mathrm{T}} > 20$ (resp. 5) GeV, to match the corresponding trigger object, and to pass the *tight* electron identification requirements. The identification requirements were varied between the *medium* and *tight* selections to evaluate the sensitivity of the measurements to the level of background under the $Z \to ee$ and $J/\psi \to ee$ signal. The probe electron was required to be of opposite charge to the tag electron. In the $J/\psi \to ee$ selection, to address the case of high-E_{T} electrons that would often produce close-by EM showers in the calorimeter, the distance in ΔR between the two electron clusters was required to be larger than 0.1. All tag–probe pairs passing the cuts were considered.
- The probe electron was required to have $|\eta| < 2.47$, and $E_{\mathrm{T}} > 15$ GeV for $W \to e\nu$, $E_{\mathrm{T}} > 15$ GeV for $Z \to ee$, and $E_{\mathrm{T}} > 4$ GeV for $J/\psi \to ee$ decays.
- To reject beam-halo muons producing high-energy bremsstrahlung clusters in the EM calorimeter in the data sample collected by $E_{\mathrm{T}}^{\mathrm{miss}}$ triggers for the $W \to e\nu$ channel, certain track quality requirements have to be applied on the electron probes: the electron tracks should have at least one pixel hit and a total of at least seven silicon (pixel plus SCT) hits. These cuts have been applied in all three selections, $W \to e\nu$, $Z \to ee$ and $J/\psi \to ee$. Their efficiency is measured separately using $Z \to ee$ events as described in Subsection 6.4.

The same procedure is applied to the MC simulation, with in addition a reweighting of the MC to reproduce the pile-up observed in data as well as the proper mixture of the various triggers. Figure 11 shows the transverse energy distributions of the probes for each of the three channels and, for completeness since the $W \to e\nu$ channel relies on an orthogonal trigger based on $E_{\mathrm{T}}^{\mathrm{miss}}$, the transverse mass distribution for the $W \to e\nu$ selected probes. In order to compare these distributions to those expected from a signal MC, *tight* identification cuts have been applied to the probes resulting in very high purity in the case of the $W \to e\nu$ and $Z \to ee$ channels. In the case of the $J/\psi \to ee$ channel however, some background remains even at this stage, as can be seen from the excess of probes in data compared to MC at low E_{T}. The small differences seen between data and MC distributions in the $W \to e\nu$ measurement arise primarily from the imperfections of the modelling of the $E_{\mathrm{T}}^{\mathrm{miss}}$-triggers in simulation.

6.2.2 Background subtraction

The next step in the analysis is to use a discriminating variable to estimate the signal and background contributions in each E_{T} or η bin. This variable should ideally be uncorrelated to the electron identification variables.

Dielectron mass for the $Z \to ee$ and $J/\psi \to ee$ channels The reconstructed dielectron mass is the most efficient discriminating variable to estimate the signal and background contributions in the selected sample of electron probes from $Z \to ee$ and $J/\psi \to ee$ decays. The signal integration ranges, typically $80 < m_{ee} < 100$ GeV for the $Z \to ee$ channel and $2.8 < m_{ee} < 3.2$ GeV for the $J/\psi \to ee$ channel, were chosen to balance the possible bias of the efficiency measurement and the systematic uncertainty on the background subtraction.

In the $Z \to ee$ channel, which has more events and lower background contamination, the efficiency measurements in η-bins (for transverse energies $20 < E_{\mathrm{T}} < 50$ GeV) were performed with a simple same-sign background subtraction. For both channels, the shape of the background under the dielectron mass peak depends strongly on the E_{T}-bin due to kinematic threshold effects. Therefore for the measurements in E_{T}-bins (integrated over $|\eta| < 2.47$ and excluding the overlap region $1.37 < |\eta| < 1.52$), the background subtraction is performed as follows.

- In the $Z \to ee$ channel, a two-component fit with a signal contribution plus a background contribution is performed in each bin to the m_{ee} distribution over typical fit mass ranges of $40 < m_{ee} < 160$ GeV. The signal contribution is modelled either by a Breit-Wigner distribution convolved with a parametrisation of the low-mass tail, arising mostly from material effects, by a Crystal Ball function, or by a template obtained from $Z \to ee$ MC simulation. For the background contribution a variety of fit functions were considered. In the $Z \to ee$ measurement, an exponential and a single-sided exponential convolved with a Gaussian are used.
- In the case of the $J/\psi \to ee$ selection, where the background contamination is highest, the amount and

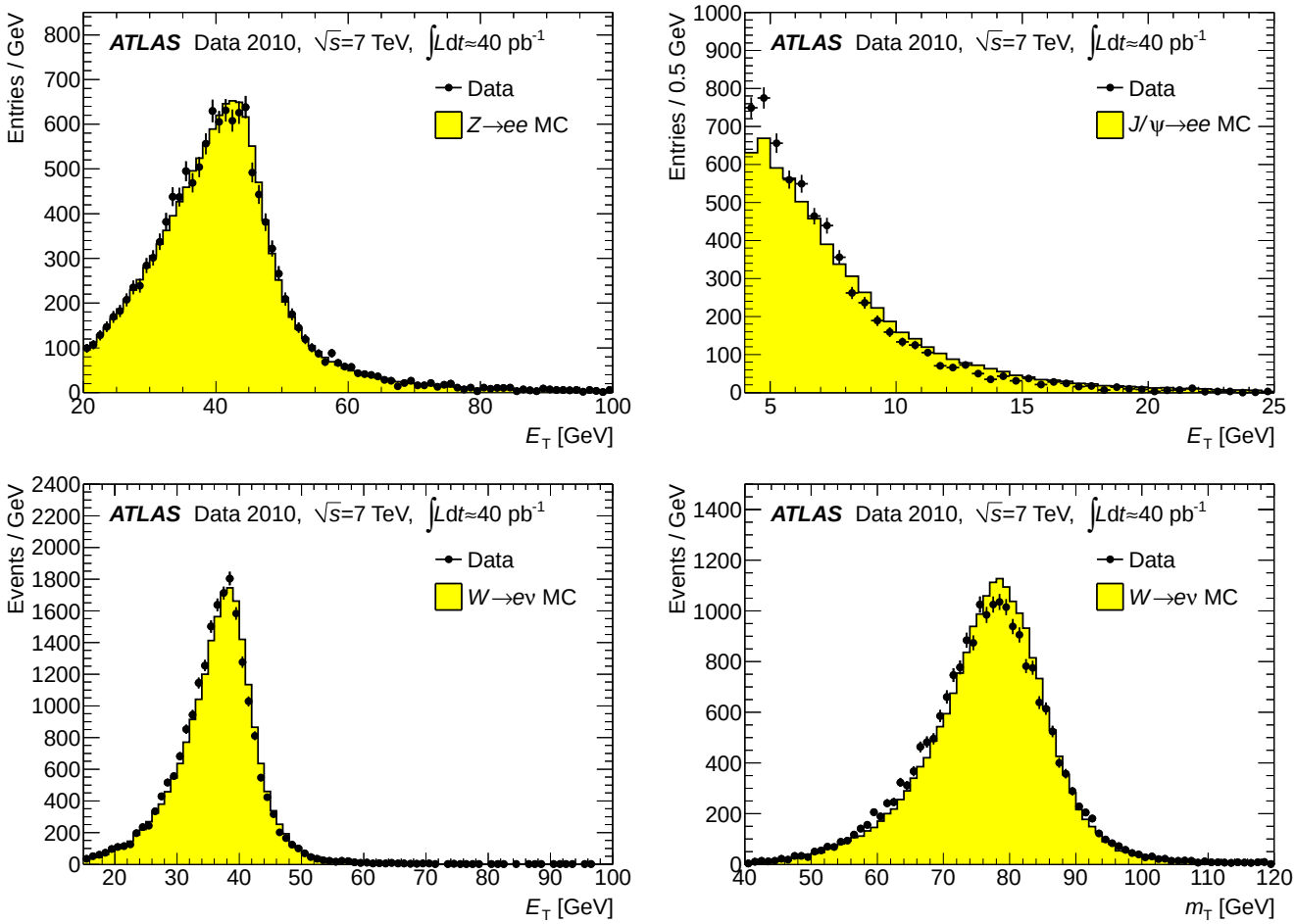

Fig. 11. Transverse energy spectra, compared between data and MC, for the selected electron probes passing *tight* identification cuts for the (top left) $Z \to ee$, (top right) $J/\psi \to ee$, and (bottom left) $W \to e\nu$ channels, together with (bottom right) the transverse mass distribution for the $W \to e\nu$ channel. The data points are plotted as full circles with statistical error bars, and the MC prediction, normalised to the number of data entries, as a filled histogram.

shape of the background vary significantly with the E_{T} of the probe, and depend strongly on the selection criteria applied to the probe. Therefore, the fit described above, and applied typically over $1.8 < m_{ee} < 4$ GeV, contains a third component, which is based on the spectrum of same-sign pairs in the data. Use of the same-sign sample has the advantage that it describes the shape of a large fraction of the background (random combinations of fake or real electrons), in particular in the signal region. The remaining background is modelled on each side of the signal region by an exponential, a Landau function or a Chebyshev polynomial.

Examples of the fit results are shown in Figure 12 for the $Z \to ee$ and in Figure 13 for the $J/\psi \to ee$ measurement.

Calorimeter isolation for the $W \to e\nu$ channel The $W \to e\nu$ sample is selected with very stringent $E_{\mathrm{T}}^{\mathrm{miss}}$ requirements. There is only a limited choice of observables to discriminate the isolated electron signal from the residual background from jets. One suitable observable, which is nevertheless slightly correlated with some of the electron identification variables, is the energy isolation measured in the calorimeter. This isolation variable, denoted hereafter $I_{\Delta R=0.4}$, is computed over a cone of half-angle $\Delta R = 0.4$ as follows. The transverse energies of all EM and hadronic calorimeter cells are summed except for those which are in the 5×7 EM calorimeter cells in $\Delta\eta\times\Delta\phi$ space around the cluster barycentre. This sum is normalised to the transverse energy of the EM cluster to yield $I_{\Delta R=0.4}$. For isolated electrons, the $I_{\Delta R=0.4}$ distribution is expected to peak at values close to zero, with a width determined by the combination of electronic noise, shower leakage, underlying event and pile-up contributions. For the background from jets, a much wider distribution is expected reaching values well beyond unity. The signal region is defined by requiring that the calorimeter isolation be below a certain threshold, typically 0.4. The residual background in the signal region is estimated using template distributions derived from data by requiring that the electron probes fail certain electron identification cuts. The obtained templates are normalized in the background region, above the

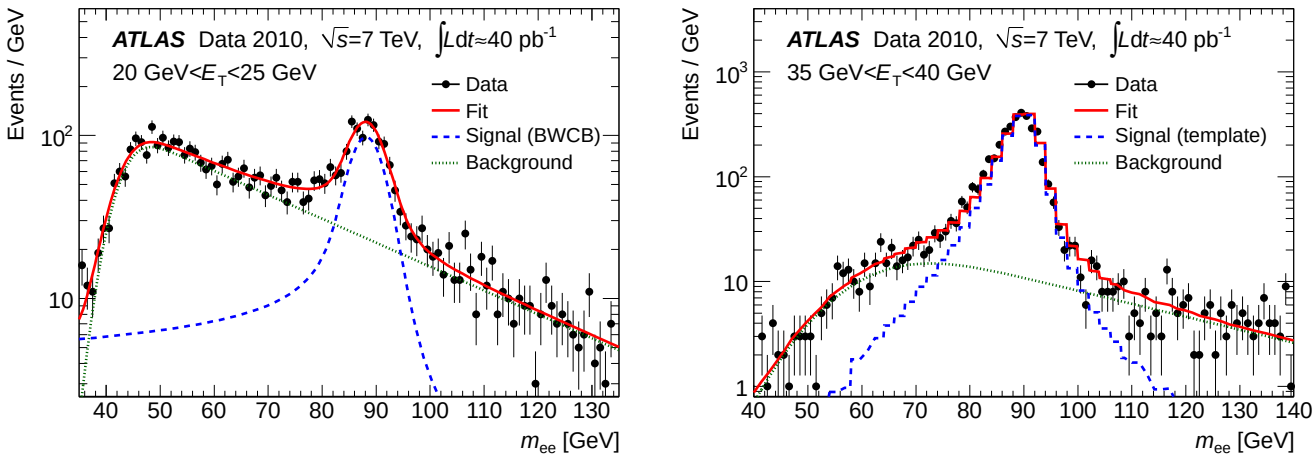

Fig. 12. The distributions of the dielectron invariant mass of $Z \to ee$ candidate events, before applying electron identification cuts on the probe electron, in the E_{T}-range (left) $20 - 25$ GeV and (right) $35 - 40$ GeV. The data distribution (full circles with statistical error bars) is fitted with the sum (full line) of a signal component (dashed line) modelled by a Breit-Wigner convolved with a Crystal Ball function (BWCB) on the left or by a MC template on the right, and a background component (dotted line) chosen here as an exponential decay function convolved with a Gaussian.

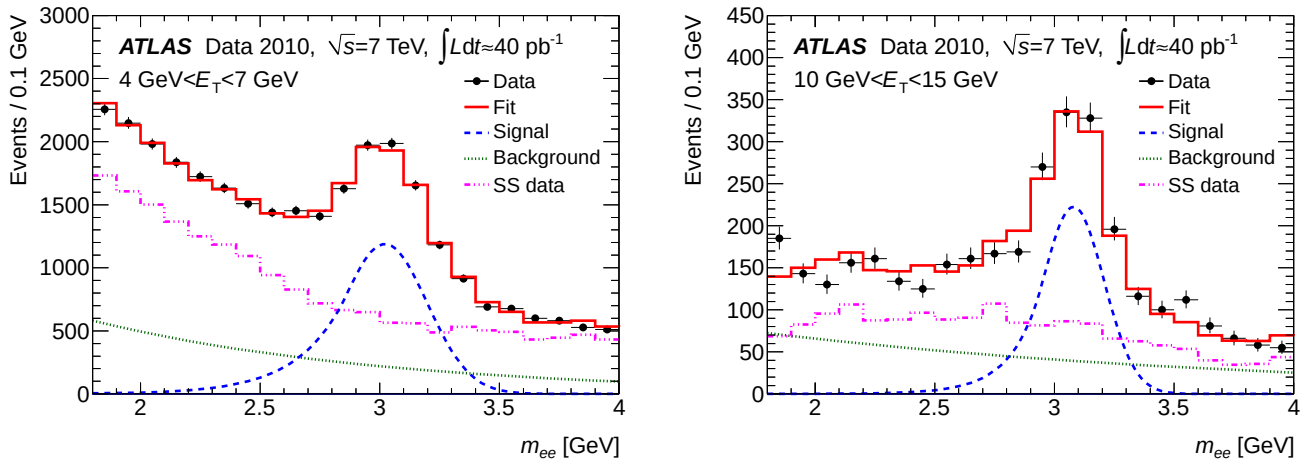

Fig. 13. The distributions of the dielectron invariant mass of $J/\psi \to ee$ candidate events, before applying electron identification cuts on the probe electron, in the E_{T}-range (left) $4 - 7$ GeV and (right) $10 - 15$ GeV. The data distribution (full circles with statistical error bars) is fitted with the sum (full line) of a signal component (dashed line) described by a Crystal Ball function and two background components, one taken from same-sign pairs in the data (dash-dotted line) and the remaining background modelled by an exponential function (dotted line).

chosen isolation threshold, to the number of selected electron probes.

Figure 14 shows the $I_{\Delta R=0.4}$ distribution for the data in two regions of phase space: a low-E_{T} bin, $20 < E_{\mathrm{T}} < 25$ GeV, where the background contribution is high, and the E_{T} bin, $35 < E_{\mathrm{T}} < 40$ GeV, which has the largest fraction of the signal statistics and a very high signal-to-background ratio.

Samples obtained after background subtraction Once the background subtraction procedure has been well defined, the next step in the process of measuring the efficiencies of the electron identification criteria (relative to electron reconstruction with additional track silicon hit requirements, as described above) is to define the total numbers of signal probes before and after applying the identification cuts, together with their statistical and systematic uncertainties. The ratios of these two numbers in each E_{T}-bin or η-bin are the efficiencies measured in data.

Table 5 shows several examples of the numbers of signal and background probes and of the corresponding signal-to-background ratios (S/B) for the three channels and for selected E_{T}-bins. The S/B ratios were found to be fairly uniform as a function of η for a given channel and E_{T}-bin. In contrast, as expected, the S/B ratios im-

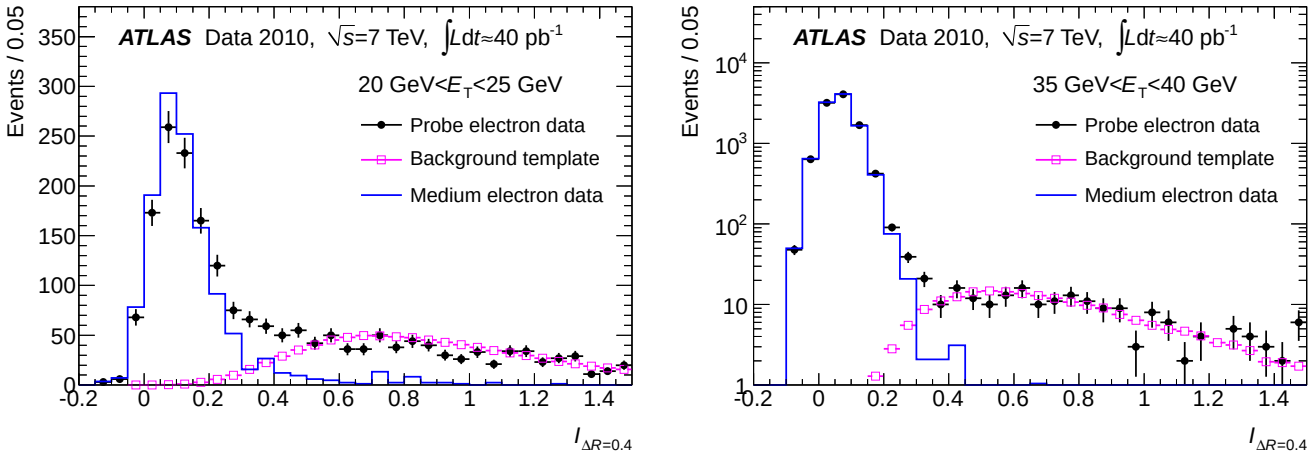

Fig. 14. The distributions of the calorimeter isolation variable, $I_{\Delta R=0.4}$ for the $W \to e\nu$ data sample for (left) $20 < E_{\mathrm{T}} < 25$ GeV and (right) $35 < E_{\mathrm{T}} < 40$ GeV. The full circles with statistical error bars correspond to the probe electrons before applying any identification cuts. The open squares show the corresponding background template, derived from data, normalised to the probe electron data in the region $I_{\Delta R=0.4} > 0.4$. To illustrate the expected shape of the $W \to e\nu$ signal, the distributions obtained for electron probes passing the *medium* identification cuts and normalised to the calculated $W \to e\nu$ signal are shown by full histograms.

Table 5. Numbers of signal and background probes and signal-over-background ratios (S/B), in different E_{T} ranges, for the $W \to e\nu$, $Z \to ee$, and $J/\psi \to ee$ channels. The errors are statistical only.

	$W \to e\nu$			$Z \to ee$		$J/\psi \to ee$	
E_{T} [GeV]	$15-20$	$20-25$	$35-40$	$20-25$	$40-45$	$4-7$	$15-20$
Signal	455 ± 20	1040 ± 30	10090 ± 100	870 ± 40	3710 ± 60	3900 ± 90	155 ± 15
Background	60 ± 10	140 ± 20	35 ± 6	460 ± 20	160 ± 20	3330 ± 190	120 ± 20
S/B	7.3 ± 1.0	7.3 ± 1.1	290 ± 50	1.9 ± 0.1	24 ± 3	1.2 ± 0.1	1.3 ± 0.3

prove considerably for high-E_{T} electrons from $W \to e\nu$ and $Z \to ee$ decay. The S/B ratios for the $W \to e\nu$ channel are considerably higher than for the $Z \to ee$ channel partly due to the higher W cross-section and partly because of the more stringent kinematic cuts applied to the neutrino tag (high $E_{\mathrm{T}}^{\mathrm{miss}}$ and $E_{\mathrm{T}}^{\mathrm{miss}}$ isolation) than to the electron tag in the $Z \to ee$ case. Such stringent kinematic cuts were not applied to the $Z \to ee$ channel because of limited statistics. At the much lower E_{T}-values covered by the $J/\psi \to ee$ channel, the S/B ratios are of order unity before applying any electron identification cuts and therefore the systematic uncertainties from the background subtraction procedure will be larger than for the $W \to e\nu$ and $Z \to ee$ channels, as shown in Subsection 6.2.3.

6.2.3 Systematic uncertainties

The dominant systematic uncertainties on the efficiency measurements described above are linked to the background subtraction from the probe samples, especially before applying the electron identification cuts. The background level under the signal was varied substantially to verify the stability of the background subtraction procedure, mostly by varying the cuts applied to the tag component of the event. Furthermore, the background subtraction method itself was also varied. The following sources of systematic uncertainties were considered:

- **Background level** The tag requirements (such as the electron identification level, *medium* or *tight*, for $Z \to ee$ and $J/\psi \to ee$, and the $E_{\mathrm{T}}^{\mathrm{miss}}$ and electron isolation, for $W \to e\nu$ and $Z \to ee$, respectively), were varied to induce variations of the background level under the signal.
- **Discriminating variable used in the background estimation** Several analysis choices were varied to estimate the uncertainty due to the discriminating variable chosen (calorimeter isolation for $W \to e\nu$ and invariant mass for $Z \to ee$ and $J/\psi \to ee$): the size of the signal window; the definition of the side-band region used for background subtraction for the η-dependent efficiencies in the $Z \to ee$ channel; the signal and background models (functions or templates) used in the fits for the E_{T}-dependent efficiencies in the $Z \to ee$ and $J/\psi \to ee$ channels; the definition of the isolation variable and the normalization region for the background template distributions for the $W \to e\nu$ channel.

– **Possible bias related to the method of the background subtraction** The possible bias from the correlations between the discriminating variable and the efficiencies themselves in the case of calorimeter isolation for the $W \to e\nu$ channel was studied by changing the selection used when producing the background isolation template (trigger stream, selection cuts).
Also, wherever feasible the possible bias of the efficiency extraction method (in particular the background subtraction) was also studied by repeating the measurements on simulated data and comparing the results to the MC truth. Typically, these *closure tests* were performed by mixing a high-statistics simulated signal sample and a background contribution with the background shape taken from a control region in data. The signal-to-background ratios were estimated from data and varied within reasonable limits. Any observed bias (defined as the difference of the measured and the true MC value in the test) was taken as an additional systematic uncertainty.

All combinations of the above variations were used to extract the efficiency, yielding about a hundred distinct measurements for each channel and for each kinematic bin. Given the complexity of the background subtraction procedure and the variety of kinematic configurations studied, no single preferred method for background subtraction could be defined. The central value of the measured efficiency was therefore defined as the mean of the distribution of all the efficiency values obtained through these variations and the systematic uncertainty was defined as the root mean square of the distributions. The statistical error is the mean of the statistical errors of all measurements corresponding to these analysis configurations.

Other potential sources of uncertainty were also checked but led to negligible contributions to the overall systematic uncertainty on the measurements:

– the impact of the energy-scale corrections discussed in Subsection 5.1 of this paper;
– the charge-dependence of the efficiencies in the $W \to e\nu$ measurement;
– the time-dependence of the efficiencies in the $W \to e\nu$ measurement;
– the size of the dead regions in the EM calorimeter;
– the amount of pile-up considered in the simulation.

When comparing the measured efficiencies with MC predictions, uncertainties related to the composition of the T&P sample potentially also need to be considered. In the case of the $J/\psi \to ee$ channel, the uncertainties on the **fraction of non-prompt J/ψ decays** [34] in the probe sample, which depend both on the kinematic bin and on the trigger conditions, are important. The uncertainties linked to the trigger, reconstruction and identification efficiencies of the non-prompt contribution are included. The effect of the modelling of the **mixture of triggers** used in the $W \to e\nu$ and $J/\psi \to ee$ channels was also studied. It is negligible in the $W \to e\nu$ case.

Table 6 illustrates the main components of the measurement uncertainties on the efficiency of the *tight* electron identification cuts for a few typical E_{T}-bins and for each channel. These uncertainties are somewhat larger than those for the *medium* cuts. The total uncertainties are computed as the quadratic sum of the statistical and the total systematic uncertainties. In the $Z \to ee$ and $J/\psi \to ee$ measurements, the total systematic uncertainty is obtained by adding linearly the closure test biases to the quadratic sum of all other components.

6.2.4 Measured efficiencies

The efficiencies of the *medium* and *tight* electron identification cuts as a function of E_{T} and η are shown in Figures 15, 16 and 17, respectively, for the $W \to e\nu$, $Z \to ee$ and $J/\psi \to ee$ channels. For the $J/\psi \to ee$ channel, only the measurements in four bins of E_{T} are presented due to the limited statistics, especially in the endcaps. For the $W \to e\nu$ and $Z \to ee$ channels, the measured efficiencies are compared directly to those expected from the MC simulations, whereas, for the $J/\psi \to ee$ channel, the measured efficiencies are compared to a weighted average of the efficiencies expected from prompt and non-prompt J/ψ production. As the *tight* cuts rely on tracking information, their performance is quite sensitive to interactions of electrons in the inner detector material. Their efficiency versus η is expected to be much less uniform than that of the *medium* cuts.

The observed differences between data and MC are discussed in terms of differences in electron identification variables in Subsection 6.2.5, in particular for the calorimeter shower shapes (used in the *medium* and *tight* selections) and for the ratio of high-threshold transition radiation hits to all hits in the TRT detector (used in the *tight* selection).

Overall, the η dependence of the identification efficiency is in good agreement between data and MC, with the most important deviations seen around the transition region between the barrel and endcap calorimeters. Larger differences are seen as a function of E_{T}, especially in the $W \to e\nu$ measurement, where the efficiency appears to decrease more at low E_{T} for data than for MC. More data are needed to properly understand this result.

The E_{T}-dependence of the efficiencies in the case of the $J/\psi \to ee$ measurements is in good agreement between data and MC. The shape can be attributed to the combination of the increasing contribution of non-isolated electrons from non-prompt J/ψ production (for which the efficiency decreases with E_{T} and is significantly lower at all E_{T} than for electrons from prompt J/ψ production) and to the rapidly improving efficiency for isolated electrons from prompt J/ψ production as E_{T} increases in this low-E_{T} range.

To check the consistency of the measurements, the electron and positron identification efficiency from the $W \to e\nu$ sample is compared, in Figure 18, for *medium* cuts as a function of E_{T} and for *tight* cuts as a function of η. Only statistical uncertainties are shown. The systematic uncertainties are in general significantly larger and correlated to some extent between the electron and positron measurements in the same E_{T}- or η-bin.

Table 6. Relative uncertainties (in %) on the measured efficiencies of the *tight* electron identification for $W \to e\nu$, $Z \to ee$, and $J/\psi \to ee$ decays for a few typical E_{T} bins (integrated over the full η-range). For the $J/\psi \to ee$ channel, the uncertainties affecting the MC prediction for the efficiency are also given.

	$W \to e\nu$			$Z \to ee$		$J/\psi \to ee$	
E_{T} range (GeV)	15-20	20-25	35-40	20-25	40-45	4-7	15-20
Statistics	3.0	1.7	0.3	3.5	0.9	2.5	9.9
Background level	1.2	1.3	0.3	4.4	0.9	2.2	3.1
Discriminating variable (nature, shape, range)	4.8	1.9	0.3	3.3	1.5	4.9	9.6
Possible bias of background subtraction	3.7	0.6	0.1	1.7	1.8	3.6	3.1
Total	7.1	3.1	0.5	8.0	3.6	9.3	16.5
MC statistics						0.2	0.8
Non-prompt J/ψ						5.2	7.7
Trigger mixture						5.1	2.4
MC total						7.3	8.1

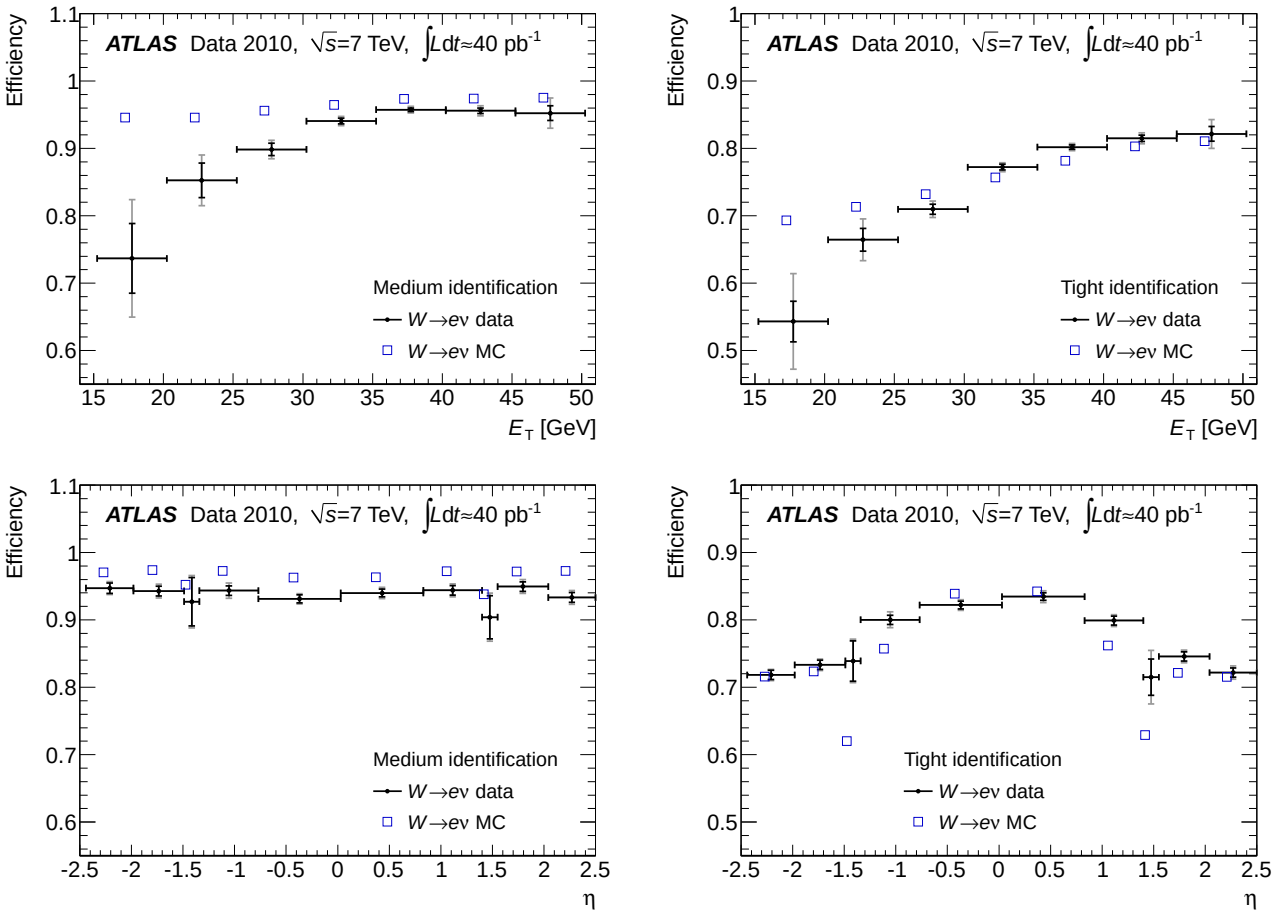

Fig. 15. Electron identification efficiencies measured from $W \to e\nu$ events and predicted by MC for (left) *medium* and (right) *tight* identification as a function (top) of E_{T} and integrated over $|\eta| < 2.47$ excluding the transition region $1.37 < |\eta| < 1.52$ and (bottom) of η and integrated over $20 < E_{\mathrm{T}} < 50$ GeV. The results for the data are shown with their statistical (inner error bars) and total (outer error bars) uncertainties. The statistical error on the MC efficiencies plotted as open squares is negligible. For clarity, the data and MC points are slightly displaced horizontally in opposite directions.

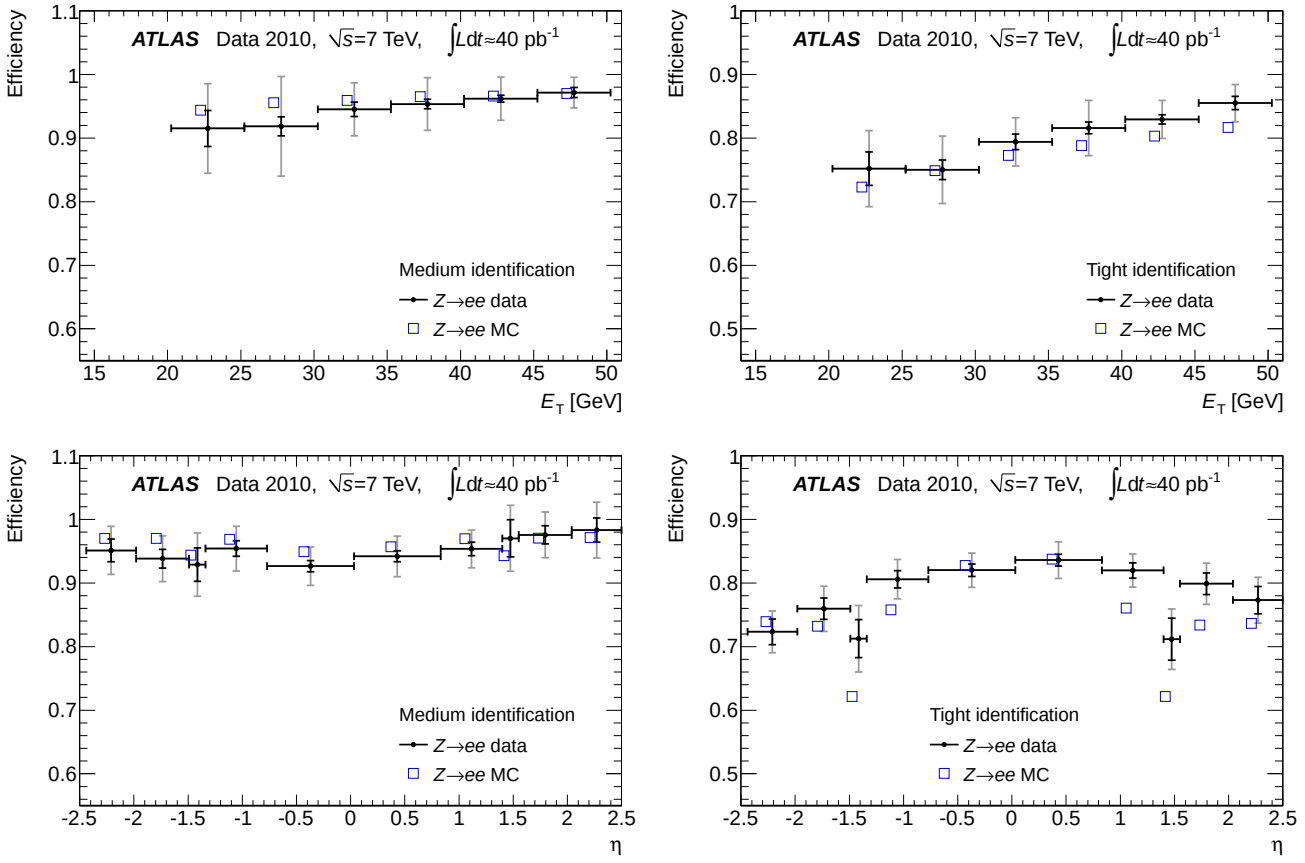

Fig. 16. Electron identification efficiencies measured from $Z \to ee$ events and predicted by MC for (left) *medium* and (right) *tight* identification as a function (top) of E_{T} and integrated over $|\eta| < 2.47$ excluding the transition region $1.37 < |\eta| < 1.52$ and (bottom) of η and integrated over $20 < E_{\mathrm{T}} < 50$ GeV. The results for the data are shown with their statistical (inner error bars) and total (outer error bars) uncertainties. The statistical error on the MC efficiencies plotted as open squares is negligible. For clarity, the data and MC points are slightly displaced horizontally in opposite directions.

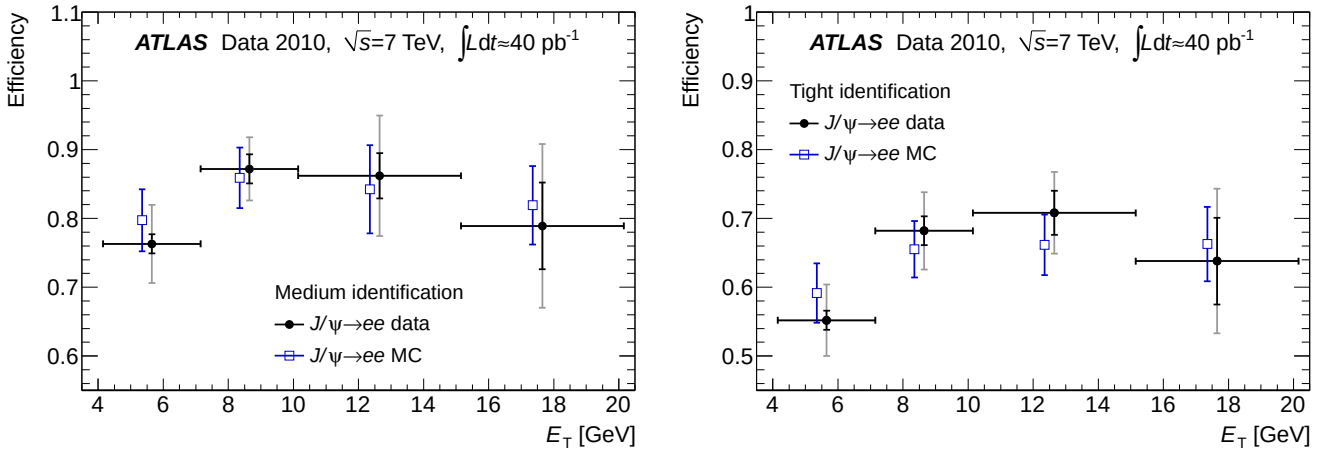

Fig. 17. Electron identification efficiencies measured from $J/\psi \to ee$ events and predicted by MC for (left) *medium* and (right) *tight* identification as a function of E_{T} and integrated over $|\eta| < 2.47$ excluding the transition region $1.37 < |\eta| < 1.52$. The results for the data are shown with their statistical (inner error bars) and total (outer error bars) uncertainties. The MC predictions are a weighted average of the efficiencies expected for prompt and non-prompt J/ψ production as explained in the text. The total error on the MC efficiencies plotted as open squares is also shown. For clarity, the data and MC points are slightly displaced horizontally in opposite directions.

The identification efficiency is expected to be higher for positrons than for electrons, since there are about 40% more positrons produced than electrons from W decays. Although the charge misidentification probability due to material effects is itself charge independent, the higher rate of $W^+ \to e^+\nu$ will induce more charge-misidentified probes in the electron sample than in the positron sample. The lower identification efficiency of these charge-misidentified electrons and positrons, also as a consequence of the material effects, leads to the expected difference in efficiency. This difference is estimated in MC simulation to be as large as 3% at high η-values where the amount of material is larger.

Since the dominant systematic uncertainties on the measurement arise from background subtraction and the number of events in the electron channel is smaller to start with, somewhat higher total uncertainties are observed in the measurements for electrons than for positrons. Small disagreements between data and MC in some η-bins indicate that there might be some contribution also from residual misalignment effects in the inner detector. The discrepancies observed in these few bins have, therefore, been added in quadrature to the total uncertainty for the charge-averaged measurements. It is expected that, with more data and improved inner-detector alignment constants, these discrepancies will be reduced.

The measurements for the $J/\psi \to ee$ channel have also been repeated for the *medium* identification criteria for different ranges of the measured pseudo-proper time, defined as

$$\tau_0 = \frac{L_{xy} \cdot m}{p_{\mathrm{T}}}, \tag{8}$$

where L_{xy} is the distance between the primary vertex and the extrapolated common vertex of the two electron candidates in the transverse plane, m is the reconstructed dielectron mass, and p_{T} is the reconstructed transverse momentum of the J/ψ candidate. Restricting the allowed pseudo-proper time to low (resp. high) values will improve the purity of the sample in terms of prompt (resp. non-prompt) J/ψ decays. The results of these measurements for the two highest statistics E_{T}-bins are compared in Figure 19 to the MC expectations for the weighted prompt plus non-prompt sample. The efficiencies expected for pure prompt and non-prompt J/ψ production are also shown. The efficiencies increase by several percent as the fraction of non-prompt decays decrease. The data show the same trend but more statistics are needed to measure clearly the variation of the efficiency with the fraction of decays from prompt J/ψ production in the data, and ultimately to separate the prompt and non-prompt J/ψ samples in the electron channel.

The $W \to e\nu$ and $Z \to ee$ samples cover very similar E_{T} and η-ranges, but they are not identical, so the one-dimensional identification efficiencies presented here are not expected to be exactly equal for a given bin in each channel. The measured identification efficiencies, integrated over η and for $20 < E_{\mathrm{T}} < 50$ GeV, are given in Table 7. Within their respective total uncertainties, the departures from the expected MC efficiencies observed for $W \to e\nu$ and $Z \to ee$ decays are compatible.

In contrast, the overlap between the $W \to e\nu$ and $J/\psi \to ee$ samples is limited to the E_{T}-range between 15 and 20 GeV, a region in which both samples suffer from quite low statistics and from large systematic uncertainties of about 10%. Moreover, the $J/\psi \to ee$ efficiency is the weighted average of prompt and non-prompt J/ψ decays, where only the former should be comparable to the electron efficiency obtained from $W \to e\nu$ decays. As the η-distributions of the two samples are not as similar as those of electrons from $W \to e\nu$ and $Z \to ee$ decays, the measured and expected identification efficiencies and their ratios are compared in the $15 - 20$ GeV E_{T}-bin in Table 8, but only over a limited η-range, $|\eta| < 0.8$. The MC efficiencies for W and prompt J/ψ production agree within a few percent. The measurement uncertainties are however still too large to draw firm conclusions.

6.2.5 Electron identification variables

The efficiencies measured in data and predicted by MC simulation presented in Figures 15, 16 and 17 manifest some marked differences. These differences are related to discrepancies in electron identification variables. In this section, the distributions of calorimeter shower shapes and of the high threshold hit fraction in the TRT are discussed.

Shower-shape distributions Lateral shower shapes in the EM calorimeter (listed in Table 1) play a crucial role in *medium* electron identification. They are extracted by the T&P method using $Z \to ee$ events in bins of the probe E_{T}, with tag requirements and probe definition as described in Section 6.2. The residual background, which could distort the measured distributions, is removed on a statistical basis using the technique of Ref. [35]. The method assigns a weight to each event based on a likelihood fit to the m_{ee} distribution in the range of $40 - 180$ GeV. These weights are then used to build the shape distributions. In order to obtain unbiased results, the correlations between the discriminating variable (m_{ee}) and the extracted variables (shower shapes) need to be negligible. This was verified using MC simulation.

To obtain bin-by-bin systematic uncertainties on the extracted electron shower shapes, different models for the signal and background dielectron-mass distributions were investigated as in the efficiency measurement.

The background subtraction method was validated by a closure test performed on MC events by applying the same procedure as used for the data. For some distributions, the observed bias is of the same order as the systematic uncertainty due to the choice of fit functions. The total bin-by-bin systematic uncertainties are calculated as the sum of these two uncertainties and are E_{T} dependent. They amount to $1 - 5\%$ in the E_{T}-bin $25 - 30$ GeV, and to $1 - 3\%$ in the bin $40 - 50$ GeV, depending on the shape variable. With the 2010 dataset, the total uncertainty is dominated by the statistical uncertainty.

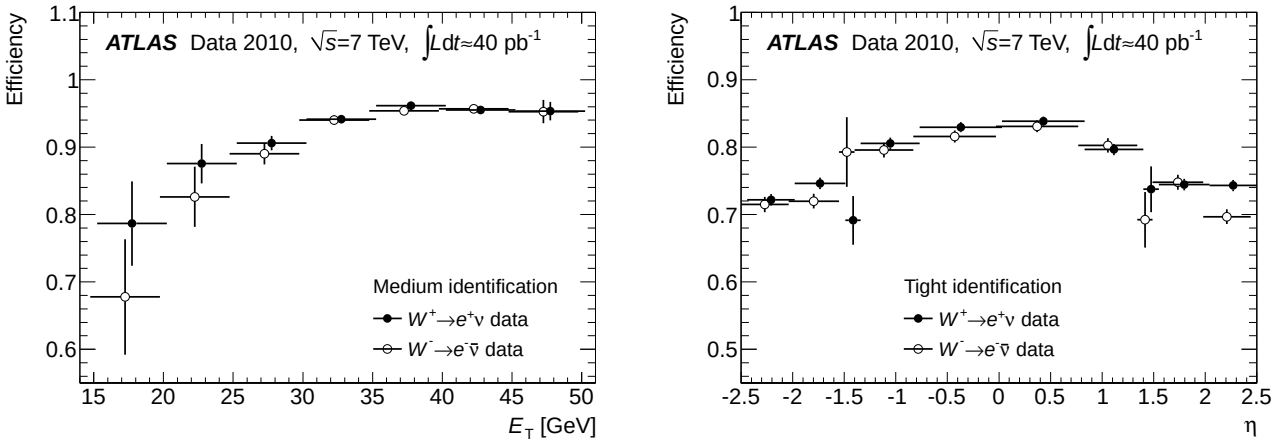

Fig. 18. Electron identification efficiencies measured separately for positrons (full circles) and electrons (open circles) from $W \to e\nu$ events (left) for *medium* identification as a function of E_{T} and integrated over $|\eta| < 2.47$ excluding the transition region $1.37 < |\eta| < 1.52$ and (right) for *tight* identification as a function of η and integrated over $20 < E_{\mathrm{T}} < 50$ GeV. The results are shown with statistical uncertainties only. For clarity, the electron and positron data points are slightly displaced horizontally in opposite directions.

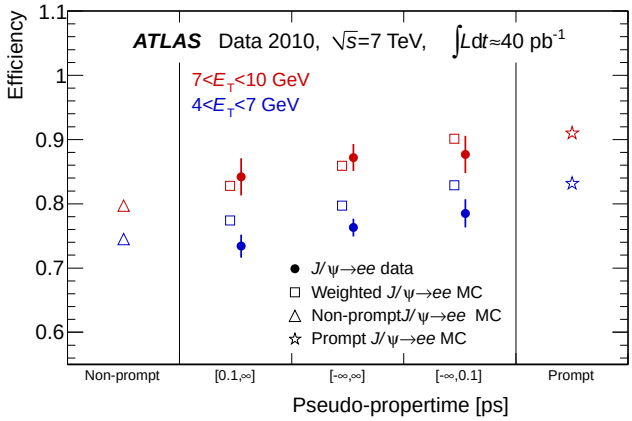

Fig. 19. Electron identification efficiencies measured from $J/\psi \to ee$ events and predicted by MC for *medium* identification for two E_{T} ranges: $4 < E_{\mathrm{T}} < 7$ GeV (lower points) and $7 < E_{\mathrm{T}} < 10$ GeV (higher points) for different ranges of pseudo-proper time. The left-most open triangles show the MC efficiencies for a pure non-prompt J/ψ sample, while the right-most open stars show them for a pure prompt J/ψ sample integrated over all pseudo-proper time values. The MC predictions plotted as open squares in the middle are weighted averages of the efficiency values expected for prompt and non-prompt J/ψ production as explained in the text. The results for the data are shown with statistical uncertainties only. For clarity, the data and MC points are slightly displaced horizontally in opposite directions.

Table 7. *Medium* and *tight* identification efficiencies (in %) measured in the $W \to e\nu$ and $Z \to ee$ channels, integrated over $|\eta| < 2.47$ excluding the transition region between barrel and endcap EM calorimeters at $1.37 < |\eta| < 1.52$ and over $20 < E_{\mathrm{T}} < 50$ GeV. The measured data efficiencies are given together with the expected efficiencies from MC simulation and with their ratios. For the data measurements and for the ratios, the first error corresponds to the statistical uncertainty and the second to the systematic uncertainty. For the MC expectations, the statistical uncertainties are negligible.

Selection	Channel	Data [%]	MC [%]	Ratio
Medium	$W \to e\nu$	$94.1 \pm 0.2 \pm 0.6$	96.9	$0.971 \pm 0.002 \pm 0.007$
	$Z \to ee$	$94.7 \pm 0.4 \pm 1.5$	96.3	$0.984 \pm 0.004 \pm 0.015$
Tight	$W \to e\nu$	$78.1 \pm 0.2 \pm 0.6$	77.5	$1.009 \pm 0.003 \pm 0.007$
	$Z \to ee$	$80.7 \pm 0.5 \pm 1.5$	78.5	$1.028 \pm 0.006 \pm 0.016$

Table 8. *Medium* and *tight* identification efficiencies (in %) measured in the $W \to e\nu$ and $J/\psi \to ee$ channels, integrated over $|\eta| < 0.8$ and $15 < E_{\mathrm{T}} < 20$ GeV. The measured data efficiencies are given together with the expected efficiencies from MC simulation and their ratios. The MC efficiencies for the $J/\psi \to ee$ channel are obtained as a weighted average of the expected prompt and non-prompt components (see text). For completeness, the expected MC efficiencies for a pure sample of $J/\psi \to ee$ decays from prompt J/ψ production are also given. For the data measurements and for the ratios, the first error corresponds to the statistical uncertainty and the second to the systematic uncertainty. For the MC expectations, the statistical uncertainties are negligible.

Selection	Channel	Data [%]	MC [%]	Ratio	MC [%] prompt J/ψ
Medium	$W \to e\nu$	$75.8 \pm 8.8 \pm 8.1$	94.9	$0.80 \pm 0.09 \pm 0.07$	
	$J/\psi \to ee$	$80.0 \pm 7.3 \pm 10.2$	81.9	$0.98 \pm 0.09 \pm 0.14$	92.9
Tight	$W \to e\nu$	$61.9 \pm 6.0 \pm 7.0$	78.3	$0.79 \pm 0.08 \pm 0.09$	
	$J/\psi \to ee$	$68.1 \pm 7.3 \pm 9.0$	69.1	$0.99 \pm 0.11 \pm 0.15$	78.3

The extracted electron shower shapes from data are compared to the MC prediction in Figure 20. There are significant differences visible for all extracted variables. The distributions of the strip and middle layer shapes are wider and are also shifted in data towards the background region. As a result, somewhat lower *medium* efficiencies are observed in data compared to MC. Currently, work is ongoing to refine the calorimeter simulation to achieve a better description of the shower shape distributions.

High threshold TRT hits The *tight* identification cuts listed in Table 1 rely on more stringent matching cuts between the inner detector and EM calorimeter measurements and on additional measurements in the inner detector. In particular, an advantage of the ATLAS detector is the capability of the TRT to discriminate against hadronic fakes over $|\eta| < 2.0$ using information on the ratio of high threshold transition radiation hits over all hits (f_{HT}).

Figure 21 shows the f_{HT} distribution in two η-regions for electron candidates from $Z \to ee$ decays, selected by a T&P analysis and having momenta in the range $10 - 100$ GeV, where the probability for producing high-threshold hits (HT) from transition radiation (TR) in the TRT straws is uniform. This probability is in the range of $0.2 - 0.25$, to be compared with about 0.05 for pion candidates in the same momentum range [36].

The HT probability for electrons varies with the radiator type, therefore it is expected to be different in the barrel and endcap regions. It also depends on the varying incidence angle of the charged particles on the straws. The observed HT probability as a function of η is not modelled perfectly in the barrel TRT by the MC simulation, but the largest effect is the higher than predicted HT probability in the TRT endcap wheels. For $|\eta| > 1.0$, the HT probability in data is measured to be significantly higher than in MC, resulting in a better than expected electron identification performance.

6.3 Electron identification efficiency in the forward region

The efficiency of electron identification in the forward region outside the tracking acceptance is studied using $Z \to ee$ events, in two bins of pseudorapidity: $2.5 < |\eta| < 3.2$ corresponding to EMEC-IW and $3.2 < |\eta| < 4.9$ corresponding to the FCal detectors.

6.3.1 Probe selection and background subtraction

The tag electron is required to be a *central tight* electron with $E_{\mathrm{T}} > 25$ GeV and $|\eta| < 2.47$ excluding the transition region $1.37 < |\eta| < 1.52$, while the probe is a *forward* electron candidate with $E_{\mathrm{T}} > 20$ GeV and $2.5 < |\eta| < 4.9$. With this selection, a total of 5469 pairs in the m_{ee} range $59-124$ GeV are found in the EMEC-IW, while 3429 pairs are found in the range $50 - 160$ GeV in the FCal.

The background is subtracted using an unbinned maximum likelihood fit to the dielectron invariant mass. The same methodology is used as in Subsection 6.2. The signal is modelled either by a Breit-Wigner convolved with a Crystal Ball function or by a MC template. The background is described either by a template from data requiring that the pair fails certain selection cuts or by different analytical functions.

The systematic uncertainties are studied by varying the signal integration range, the background level via the tag requirements (isolation and E_{T} cut), the signal and background shapes and the fit range. The systematic uncertainties vary between 2.5% and 4.5% and are typically larger for FCal and for *forward tight* selection. The possible bias of the method was also studied by a closure test and yielded an additional systematic uncertainty of $3 - 4\%$.

6.3.2 Results

Table 9 presents the measured and expected efficiency values. The electron identification efficiency in the forward region is not perfectly reproduced by MC. This can be

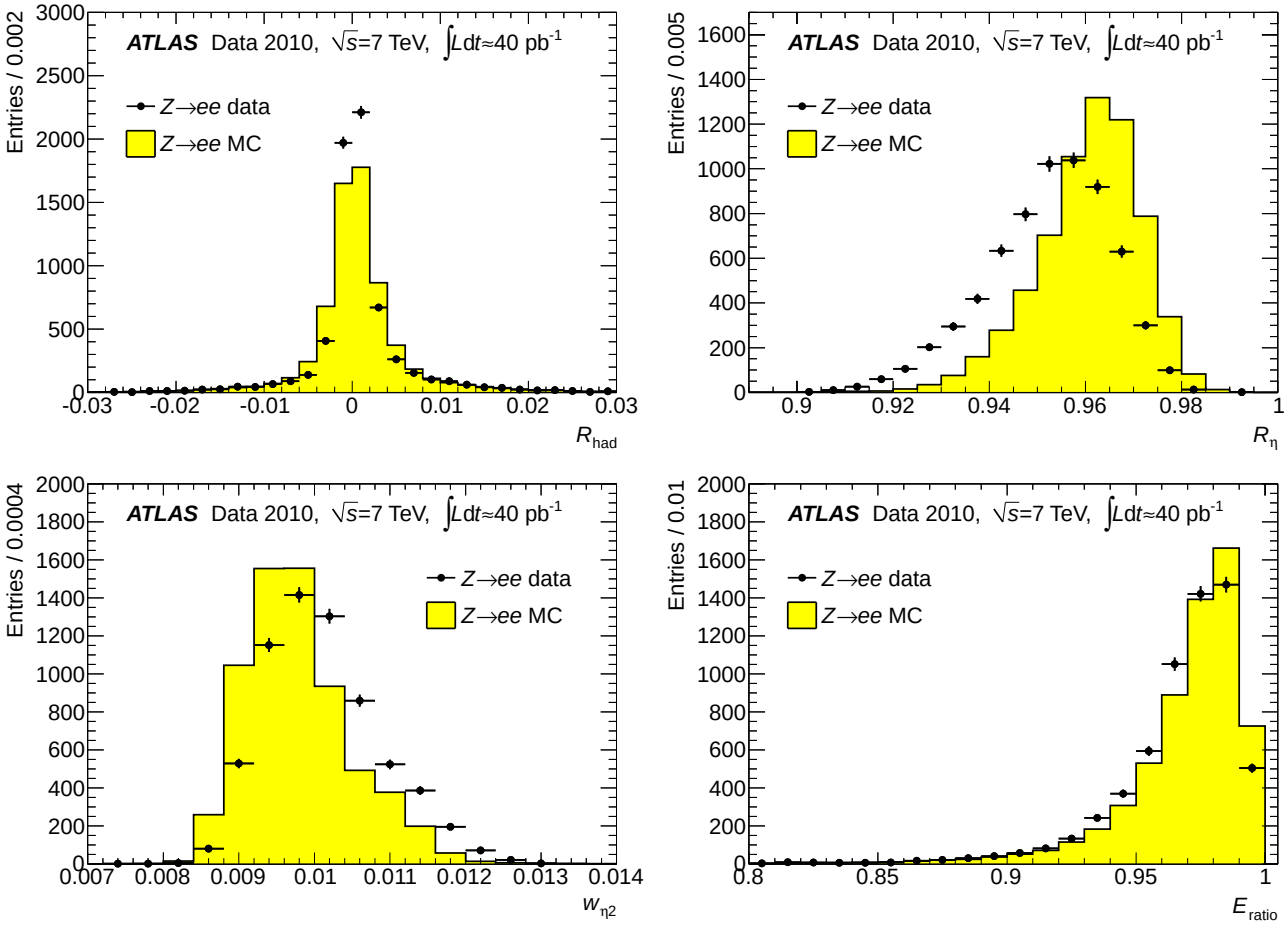

Fig. 20. Electron shower shapes from $Z \to ee$ events for probe electrons in the range $E_{\mathrm{T}} = 40 - 50$ GeV: (top left) R_{had} hadronic leakage, (top right) R_{η} and (bottom left) $w_{\eta 2}$ middle-layer variables, (bottom right) E_{ratio} strip-layer variable. The data points are plotted as full circles with error bars, representing the total statistical and systematic uncertainties. The MC predictions, normalised to the number of data entries, are shown by filled histograms.

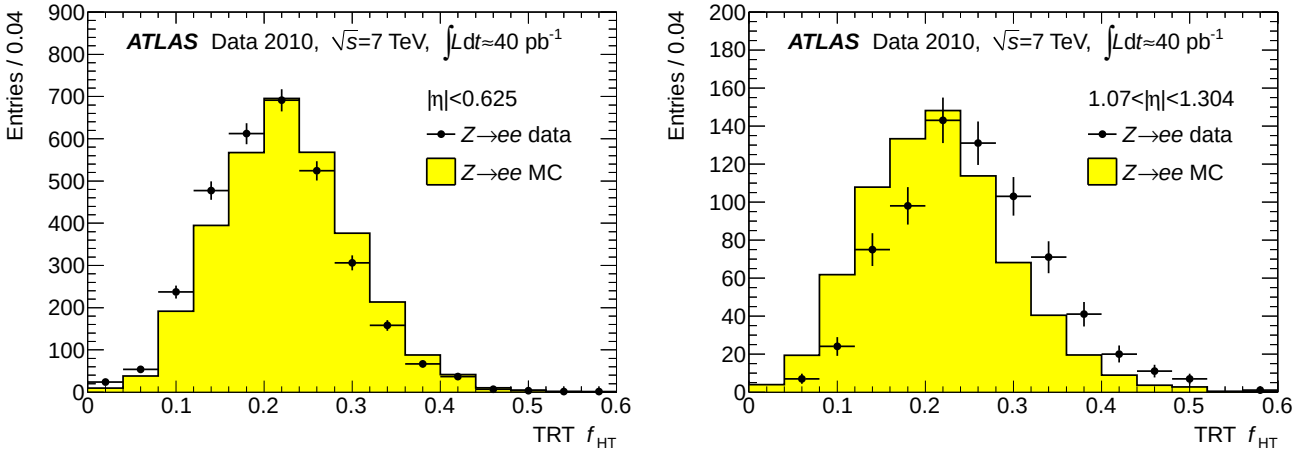

Fig. 21. Distributions of the fraction of high-threshold hits in the TRT measured from $Z \to ee$ data and compared to MC prediction for (left) $|\eta| < 0.625$ and (right) $1.07 < |\eta| < 1.304$. The data points are plotted as full circles with statistical error bars, while the MC predictions, normalised to the number of data entries, as filled histograms.

Table 9. Identification efficiencies (in %) in the forward region measured from $Z \to ee$ events integrated over $E_{\mathrm{T}} > 20$ GeV and over $2.5 < |\eta| < 3.2$ for EMEC-IW and over $3.2 < |\eta| < 4.9$ for FCal. The measured data efficiencies are given together with the expected efficiencies from MC simulation and with their ratios. For the data measurements and for the ratios, the first error corresponds to the statistical and the second to the systematic uncertainty. For the MC expectations, the statistical uncertainties are about 0.1%.

Detector	Selection	Data [%]	MC [%]	Ratio
EMEC-IW	*Forward loose*	$83.1 \pm 1.3 \pm 4.6$	90.7	$0.916 \pm 0.014 \pm 0.051$
	Forward tight	$58.2 \pm 1.4 \pm 3.6$	72.8	$0.800 \pm 0.019 \pm 0.050$
FCal	*Forward loose*	$87.5 \pm 2.6 \pm 7.2$	89.0	$0.983 \pm 0.029 \pm 0.081$
	Forward tight	$53.2 \pm 2.3 \pm 4.3$	59.4	$0.896 \pm 0.038 \pm 0.072$

explained by the observation that the showers are broader and longer in data. The origin of these discrepancies is under investigation.

6.4 Reconstruction efficiency of central electrons

In this section, the electron reconstruction efficiencies are studied with respect to sliding-window clusters in the EM calorimeter using $Z \to ee$ decays following the methodology of Subsection 6.2. The reconstruction efficiency defined this way measures the combined electron track reconstruction and track–cluster matching efficiencies.

6.4.1 Probe selection and background subtraction

To measure the electron reconstruction efficiency with or without the additional requirements on the number of silicon hits on the associated track introduced in Subsection 6.2.1, the requirements on the probe electron are released to consider all sliding-window EM clusters. Using *tight* tag electrons having $E_{\mathrm{T}} = 20 - 50$ GeV, this leads to almost 20000 probes, with $500 - 4000$ per pseudorapidity bin. The S/B ratio in the dielectron mass range $80 < m_{ee} < 100$ GeV varies from about 1 (for *medium* tags) to $6 - 10$ (for *tight* isolated tags).

As for the identification efficiency measurement, the average of measurements, made with different configurations of the background level and the size of the signal window in the dielectron mass, was used to assess the reconstruction efficiencies. In particular, *medium* or *tight* tags, with or without track or cluster isolation requirements, and with or without a cut on the transverse impact parameter significance, and five different integration ranges are considered. The root mean square of these 80 measurements is assigned as the systematic error on the reconstruction efficiency due to the stability of the background estimation on data.

The potential biases of the background subtraction method were also studied in a MC closure test. The best closure was achieved using an exponential shape to describe the background and a Breit-Wigner convolved with a Crystal Ball function (to account for detector effects) to model the signal. The difference between the efficiency estimated using such a fit and the true efficiency is considered as an additional systematic uncertainty. The largest bias found in any η bin is taken for all bins. It amounts to 1.5% (0.5%) when the requirements on silicon hits on the track are (not) required.

6.4.2 Results and pseudorapidity dependence

The measured reconstruction efficiency in data, shown in Figure 22, is compatible with the MC predictions, though slightly higher values are observed in data, especially in the region $0.8 < |\eta| < 2.01$ when requirements on the numbers of silicon hits on the track are applied. The globally averaged efficiencies in the full pseudorapidity range of $|\eta| < 2.47$ are given in Table 10. The efficiency loss due to requirements on the numbers of silicon hits is smaller than 3% in the barrel and reaches almost 10% in the highest $|\eta|$ bins.

The results for the data are shown with their statistical (inner error bars) and total (outer error bars) uncertainties. The statistical error on the MC efficiencies is negligible.

6.5 Charge misidentification probability

Mismeasurement of the charge happens primarily when the electron interacts early in the detector and the EM shower produces several high p_{T} tracks. The primary track is then either not available or a different subsequent track is matched to the EM cluster. The charge misidentification probability, $\epsilon_{\mathrm{QmisID}}$, is defined as the fraction of electrons with incorrectly measured charge with respect to all electrons, and depends on the applied electron identification cuts. In particular, track quality cuts decrease $\epsilon_{\mathrm{QmisID}}$ significantly.

In this study $\epsilon_{\mathrm{QmisID}}$ is investigated comparing same-sign pairs to all (same-sign and opposite-sign) pairs in $Z \to ee$ events at four levels of electron identification: reconstruction, silicon hit requirements on the track as defined in Subsection 6.2.1, and the standard *medium* and *tight* selections.

6.5.1 Probe selection and background subtraction

To ensure a well measured tag electron charge, the tag is confined to the barrel region of $|\eta| < 1.37$. No correction is applied for the misidentification of the *tight* central

Table 10. Efficiency (in %) for electron reconstruction only and with requirements on the number of silicon hits on the track, measured from $Z \to ee$ events, integrated over $20 < E_{\mathrm{T}} < 50$ GeV and over $|\eta| < 2.47$, excluding the transition region between barrel and endcap EM calorimeters at $1.37 < |\eta| < 1.52$. The measured data efficiencies are given together with the expected efficiencies from MC simulation and with their ratios. For the data measurements and for the ratios, the first error corresponds to the statistical uncertainty and the second one to the systematic uncertainty. For the MC expectations, the statistical uncertainties are negligible.

Selection	Data [%]	MC [%]	Ratio
Electron reconstruction	$98.7 \pm 0.1 \pm 0.2$	98.3	$1.005 \pm 0.001 \pm 0.002$
Track silicon hit requirements	$94.3 \pm 0.2 \pm 0.8$	93.1	$1.013 \pm 0.002 \pm 0.008$

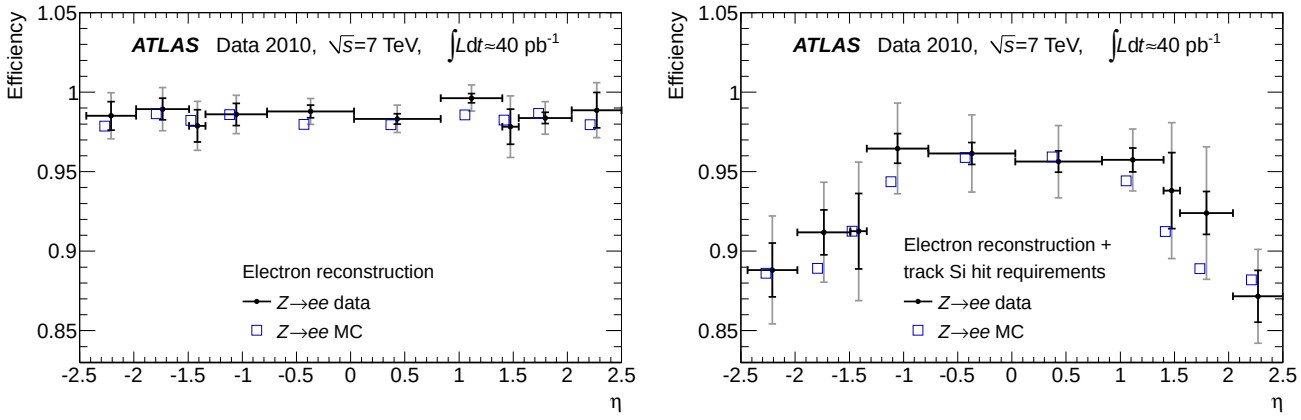

Fig. 22. Reconstruction efficiency measured from $Z \to ee$ events and predicted by MC as a function of the cluster pseudorapidity and integrated over $20 < E_{\mathrm{T}} < 50$ GeV (left) for electron reconstruction only and (right) after applying requirements on the number of silicon hits on the track. The results for the data are shown with their statistical (inner error bars) and total (outer error bars) uncertainties. The statistical error on the MC efficiencies plotted as open squares is negligible. For clarity, the data and MC points are slightly displaced horizontally in opposite directions.

tag electron. This increases the measured probability with respect to the "true" value by about 0.2%.

The selection of same-sign pairs favours background over signal. This is especially problematic when studying $\epsilon_{\mathrm{QmisID}}$ at early stages of electron identification. Additional requirements beyond the standard $Z \to ee$ selection described in Subsection 6.2.1 are necessary. To extract the central value for $\epsilon_{\mathrm{QmisID}}$, a low missing transverse momentum of $E_{\mathrm{T}}^{\mathrm{miss}} < 25$ GeV is required, reducing significantly the $W \to e\nu$ background. To assess the systematic uncertainty due to background contamination, four other variants of the selection were studied with different requirements on $E_{\mathrm{T}}^{\mathrm{miss}}$, calorimeter isolation and the tag E_{T}. With the standard $Z \to ee$ selection, about 1000 probes are found, with a S/B ratio of 0.34, in the same-sign sample at the reconstruction level in the full pseudorapidity range. Applying the $E_{\mathrm{T}}^{\mathrm{miss}}$ and calorimeter isolation cuts, the S/B ratio improves to 0.74 but the number of probes drops to 550. The available statistics is much more limited at *medium* ($100-140$ same-sign pairs) and *tight* (about 40 same-sign pairs) identification levels, where $\mathrm{S/B} = 5.5-8$ is achieved.

The remaining background is subtracted by a template method at early identification stages where the available statistics is sufficient, and by a side-band method at the *medium* and *tight* identification levels. For the fit, the background template is derived from data events where the tag electron candidate fires an EM trigger (with no trigger-level electron identification) but fails both the *medium* offline selection and the isolation cut. The signal template is obtained from $Z \to ee$ MC. The number of signal events is counted within $75 < m_{ee} < 100$ GeV.

The systematic uncertainties are estimated by varying the tag requirements, the signal and background templates (or the side-bands), and the m_{ee} signal window, in a way similar to that described in Subsection 6.2.

6.5.2 Results and pseudorapidity dependence

The results for globally averaged charge misidentification probabilities are summarised in Table 11. Overall the data-MC agreement is good. The measurement in the data tends to be slightly lower than the MC prediction.

The same techniques are applied in bins of electron probe pseudorapidity. The results are displayed in Figure 23 at the two extreme levels of selection: after electron reconstruction only and after *tight* identification.

The measurements are repeated separately for the cases of positive (negative) tag electrons, measuring $\epsilon_{\mathrm{QmisID}}$ predominantly for true negative (positive) probes.

Table 11. Charge misidentification probabilities (in %) at different levels of electron identification from $Z \to ee$ events, integrated over $|\eta| < 2.47$ excluding the transition region between barrel and endcap EM calorimeters at $1.37 < |\eta| < 1.52$ and over $E_{\mathrm{T}} > 20$ GeV. The measured data efficiencies are given together with the expected efficiencies from MC simulation. For the data measurements, the first error corresponds to the statistical uncertainty and the second one to the systematic uncertainty. For the MC expectations, the statistical uncertainties are negligible.

Selection	Data [%]	MC [%]
Electron reconstruction	$2.17 \pm 0.25 \pm 0.28$	2.73
Track silicon hit requirements	$1.13 \pm 0.21 \pm 0.16$	1.28
Medium identification	$1.04 \pm 0.11 \pm 0.14$	1.20
Tight identification	$0.37 \pm 0.07 \pm 0.11$	0.50

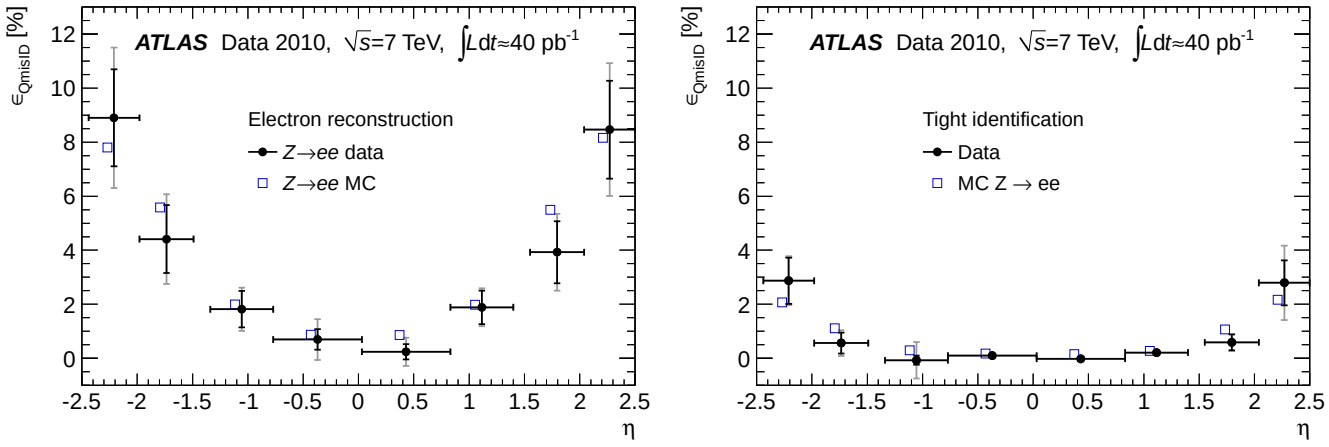

Fig. 23. Electron charge misidentification probability measured from $Z \to ee$ events as a function of pseudorapidity and integrated over $E_{\mathrm{T}} > 20$ GeV (left) after electron reconstruction and (right) after *tight* selection. Data points are shown with statistical (inner error bars) and total uncertainties (outer error bars). The MC expectation is indicated by open squares. For clarity, the data and MC points are slightly displaced horizontally in opposite directions.

The results for the different charges agree within uncertainties.

These measurements, even if limited in precision, do not show any significant difference between the charge misidentification probability in data and MC. An $\epsilon_{\mathrm{QmisID}}$ of about 0.5% is observed in the barrel and up to 8% at high η for candidates at the reconstruction level. The measured probability decreases to about 0.2% in the barrel and around 2% in the endcaps after *tight* identification cuts.

6.6 Electron trigger efficiency

The trigger efficiency is defined as the fraction of identified offline electrons that fire a given trigger. Here, the *medium* and *tight* selections are considered as offline benchmarks, for which the most commonly used triggers were designed to have close to 100% efficiency in the plateau E_{T}-region, starting typically about 5 GeV above the trigger threshold. The main sources of inefficiency are readout problems of the L1 system, lower reconstruction efficiency (especially for tracking) at trigger level due to timing constraints, and small differences of the electron identification variables between trigger and offline [12,13].

In 2010, events with high-p_{T} electrons were primarily selected by the *e15_medium* and *e20_loose* triggers, which require an electron candidate reconstructed at the event filter (EF) level with $E_{\mathrm{T}} > 15$ and 20 GeV passing the *medium* and *loose* identification cuts, respectively. In this section, their efficiency measurements using $W \to e\nu$ and $Z \to ee$ decays are reported.

6.6.1 Probe selection

To measure the trigger efficiency, electron probes in the range $E_{\mathrm{T}} > 15$ GeV are checked for a match to an EF electron fulfilling the trigger selection. The angular distance ΔR between the trigger and offline electron candidates is computed using the tracking variables. It is required to be smaller than 0.15. This loose cut results in a 100% matching efficiency. Note that, while all three levels of the trigger have to be implicitly satisfied, no particular matching is required between the offline electron and L1 or L2 trigger objects.

$W \to e\nu$ and $Z \to ee$ candidates are selected following Subsection 6.2. The *medium* or *tight* requirement on the probe electron candidate increases significantly the purity of the sample. For example, in the $Z \to ee$ channel the background fraction of *tight–medium* pairs is below 1%. Therefore, no background subtraction is applied when obtaining the central values of the trigger efficiency measurements.

Systematic uncertainties due to the tag requirements, the m_{ee} requirement in the probe definition for the $Z \to ee$ channel, the background contamination, the energy-scale uncertainty and the trigger–offline matching requirement have been studied and found to be less than 0.1% in total.

6.6.2 Results and E_{T} dependence

Figure 24 shows the trigger efficiency as a function of the offline E_{T} of *tight* probe electrons for the e15_medium and e20_loose triggers. As expected, both triggers are very efficient in the plateau region starting 5 GeV above the trigger threshold.

The integrated efficiencies in the plateau region are summarized in Table 12 together with the data/MC efficiency ratios. As correctly predicted by the MC, the trigger efficiency is slightly higher with respect to the offline *tight* selection than to the *medium* one. This is mainly due to the E/p cut present in the *tight* selection; it rejects electrons with a large amount of bremsstrahlung radiation which are less efficiently reconstructed by the fast L2 tracking algorithm. The W and Z results are compatible for all four trigger–offline selection combinations.

The small difference in the trigger efficiency behaviour between data and MC could be explained by the presence of dead L1 trigger towers[7] not simulated in MC (typically well below the per mille level), differences at the few % level in the electron energy-scale calibration introduced by the offline data reprocessing, and differences in the distribution of identification variables between data and MC as discussed in Subsection 6.2.5.

7 Conclusions

The performance of the ATLAS detector for electrons in 2010 was presented, using $W \to e\nu$, $Z \to ee$ and $J/\psi \to ee$ decays in pp collision data.

An inter-alignment of the inner detector and the EM calorimeter has been performed and resulted in a track–cluster matching accuracy close to the MC expectation. Further improvements are in progress, in particular for ϕ in the endcap regions covering $1.52 < |\eta| < 2.47$.

The electron energy scale has been determined in bins of pseudorapidity with a precision of $0.3-1.6\%$ in the central region over $|\eta| < 2.47$ and $2-3\%$ in the forward regions over $2.5 < |\eta| < 4.9$, with a residual non-uniformity in ϕ below 1% in the central region. After applying the 2010 in-situ calibration, the constant term of the energy resolution is measured to be $(1.2 \pm 0.1(\mathrm{stat}) \pm 0.3(\mathrm{syst}))\%$ in the barrel EM calorimeter covering $|\eta| < 1.37$, increasing to 1.8% in the endcaps and to about 3% in the forward regions. With the additional statistics being collected in 2011, the energy-scale will be determined in (η, ϕ) bins and the knowledge of the material in front of the calorimeter will be improved. The EM calorimeter constant term should therefore be determined more accurately and should decrease towards its design value of 0.7%.

Precise measurements as a function of η and E_{T} have been performed for a variety of components of the electron selection efficiency in the central region over $|\eta| < 2.47$. The electron identification efficiency has been measured with a total accuracy better than 1% for the highest-statistics bin of $E_{\mathrm{T}} = 35 - 40$ GeV using $W \to e\nu$ events, and to about 10% for the lowest-statistics bin of $E_{\mathrm{T}} = 15 - 20$ GeV using $W \to e\nu$ and $J/\psi \to ee$ events.

The differences between calorimeter shower shapes measured in data and predicted by MC have been an ongoing topic of study since the first runs collecting cosmic-ray events [37,38]. These are now precisely measured for $|\eta| < 2.47$ using the $Z \to ee$ channel which allows to extract unbiased distributions for the electron probes.

Other important components of the electron selection efficiency have been determined with good accuracy in the $Z \to ee$ channel, even though they are more difficult to extract: the electron reconstruction efficiency, the efficiency of the track silicon hit requirements, and the probability of electron charge misidentification. The trigger efficiency measurements have established very high plateau efficiencies of the electron triggers used in 2010.

In the forward region over $2.5 < |\eta| < 4.9$, despite the difficulty of the measurements without any tracking information and with non-optimal EM calorimeter measurements, the clear signal observed from $Z \to ee$ decays has been used to also measure the electron identification efficiencies with reasonable accuracy. The disagreements between data and MC are found to be larger in this region.

In parallel, work is ongoing to measure precisely the material in the detector and to refine the description of the detector material, the simulation of the EM shower development in the calorimeter, and the transition radiation production in the TRT. This will ultimately improve the description of the data by the MC.

The accuracy of all efficiency measurements will benefit from the much larger statistics available in 2011. Two-dimensional measurements in (E_{T},η) space with finer η granularity will be obtained with accuracies better than 1%, allowing a more precise identification of the sources of the different E_{T}-dependence of the efficiencies in data and MC.

In the low-E_{T} range, the $J/\psi \to ee$ measurements require a substantial increase in statistics to measure the reconstruction and identification efficiencies in the low-E_{T} region, important for Higgs-boson searches. In this region, the material effects are large, the energies are closer to the

[7] These dead L1 trigger towers were repaired in the 2010 – 2011 LHC winter shutdown.

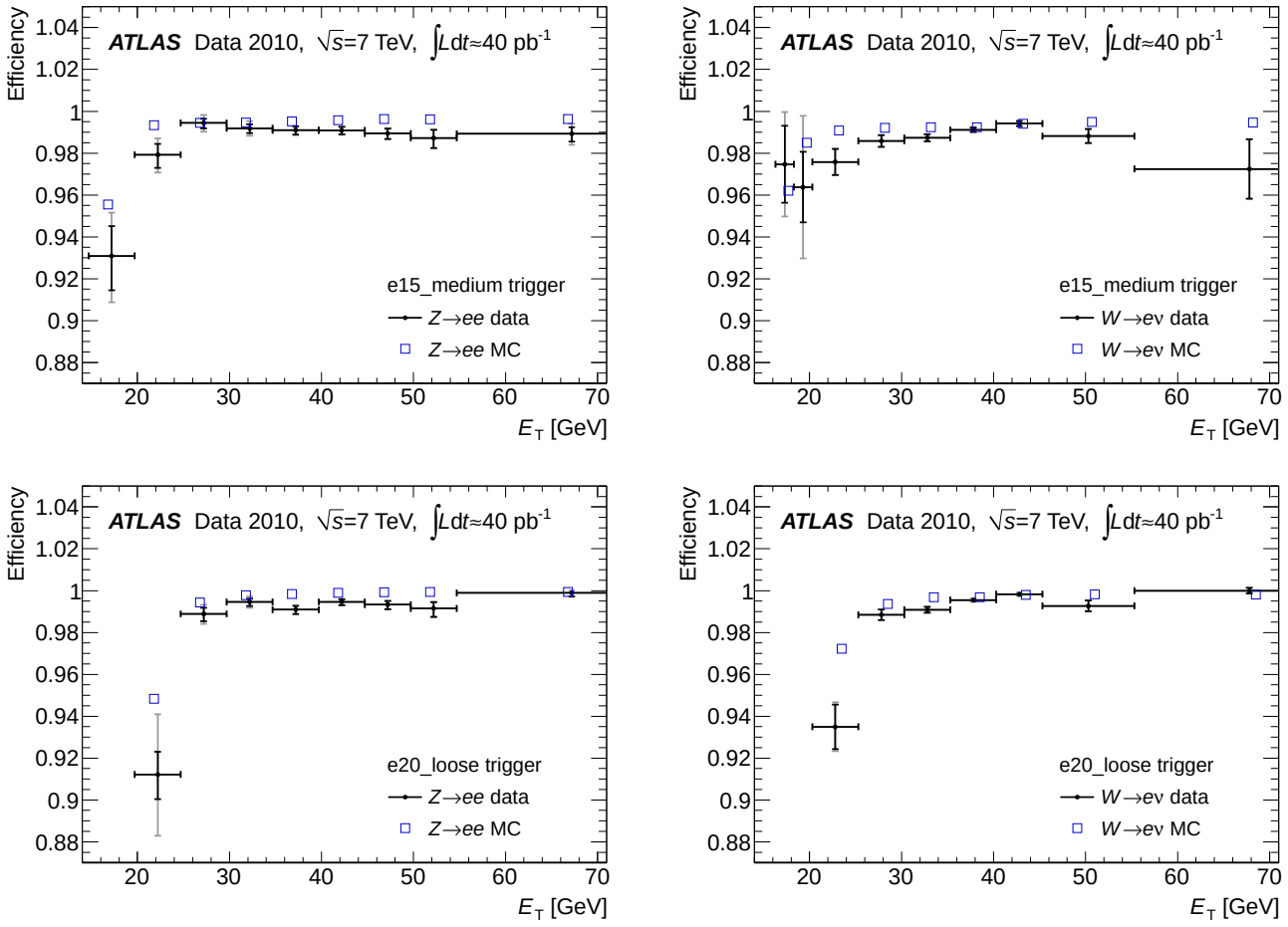

Fig. 24. Efficiency with respect to offline *tight* electrons for (top) e15_medium and (bottom) e20_loose triggers measured from (left) $Z \to ee$ and (right) $W \to e\nu$ events as a function of the offline electron E_{T} and integrated over $|\eta| < 2.47$ excluding the transition region between the barrel and endcap EM calorimeters. The results for the data are shown with their statistical (inner error bars) and total (outer error bars) uncertainties. The statistical error on the MC efficiencies plotted as open squares is negligible. For clarity, the data and MC points are slightly displaced horizontally in opposite directions.

Table 12. Efficiency (in %) for the e15_medium (e20_loose) trigger measured from $W \to e\nu$ and $Z \to ee$ events, integrated over $|\eta| < 2.47$ excluding the transition region between barrel and endcap EM calorimeters at $1.37 < |\eta| < 1.52$ and over $E_{\mathrm{T}} > 20$ (25) GeV. The measured data efficiencies are given together with the expected efficiencies from MC simulation and with their ratios. For the data measurements and for the ratios, the error corresponds to the statistical uncertainty. The systematic errors are below 0.1%. For the MC expectations, the statistical uncertainties are negligible.

Trigger	Probe	Channel	Data [%]	MC [%]	Ratio
e15_medium	Offline *medium*	$W \to e\nu$	98.48 ± 0.08	98.76	0.997 ± 0.001
		$Z \to ee$	98.67 ± 0.10	99.24	0.994 ± 0.001
	Offline *tight*	$W \to e\nu$	98.96 ± 0.07	99.30	0.997 ± 0.001
		$Z \to ee$	99.02 ± 0.09	99.54	0.995 ± 0.001
e20_loose	Offline *medium*	$W \to e\nu$	99.28 ± 0.05	99.52	0.998 ± 0.001
		$Z \to ee$	99.11 ± 0.08	99.73	0.994 ± 0.001
	Offline *tight*	$W \to e\nu$	99.42 ± 0.05	99.69	0.997 ± 0.001
		$Z \to ee$	99.33 ± 0.08	99.83	0.995 ± 0.001

reconstruction threshold, and the identification cuts are stringent.

In the high-E_{T} range, above that explored in this paper, much higher statistics of $W \to e\nu$ and $Z \to ee$ decays are required to extend the measurements to a region important for exotic searches where the efficiencies are expected to become asymptotically flat with E_{T}.

Overall, the performance of the ATLAS inner detector and EM calorimeters has been firmly established using the limited electron statistics from W, Z and J/ψ decays obtained in 2010 at $\sqrt{s} = 7$ TeV corresponding to about 40 pb^{-1}. The agreement between the measurements in data and the predictions of the MC is generally good, leading to only small corrections of the MC electron performance estimates in physics analyses.

8 Acknowledgements

We thank CERN for the very successful operation of the LHC, as well as the support staff from our institutions without whom ATLAS could not be operated efficiently.

We acknowledge the support of ANPCyT, Argentina; YerPhI, Armenia; ARC, Australia; BMWF, Austria; ANAS, Azerbaijan; SSTC, Belarus; CNPq and FAPESP, Brazil; NSERC, NRC and CFI, Canada; CERN; CONICYT, Chile; CAS, MOST and NSFC, China; COLCIENCIAS, Colombia; MSMT CR, MPO CR and VSC CR, Czech Republic; DNRF, DNSRC and Lundbeck Foundation, Denmark; ARTEMIS, European Union; IN2P3-CNRS, CEA-DSM/IRFU, France; GNAS, Georgia; BMBF, DFG, HGF, MPG and AvH Foundation, Germany; GSRT, Greece; ISF, MINERVA, GIF, DIP and Benoziyo Center, Israel; INFN, Italy; MEXT and JSPS, Japan; CNRST, Morocco; FOM and NWO, Netherlands; RCN, Norway; MNiSW, Poland; GRICES and FCT, Portugal; MERYS (MECTS), Romania; MES of Russia and ROSATOM, Russian Federation; JINR; MSTD, Serbia; MSSR, Slovakia; ARRS and MVZT, Slovenia; DST/NRF, South Africa; MICINN, Spain; SRC and Wallenberg Foundation, Sweden; SER, SNSF and Cantons of Bern and Geneva, Switzerland; NSC, Taiwan; TAEK, Turkey; STFC, the Royal Society and Leverhulme Trust, United Kingdom; DOE and NSF, United States of America.

The crucial computing support from all WLCG partners is acknowledged gratefully, in particular from CERN and the ATLAS Tier-1 facilities at TRIUMF (Canada), NDGF (Denmark, Norway, Sweden), CC-IN2P3 (France), KIT/GridKA (Germany), INFN-CNAF (Italy), NL-T1 (Netherlands), PIC (Spain), ASGC (Taiwan), RAL (UK) and BNL (USA) and in the Tier-2 facilities worldwide.

References

1. The ATLAS Collaboration, *The ATLAS Experiment at the CERN Large Hadron Collider*, JINST **3** (2008) S08003.
2. The ATLAS Collaboration, *Expected performance of the ATLAS experiment : detector, trigger and physics*, CERN-OPEN-2008-20 , arXiv:0901.0512 [hep-ex].
3. T. Sjostrand, S. Mrenna, and P. Z. Skands, *PYTHIA 6.4 Physics and Manual*, JHEP **0605** (2006) 026, arXiv:hep-ph/0603175.
4. The ATLAS Collaboration, *The ATLAS Simulation Infrastructure*, Eur. Phys. J. **C70** (2010) 823–874, arXiv:1005.4568 [physics.ins-det].
5. S. Agostinelli et al., *GEANT4: A simulation toolkit*, Nucl. Instrum. Meth. **A506** (2003) 250–303.
6. The ATLAS Collaboration, *Charged-particle multiplicities in pp interactions at $\sqrt{s} = 900$ GeV measured with the ATLAS detector at the LHC*, Phys. Lett. **B688** (2010) 21–42, arXiv:1003.3124 [hep-ex].
7. The ATLAS Collaboration, *Charged-particle multiplicities in pp interactions measured with the ATLAS detector at the LHC*, New J. Phys. **13** (2011) 053033, arXiv:1012.5104 [hep-ex].
8. The ATLAS Collaboration, *Study of the Material Budget in the ATLAS Inner Detector with K^0_S decays in collision data at $\sqrt{s} = 900$ GeV*, ATLAS-CONF-2010-019.
9. The ATLAS Collaboration, *A measurement of the material in the ATLAS inner detector using secondary hadronic interactions*, JINST **7** (2012) P01013, arXiv:1110.6191 [hep-ex].
10. The ATLAS Collaboration, *Photon conversion at $\sqrt{s} = 900$ GeV measured with the ATLAS detector*, ATLAS-CONF-2010-007.
11. The ATLAS Collaboration, *Probing the material in front of the ATLAS electromagnetic calorimeter with energy flow from $\sqrt{s} = 7$ TeV minimum bias events*, ATLAS-CONF-2010-037.
12. The ATLAS Collaboration, *Performance of the ATLAS Trigger System in 2010*, Eur. Phys. J. **C72** (2012) 1849, arXiv:1110.1530 [hep-ex].
13. The ATLAS Collaboration, *Performance of the Electron and Photon Trigger in p-p Collisions at $\sqrt{s} = 7$ TeV with the ATLAS Detector at the LHC*, ATLAS-CONF-2011-114.
14. ATLAS Collaboration, *Expected electron performance in the ATLAS experiment*, ATL-PHYS-PUB-2011-006.
15. W. Lampl et al., *Calorimeter Clustering Algorithms : Description and Performance*, ATL-LARG-PUB-2008-002.
16. The ATLAS Collaboration, *Readiness of the ATLAS Liquid Argon Calorimeter for LHC Collisions*, Eur. Phys. J. **C70** (2010) 723–753, arXiv:0912.2642 [physics.ins-det].
17. The ATLAS Collaboration, *Expected photon performance in the ATLAS experiment*, ATL-PHYS-PUB-2011-007.
18. The ATLAS Collaboration, *ATLAS detector and physics performance: Technical Design Report, Vol. 1.* Technical Design Report ATLAS. CERN, Geneva, 1999. CERN/LHCC 99-14, ATLAS TDR 14.
19. M. Aharrouche et al., *Energy linearity and resolution of the ATLAS electromagnetic barrel calorimeter in an electron test-beam*, Nucl.Instrum.Meth. **A568** (2006) 601–623, arXiv:physics/0608012.
20. J. Colas et al., *Response Uniformity of the ATLAS Liquid Argon Electromagnetic Calorimeter*,

Nucl.Instrum.Meth. **A582** (2007) 429–455, arXiv:0709.1094 [physics.ins-det].
21. M. Aharrouche et al., *Measurement of the response of the ATLAS liquid argon barrel calorimeter to electrons at the 2004 combined test-beam*, Nucl.Instrum.Meth. **A614** (2010) 400–432.
22. B. Aubert et al., *Performance of the ATLAS electromagnetic calorimeter end-cap module 0*, Nucl.Instrum.Meth. **A500** (2003) 178–201.
23. B. Aubert et al., *Performance of the ATLAS electromagnetic calorimeter barrel module 0*, Nucl.Instrum.Meth. **A500** (2003) 202–231.
24. The ATLAS Collaboration, *Data-quality requirements and event cleaning for jets and missing transverse energy reconstruction with the ATLAS detector in Proton-Proton collisions at a center-of-mass energy of* $\sqrt{s} = 7$ *TeV*, ATLAS-CONF-2010-038.
25. D. Banfi et al., *Cell response equalization of the ATLAS electromagnetic calorimeter without the direct knowledge of the ionization signals*, J. Instrum. **1** (2006) P08001.
26. C. Collard et al., *Prediction of signal amplitude and shape for the ATLAS electromagnetic calorimeter*, ATL-LARG-PUB-2007-010.
27. H. Abreu et al., *Performance of the electronic readout of the ATLAS liquid argon calorimeters*, JINST **5** (2010) P09003.
28. M.J. Oreglia, *A study of the reactions* $\psi' \to \gamma\gamma\psi$, Ph.D. thesis, SLAC-R-236 (1980), Appendix D.
29. J.E. Gaiser, *Charmonium spectroscopy from radiative decays of the J/ψ and ψ′*, Ph.D. thesis, SLAC-R-255 (1982), Appendix F.
30. The ALEPH, DELPHI, L3, OPAL and SLD Collaborations, *Precision electroweak measurements on the Z resonance*, Physics Reports **427** (2006) 257–454, arXiv:hep-ex/0509008.
31. The CDF Collaboration, *First measurement of inclusive W and Z cross sections from Run II of the Fermilab Tevatron Collider*, Phys. Rev. Lett. **94** (2005) 091803, arXiv:hep-ex/0406078.
32. The D0 Collaboration, *Measurement of the shape of the boson rapidity distribution for* $p\bar{p} \to Z/\gamma^* \to e^+e^- + X$ *events produced at* $\sqrt{s}$ *of 1.96 TeV*, Phys. Rev. **D76** (2007) 012003, arXiv:hep-ex/0702025.
33. C. Blocker, *Treatment of Errors in Efficiency Calculations*, CDF/MEMO/STATISTICS/PUBLIC/7168, 2004.
34. The ATLAS Collaboration, *Measurement of the differential cross-sections of inclusive, prompt and non-prompt J/ψ production in proton-proton collisions at* $\sqrt{s} = 7$ *TeV*, Nucl. Phys. **B850** (2011) 387–444, arXiv:1104.3038 [hep-ex].
35. M. Pivk and F.R. Le Diberder, *sPlot : a statistical tool to unfold data distributions*, Nucl. Istrum. Meth. **A555** (2005) 356–369, arXiv:physics/0402083.
36. The ATLAS Collaboration, *Particle identification performance of the ATLAS Transition Radiation Tracker*, ATLAS-CONF-2011-128.
37. The ATLAS Collaboration, *Studies of the performance of the ATLAS detector using cosmic-ray muons*, Eur. Phys. J. **C71** (2011) 1593, arXiv:1011.6665 [physics.ins-det].
38. The ATLAS Collaboration, *Performance of the ATLAS Detector using First Collision Data*, JHEP **1009** (2010) 056, arXiv:1005.5254 [hep-ex].

The ATLAS Collaboration

G. Aad[48], B. Abbott[111], J. Abdallah[11], A.A. Abdelalim[49], A. Abdesselam[118], O. Abdinov[10], B. Abi[112], M. Abolins[88], H. Abramowicz[153], H. Abreu[115], E. Acerbi[89a,89b], B.S. Acharya[164a,164b], D.L. Adams[24], T.N. Addy[56], J. Adelman[175], M. Aderholz[99], S. Adomeit[98], P. Adragna[75], T. Adye[129], S. Aefsky[22], J.A. Aguilar-Saavedra[124b,a], M. Aharrouche[81], S.P. Ahlen[21], F. Ahles[48], A. Ahmad[148], M. Ahsan[40], G. Aielli[133a,133b], T. Akdogan[18a], T.P.A. Åkesson[79], G. Akimoto[155], A.V. Akimov [94], A. Akiyama[67], M.S. Alam[1], M.A. Alam[76], J. Albert[169], S. Albrand[55], M. Aleksa[29], I.N. Aleksandrov[65], F. Alessandria[89a], C. Alexa[25a], G. Alexander[153], G. Alexandre[49], T. Alexopoulos[9], M. Alhroob[20], M. Aliev[15], G. Alimonti[89a], J. Alison[120], M. Aliyev[10], P.P. Allport[73], S.E. Allwood-Spiers[53], J. Almond[82], A. Aloisio[102a,102b], R. Alon[171], A. Alonso[79], M.G. Alviggi[102a,102b], K. Amako[66], P. Amaral[29], C. Amelung[22], V.V. Ammosov[128], A. Amorim[124a,b], G. Amorós[167], N. Amram[153], C. Anastopoulos[29], L.S. Ancu[16], N. Andari[115], T. Andeen[34], C.F. Anders[20], G. Anders[58a], K.J. Anderson[30], A. Andreazza[89a,89b], V. Andrei[58a], M-L. Andrieux[55], X.S. Anduaga[70], A. Angerami[34], F. Anghinolfi[29], N. Anjos[124a], A. Annovi[47], A. Antonaki[8], M. Antonelli[47], A. Antonov[96], J. Antos[144b], F. Anulli[132a], S. Aoun[83], L. Aperio Bella[4], R. Apolle[118,c], G. Arabidze[88], I. Aracena[143], Y. Arai[66], A.T.H. Arce[44], J.P. Archambault[28], S. Arfaoui[29,d], J-F. Arguin[14], E. Arik[18a,*], M. Arik[18a], A.J. Armbruster[87], O. Arnaez[81], C. Arnault[115], A. Artamonov[95], G. Artoni[132a,132b], D. Arutinov[20], S. Asai[155], R. Asfandiyarov[172], S. Ask[27], B. Åsman[146a,146b], L. Asquith[5], K. Assamagan[24], A. Astbury[169], A. Astvatsatourov[52], G. Atoian[175], B. Aubert[4], B. Auerbach[175], E. Auge[115], K. Augsten[127], M. Aurousseau[145a], N. Austin[73], G. Avolio[163], R. Avramidou[9], D. Axen[168], C. Ay[54], G. Azuelos[93,e], Y. Azuma[155], M.A. Baak[29], G. Baccaglioni[89a], C. Bacci[134a,134b], A.M. Bach[14], H. Bachacou[136], K. Bachas[29], G. Bachy[29], M. Backes[49], M. Backhaus[20], E. Badescu[25a], P. Bagnaia[132a,132b], S. Bahinipati[2], Y. Bai[32a], D.C. Bailey[158], T. Bain[158], J.T. Baines[129], O.K. Baker[175], M.D. Baker[24], S. Baker[77], E. Banas[38], P. Banerjee[93], Sw. Banerjee[172], D. Banfi[29], A. Bangert[137], V. Bansal[169], H.S. Bansil[17], L. Barak[171], S.P. Baranov[94], A. Barashkou[65], A. Barbaro Galtieri[14], T. Barber[27], E.L. Barberio[86], D. Barberis[50a,50b], M. Barbero[20], D.Y. Bardin[65], T. Barillari[99], M. Barisonzi[174], T. Barklow[143], N. Barlow[27], B.M. Barnett[129], R.M. Barnett[14], A. Baroncelli[134a], G. Barone[49], A.J. Barr[118], F. Barreiro[80], J. Barreiro Guimarães da Costa[57], P. Barrillon[115], R. Bartoldus[143], A.E. Barton[71], D. Bartsch[20], V. Bartsch[149], R.L. Bates[53], L. Batkova[144a], J.R. Batley[27], A. Battaglia[16], M. Battistin[29], G. Battistoni[89a], F. Bauer[136], H.S. Bawa[143,f], B. Beare[158], T. Beau[78], P.H. Beauchemin[118], R. Beccherle[50a], P. Bechtle[41], H.P. Beck[16], M. Beckingham[48], K.H. Becks[174], A.J. Beddall[18c], A. Beddall[18c], S. Bedikian[175], V.A. Bednyakov[65], C.P. Bee[83], M. Begel[24], S. Behar Harpaz[152], P.K. Behera[63], M. Beimforde[99], C. Belanger-Champagne[85], P.J. Bell[49], W.H. Bell[49], G. Bella[153], L. Bellagamba[19a], F. Bellina[29], M. Bellomo[29], A. Belloni[57], O. Beloborodova[107], K. Belotskiy[96], O. Beltramello[29], S. Ben Ami[152], O. Benary[153], D. Benchekroun[135a], C. Benchouk[83], M. Bendel[81], N. Benekos[165], Y. Benhammou[153], D.P. Benjamin[44], M. Benoit[115], J.R. Bensinger[22], K. Benslama[130], S. Bentvelsen[105], D. Berge[29], E. Bergeaas Kuutmann[41], N. Berger[4], F. Berghaus[169], E. Berglund[49], J. Beringer[14], K. Bernardet[83], P. Bernat[77], R. Bernhard[48], C. Bernius[24], T. Berry[76], A. Bertin[19a,19b], F. Bertinelli[29], F. Bertolucci[122a,122b], M.I. Besana[89a,89b], N. Besson[136], S. Bethke[99], W. Bhimji[45], R.M. Bianchi[29], M. Bianco[72a,72b], O. Biebel[98], S.P. Bieniek[77], K. Bierwagen[54], J. Biesiada[14], M. Biglietti[134a,134b], H. Bilokon[47], M. Bindi[19a,19b], S. Binet[115], A. Bingul[18c], C. Bini[132a,132b], C. Biscarat[177], U. Bitenc[48], K.M. Black[21], R.E. Blair[5], J.-B. Blanchard[115], G. Blanchot[29], T. Blazek[144a], C. Blocker[22], J. Blocki[38], A. Blondel[49], W. Blum[81], U. Blumenschein[54], G.J. Bobbink[105], V.B. Bobrovnikov[107], S.S. Bocchetta[79], A. Bocci[44], C.R. Boddy[118], M. Boehler[41], J. Boek[174], N. Boelaert[35], S. Böser[77], J.A. Bogaerts[29], A. Bogdanchikov[107], A. Bogouch[90,*], C. Bohm[146a], V. Boisvert[76], T. Bold[163,g], V. Boldea[25a], N.M. Bolnet[136], M. Bona[75], V.G. Bondarenko[96], M. Boonekamp[136], G. Boorman[76], C.N. Booth[139], S. Bordoni[78], C. Borer[16], A. Borisov[128], G. Borissov[71], I. Borjanovic[12a], S. Borroni[132a,132b], K. Bos[105], D. Boscherini[19a], M. Bosman[11], H. Boterenbrood[105], D. Botterill[129], J. Bouchami[93], J. Boudreau[123], E.V. Bouhova-Thacker[71], C. Bourdarios[115], N. Bousson[83], A. Boveia[30], J. Boyd[29], I.R. Boyko[65], N.I. Bozhko[128], I. Bozovic-Jelisavcic[12b], J. Bracinik[17], A. Braem[29], P. Branchini[134a], G.W. Brandenburg[57], A. Brandt[7], G. Brandt[15], O. Brandt[54], U. Bratzler[156], B. Brau[84], J.E. Brau[114], H.M. Braun[174], B. Brelier[158], J. Bremer[29], R. Brenner[166], S. Bressler[152], D. Breton[115], D. Britton[53], F.M. Brochu[27], I. Brock[20], R. Brock[88], T.J. Brodbeck[71], E. Brodet[153], F. Broggi[89a], C. Bromberg[88], G. Brooijmans[34], W.K. Brooks[31b], G. Brown[82], H. Brown[7], P.A. Bruckman de Renstrom[38], D. Bruncko[144b], R. Bruneliere[48], S. Brunet[61], A. Bruni[19a], G. Bruni[19a], M. Bruschi[19a], T. Buanes[13], F. Bucci[49], J. Buchanan[118], N.J. Buchanan[2], P. Buchholz[141], R.M. Buckingham[118], A.G. Buckley[45], S.I. Buda[25a], I.A. Budagov[65], B. Budick[108], V. Büscher[81], L. Bugge[117], D. Buira-Clark[118], O. Bulekov[96], M. Bunse[42], T. Buran[117], H. Burckhart[29], S. Burdin[73], T. Burgess[13], S. Burke[129], E. Busato[33], P. Bussey[53], C.P. Buszello[166], F. Butin[29], B. Butler[143], J.M. Butler[21], C.M. Buttar[53], J.M. Butterworth[77], W. Buttinger[27], T. Byatt[77], S. Cabrera Urbán[167], D. Caforio[19a,19b], O. Cakir[3a], P. Calafiura[14], G. Calderini[78], P. Calfayan[98], R. Calkins[106], L.P. Caloba[23a], R. Caloi[132a,132b], D. Calvet[33], S. Calvet[33], R. Camacho Toro[33], P. Camarri[133a,133b], M. Cambiaghi[119a,119b], D. Cameron[117], S. Campana[29], M. Campanelli[77], V. Canale[102a,102b], F. Canelli[30], A. Canepa[159a], J. Cantero[80], L. Capasso[102a,102b], M.D.M. Capeans Garrido[29], I. Caprini[25a], M. Caprini[25a], D. Capriotti[99], M. Capua[36a,36b], R. Caputo[148], C. Caramarcu[25a], R. Cardarelli[133a], T. Carli[29], G. Carlino[102a], L. Carminati[89a,89b], B. Caron[159a], S. Caron[48], G.D. Carrillo Montoya[172], A.A. Carter[75],

J.R. Carter[27], J. Carvalho[124a,h], D. Casadei[108], M.P. Casado[11], M. Cascella[122a,122b], C. Caso[50a,50b,*], A.M. Castaneda Hernandez[172], E. Castaneda-Miranda[172], V. Castillo Gimenez[167], N.F. Castro[124a], G. Cataldi[72a], F. Cataneo[29], A. Catinaccio[29], J.R. Catmore[71], A. Cattai[29], G. Cattani[133a,133b], S. Caughron[88], D. Cauz[164a,164c], P. Cavalleri[78], D. Cavalli[89a], M. Cavalli-Sforza[11], V. Cavasinni[122a,122b], F. Ceradini[134a,134b], A.S. Cerqueira[23a], A. Cerri[29], L. Cerrito[75], F. Cerutti[47], S.A. Cetin[18b], F. Cevenini[102a,102b], A. Chafaq[135a], D. Chakraborty[106], K. Chan[2], B. Chapleau[85], J.D. Chapman[27], J.W. Chapman[87], E. Chareyre[78], D.G. Charlton[17], V. Chavda[82], C.A. Chavez Barajas[29], S. Cheatham[85], S. Chekanov[5], S.V. Chekulaev[159a], G.A. Chelkov[65], M.A. Chelstowska[104], C. Chen[64], H. Chen[24], S. Chen[32c], T. Chen[32c], X. Chen[172], S. Cheng[32a], A. Cheplakov[65], V.F. Chepurnov[65], R. Cherkaoui El Moursli[135e], V. Chernyatin[24], E. Cheu[6], S.L. Cheung[158], L. Chevalier[136], G. Chiefari[102a,102b], L. Chikovani[51], J.T. Childers[58a], A. Chilingarov[71], G. Chiodini[72a], M.V. Chizhov[65], G. Choudalakis[30], S. Chouridou[137], I.A. Christidi[77], A. Christov[48], D. Chromek-Burckhart[29], M.L. Chu[151], J. Chudoba[125], G. Ciapetti[132a,132b], K. Ciba[37], A.K. Ciftci[3a], R. Ciftci[3a], D. Cinca[33], V. Cindro[74], M.D. Ciobotaru[163], C. Ciocca[19a,19b], A. Ciocio[14], M. Cirilli[87], M. Ciubancan[25a], A. Clark[49], P.J. Clark[45], W. Cleland[123], J.C. Clemens[83], B. Clement[55], C. Clement[146a,146b], R.W. Clifft[129], Y. Coadou[83], M. Cobal[164a,164c], A. Coccaro[50a,50b], J. Cochran[64], P. Coe[118], J.G. Cogan[143], J. Coggeshall[165], E. Cogneras[177], C.D. Cojocaru[28], J. Colas[4], A.P. Colijn[105], C. Collard[115], N.J. Collins[17], C. Collins-Tooth[53], J. Collot[55], G. Colon[84], P. Conde Muiño[124a], E. Coniavitis[118], M.C. Conidi[11], M. Consonni[104], V. Consorti[48], S. Constantinescu[25a], C. Conta[119a,119b], F. Conventi[102a,i], J. Cook[29], M. Cooke[14], B.D. Cooper[77], A.M. Cooper-Sarkar[118], N.J. Cooper-Smith[76], K. Copic[34], T. Cornelissen[50a,50b], M. Corradi[19a], F. Corriveau[85,j], A. Cortes-Gonzalez[165], G. Cortiana[99], G. Costa[89a], M.J. Costa[167], D. Costanzo[139], T. Costin[30], D. Côté[29], R. Coura Torres[23a], L. Courneyea[169], G. Cowan[76], C. Cowden[27], B.E. Cox[82], K. Cranmer[108], F. Crescioli[122a,122b], M. Cristinziani[20], G. Crosetti[36a,36b], R. Crupi[72a,72b], S. Crépé-Renaudin[55], C.-M. Cuciuc[25a], C. Cuenca Almenar[175], T. Cuhadar Donszelmann[139], M. Curatolo[47], C.J. Curtis[17], P. Cwetanski[61], H. Czirr[141], Z. Czyczula[117], S. D'Auria[53], M. D'Onofrio[73], A. D'Orazio[132a,132b], P.V.M. Da Silva[23a], C. Da Via[82], W. Dabrowski[37], T. Dai[87], C. Dallapiccola[84], M. Dam[35], M. Dameri[50a,50b], D.S. Damiani[137], H.O. Danielsson[29], D. Dannheim[99], V. Dao[49], G. Darbo[50a], G.L. Darlea[25b], C. Daum[105], J.P. Dauvergne [29], W. Davey[86], T. Davidek[126], N. Davidson[86], R. Davidson[71], E. Davies[118,c], M. Davies[93], A.R. Davison[77], Y. Davygora[58a], E. Dawe[142], I. Dawson[139], J.W. Dawson[5,*], R.K. Daya[39], K. De[7], R. de Asmundis[102a], S. De Castro[19a,19b], P.E. De Castro Faria Salgado[24], S. De Cecco[78], J. de Graat[98], N. De Groot[104], P. de Jong[105], C. De La Taille[115], H. De la Torre[80], B. De Lotto[164a,164c], L. De Mora[71], L. De Nooij[105], M. De Oliveira Branco[29], D. De Pedis[132a], A. De Salvo[132a], U. De Sanctis[164a,164c], A. De Santo[149], J.B. De Vivie De Regie[115], S. Dean[77], D.V. Dedovich[65], J. Degenhardt[120], M. Dehchar[118], C. Del Papa[164a,164c], J. Del Peso[80], T. Del Prete[122a,122b], M. Deliyergiyev[74], A. Dell'Acqua[29], L. Dell'Asta[89a,89b], M. Della Pietra[102a,i], D. della Volpe[102a,102b], M. Delmastro[29], P. Delpierre[83], N. Delruelle[29], P.A. Delsart[55], C. Deluca[148], S. Demers[175], M. Demichev[65], B. Demirkoz[11,k], J. Deng[163], S.P. Denisov[128], D. Derendarz[38], J.E. Derkaoui[135d], F. Derue[78], P. Dervan[73], K. Desch[20], E. Devetak[148], P.O. Deviveiros[158], A. Dewhurst[129], B. DeWilde[148], S. Dhaliwal[158], R. Dhullipudi[24,l], A. Di Ciaccio[133a,133b], L. Di Ciaccio[4], A. Di Girolamo[29], B. Di Girolamo[29], S. Di Luise[134a,134b], A. Di Mattia[88], B. Di Micco[29], R. Di Nardo[133a,133b], A. Di Simone[133a,133b], R. Di Sipio[19a,19b], M.A. Diaz[31a], F. Diblen[18c], E.B. Diehl[87], J. Dietrich[41], T.A. Dietzsch[58a], S. Diglio[115], K. Dindar Yagci[39], J. Dingfelder[20], C. Dionisi[132a,132b], P. Dita[25a], S. Dita[25a], F. Dittus[29], F. Djama[83], T. Djobava[51], M.A.B. do Vale[23a], A. Do Valle Wemans[124a], T.K.O. Doan[4], M. Dobbs[85], R. Dobinson [29,*], D. Dobos[42], E. Dobson[29], M. Dobson[163], J. Dodd[34], C. Doglioni[118], T. Doherty[53], Y. Doi[66,*], J. Dolejsi[126], I. Dolenc[74], Z. Dolezal[126], B.A. Dolgoshein[96,*], T. Dohmae[155], M. Donadelli[23d], M. Donega[120], J. Donini[55], J. Dopke[29], A. Doria[102a], A. Dos Anjos[172], M. Dosil[11], A. Dotti[122a,122b], M.T. Dova[70], J.D. Dowell[17], A.D. Doxiadis[105], A.T. Doyle[53], Z. Drasal[126], J. Drees[174], N. Dressnandt[120], H. Drevermann[29], C. Driouichi[35], M. Dris[9], J. Dubbert[99], T. Dubbs[137], S. Dube[14], E. Duchovni[171], G. Duckeck[98], A. Dudarev[29], F. Dudziak[64], M. Dührssen [29], I.P. Duerdoth[82], L. Duflot[115], M-A. Dufour[85], M. Dunford[29], H. Duran Yildiz[3b], R. Duxfield[139], M. Dwuznik[37], F. Dydak [29], D. Dzahini[55], M. Düren[52], W.L. Ebenstein[44], J. Ebke[98], S. Eckert[48], S. Eckweiler[81], K. Edmonds[81], C.A. Edwards[76], N.C. Edwards[53], W. Ehrenfeld[41], T. Ehrich[99], T. Eifert[29], G. Eigen[13], K. Einsweiler[14], E. Eisenhandler[75], T. Ekelof[166], M. El Kacimi[135c], M. Ellert[166], S. Elles[4], F. Ellinghaus[81], K. Ellis[75], N. Ellis[29], J. Elmsheuser[98], M. Elsing[29], D. Emeliyanov[129], R. Engelmann[148], A. Engl[98], B. Epp[62], A. Eppig[87], J. Erdmann[54], A. Ereditato[16], D. Eriksson[146a], J. Ernst[1], M. Ernst[24], J. Ernwein[136], D. Errede[165], S. Errede[165], E. Ertel[81], M. Escalier[115], C. Escobar[167], X. Espinal Curull[11], B. Esposito[47], F. Etienne[83], A.I. Etienvre[136], E. Etzion[153], D. Evangelakou[54], H. Evans[61], L. Fabbri[19a,19b], C. Fabre[29], R.M. Fakhrutdinov[128], S. Falciano[132a], Y. Fang[172], M. Fanti[89a,89b], A. Farbin[7], A. Farilla[134a], J. Farley[148], T. Farooque[158], S.M. Farrington[118], P. Farthouat[29], P. Fassnacht[29], D. Fassouliotis[8], B. Fatholahzadeh[158], A. Favareto[89a,89b], L. Fayard[115], S. Fazio[36a,36b], R. Febbraro[33], P. Federic[144a], O.L. Fedin[121], W. Fedorko[88], M. Fehling-Kaschek[48], L. Feligioni[83], D. Fellmann[5], C.U. Felzmann[86], C. Feng[32d], E.J. Feng[30], A.B. Fenyuk[128], J. Ferencei[144b], J. Ferland[93], W. Fernando[109], S. Ferrag[53], J. Ferrando[53], V. Ferrara[41], A. Ferrari[166], P. Ferrari[105], R. Ferrari[119a], A. Ferrer[167], M.L. Ferrer[47], D. Ferrere[49], C. Ferretti[87], A. Ferretto Parodi[50a,50b], M. Fiascaris[30], F. Fiedler[81], A. Filipčič[74], A. Filippas[9], F. Filthaut[104], M. Fincke-Keeler[169], M.C.N. Fiolhais[124a,h], L. Fiorini[167],

A. Firan[39], G. Fischer[41], P. Fischer [20], M.J. Fisher[109], S.M. Fisher[129], M. Flechl[48], I. Fleck[141], J. Fleckner[81], P. Fleischmann[173], S. Fleischmann[174], T. Flick[174], L.R. Flores Castillo[172], M.J. Flowerdew[99], M. Fokitis[9], T. Fonseca Martin[16], D.A. Forbush[138], A. Formica[136], A. Forti[82], D. Fortin[159a], J.M. Foster[82], D. Fournier[115], A. Foussat[29], A.J. Fowler[44], K. Fowler[137], H. Fox[71], P. Francavilla[122a,122b], S. Franchino[119a,119b], D. Francis[29], T. Frank[171], M. Franklin[57], S. Franz[29], M. Fraternali[119a,119b], S. Fratina[120], S.T. French[27], F. Friedrich [43], R. Froeschl[29], D. Froidevaux[29], J.A. Frost[27], C. Fukunaga[156], E. Fullana Torregrosa[29], J. Fuster[167], C. Gabaldon[29], O. Gabizon[171], T. Gadfort[24], S. Gadomski[49], G. Gagliardi[50a,50b], P. Gagnon[61], C. Galea[98], E.J. Gallas[118], M.V. Gallas[29], V. Gallo[16], B.J. Gallop[129], P. Gallus[125], E. Galyaev[40], K.K. Gan[109], Y.S. Gao[143,f], V.A. Gapienko[128], A. Gaponenko[14], F. Garberson[175], M. Garcia-Sciveres[14], C. García[167], J.E. García Navarro[49], R.W. Gardner[30], N. Garelli[29], H. Garitaonandia[105], V. Garonne[29], J. Garvey[17], C. Gatti[47], G. Gaudio[119a], O. Gaumer[49], B. Gaur[141], L. Gauthier[136], I.L. Gavrilenko[94], C. Gay[168], G. Gaycken[20], J-C. Gayde[29], E.N. Gazis[9], P. Ge[32d], C.N.P. Gee[129], D.A.A. Geerts[105], Ch. Geich-Gimbel[20], K. Gellerstedt[146a,146b], C. Gemme[50a], A. Gemmell[53], M.H. Genest[98], S. Gentile[132a,132b], M. George[54], S. George[76], P. Gerlach[174], A. Gershon[153], C. Geweniger[58a], H. Ghazlane[135b], P. Ghez[4], N. Ghodbane[33], B. Giacobbe[19a], S. Giagu[132a,132b], V. Giakoumopoulou[8], V. Giangiobbe[122a,122b], F. Gianotti[29], B. Gibbard[24], A. Gibson[158], S.M. Gibson[29], L.M. Gilbert[118], M. Gilchriese[14], V. Gilewsky[91], D. Gillberg[28], A.R. Gillman[129], D.M. Gingrich[2,e], J. Ginzburg[153], N. Giokaris[8], R. Giordano[102a,102b], F.M. Giorgi[15], P. Giovannini[99], P.F. Giraud[136], D. Giugni[89a], M. Giunta[132a,132b], P. Giusti[19a], B.K. Gjelsten[117], L.K. Gladilin[97], C. Glasman[80], J. Glatzer[48], A. Glazov[41], K.W. Glitza[174], G.L. Glonti[65], J. Godfrey[142], J. Godlewski[29], M. Goebel[41], T. Göpfert[43], C. Goeringer[81], C. Gössling[42], T. Göttfert[99], S. Goldfarb[87], D. Goldin[39], T. Golling[175], S.N. Golovnia[128], A. Gomes[124a,b], L.S. Gomez Fajardo[41], R. Gonçalo[76], J. Goncalves Pinto Firmino Da Costa[41], L. Gonella[20], A. Gonidec[29], S. Gonzalez[172], S. González de la Hoz[167], M.L. Gonzalez Silva[26], S. Gonzalez-Sevilla[49], J.J. Goodson[148], L. Goossens[29], P.A. Gorbounov[95], H.A. Gordon[24], I. Gorelov[103], G. Gorfine[174], B. Gorini[29], E. Gorini[72a,72b], A. Gorišek[74], E. Gornicki[38], S.A. Gorokhov[128], V.N. Goryachev[128], B. Gosdzik[41], M. Gosselink[105], M.I. Gostkin[65], I. Gough Eschrich[163], M. Gouighri[135a], D. Goujdami[135c], M.P. Goulette[49], A.G. Goussiou[138], C. Goy[4], I. Grabowska-Bold[163,g], V. Grabski[176], P. Grafström[29], C. Grah[174], K-J. Grahn[41], F. Grancagnolo[72a], S. Grancagnolo[15], V. Grassi[148], V. Gratchev[121], N. Grau[34], H.M. Gray[29], J.A. Gray[148], E. Graziani[134a], O.G. Grebenyuk[121], D. Greenfield[129], T. Greenshaw[73], Z.D. Greenwood[24,l], K. Gregersen[35], I.M. Gregor[41], P. Grenier[143], J. Griffiths[138], N. Grigalashvili[65], A.A. Grillo[137], S. Grinstein[11], Y.V. Grishkevich[97], J.-F. Grivaz[115], J. Grognuz[29], M. Groh[99], E. Gross[171], J. Grosse-Knetter[54], J. Groth-Jensen[171], K. Grybel[141], V.J. Guarino[5], D. Guest[175], C. Guicheney[33], A. Guida[72a,72b], T. Guillemin[4], S. Guindon[54], H. Guler[85,m], J. Gunther[125], B. Guo[158], J. Guo[34], A. Gupta[30], Y. Gusakov[65], V.N. Gushchin[128], A. Gutierrez[93], P. Gutierrez[111], N. Guttman[153], O. Gutzwiller[172], C. Guyot[136], C. Gwenlan[118], C.B. Gwilliam[73], A. Haas[143], S. Haas[29], C. Haber[14], R. Hackenburg[24], H.K. Hadavand[39], D.R. Hadley[17], P. Haefner[99], F. Hahn[29], S. Haider[29], Z. Hajduk[38], H. Hakobyan[176], J. Haller[54], K. Hamacher[174], P. Hamal[113], A. Hamilton[49], S. Hamilton[161], H. Han[32a], L. Han[32b], K. Hanagaki[116], M. Hance[120], C. Handel[81], P. Hanke[58a], J.R. Hansen[35], J.B. Hansen[35], J.D. Hansen[35], P.H. Hansen[35], P. Hansson[143], K. Hara[160], G.A. Hare[137], T. Harenberg[174], S. Harkusha[90], D. Harper[87], R.D. Harrington[21], O.M. Harris[138], K. Harrison[17], J. Hartert[48], F. Hartjes[105], T. Haruyama[66], A. Harvey[56], S. Hasegawa[101], Y. Hasegawa[140], S. Hassani[136], M. Hatch[29], D. Hauff[99], S. Haug[16], M. Hauschild[29], R. Hauser[88], M. Havranek[20], B.M. Hawes[118], C.M. Hawkes[17], R.J. Hawkings[29], D. Hawkins[163], T. Hayakawa[67], D Hayden[76], H.S. Hayward[73], S.J. Haywood[129], E. Hazen[21], M. He[32d], S.J. Head[17], V. Hedberg[79], L. Heelan[7], S. Heim[88], B. Heinemann[14], S. Heisterkamp[35], L. Helary[4], M. Heller[115], S. Hellman[146a,146b], D. Hellmich[20], C. Helsens[11], R.C.W. Henderson[71], M. Henke[58a], A. Henrichs[54], A.M. Henriques Correia[29], S. Henrot-Versille[115], F. Henry-Couannier[83], C. Hensel[54], T. Henß[174], C.M. Hernandez[7], Y. Hernández Jiménez[167], R. Herrberg[15], A.D. Hershenhorn[152], G. Herten[48], R. Hertenberger[98], L. Hervas[29], N.P. Hessey[105], A. Hidvegi[146a], E. Higón-Rodriguez[167], D. Hill[5,*], J.C. Hill[27], N. Hill[5], K.H. Hiller[41], S. Hillert[20], S.J. Hillier[17], I. Hinchliffe[14], E. Hines[120], M. Hirose[116], F. Hirsch[42], D. Hirschbuehl[174], J. Hobbs[148], N. Hod[153], M.C. Hodgkinson[139], P. Hodgson[139], A. Hoecker[29], M.R. Hoeferkamp[103], J. Hoffman[39], D. Hoffmann[83], M. Hohlfeld[81], M. Holder[141], S.O. Holmgren[146a], T. Holy[127], J.L. Holzbauer[88], Y. Homma[67], T.M. Hong[120], L. Hooft van Huysduynen[108], T. Horazdovsky[127], C. Horn[143], S. Horner[48], K. Horton[118], J-Y. Hostachy[55], S. Hou[151], M.A. Houlden[73], A. Hoummada[135a], J. Howarth[82], D.F. Howell[118], I. Hristova [15], J. Hrivnac[115], I. Hruska[125], T. Hryn'ova[4], P.J. Hsu[175], S.-C. Hsu[14], G.S. Huang[111], Z. Hubacek[127], F. Hubaut[83], F. Huegging[20], T.B. Huffman[118], E.W. Hughes[34], G. Hughes[71], R.E. Hughes-Jones[82], M. Huhtinen[29], P. Hurst[57], M. Hurwitz[14], U. Husemann[41], N. Huseynov[65,n], J. Huston[88], J. Huth[57], G. Iacobucci[49], G. Iakovidis[9], M. Ibbotson[82], I. Ibragimov[141], R. Ichimiya[67], L. Iconomidou-Fayard[115], J. Idarraga[115], M. Idzik[37], P. Iengo[102a,102b], O. Igonkina[105], Y. Ikegami[66], M. Ikeno[66], Y. Ilchenko[39], D. Iliadis[154], D. Imbault[78], M. Imhaeuser[174], M. Imori[155], T. Ince[20], J. Inigo-Golfin[29], P. Ioannou[8], M. Iodice[134a], G. Ionescu[4], A. Irles Quiles[167], K. Ishii[66], A. Ishikawa[67], M. Ishino[68], R. Ishmukhametov[39], C. Issever[118], S. Istin[18a], A.V. Ivashin[128], W. Iwanski[38], H. Iwasaki[66], J.M. Izen[40], V. Izzo[102a], B. Jackson[120], J.N. Jackson[73], P. Jackson[143], M.R. Jaekel[29], V. Jain[61], K. Jakobs[48], S. Jakobsen[35], J. Jakubek[127], D.K. Jana[111], E. Jankowski[158], E. Jansen[77], A. Jantsch[99], M. Janus[20], G. Jarlskog[79], L. Jeanty[57], K. Jelen[37], I. Jen-La Plante[30], P. Jenni[29], A. Jeremie[4], P. Ježˇ[35], S. Jézéquel[4], M.K. Jha[19a], H. Ji[172],

W. Ji[81], J. Jia[148], Y. Jiang[32b], M. Jimenez Belenguer[41], G. Jin[32b], S. Jin[32a], O. Jinnouchi[157], M.D. Joergensen[35], D. Joffe[39], L.G. Johansen[13], M. Johansen[146a,146b], K.E. Johansson[146a], P. Johansson[139], S. Johnert[41], K.A. Johns[6], K. Jon-And[146a,146b], G. Jones[82], R.W.L. Jones[71], T.W. Jones[77], T.J. Jones[73], O. Jonsson[29], C. Joram[29], P.M. Jorge[124a,b], J. Joseph[14], T. Jovin[12b], X. Ju[130], V. Juranek[125], P. Jussel[62], A. Juste Rozas[11], V.V. Kabachenko[128], S. Kabana[16], M. Kaci[167], A. Kaczmarska[38], P. Kadlecik[35], M. Kado[115], H. Kagan[109], M. Kagan[57], S. Kaiser[99], E. Kajomovitz[152], S. Kalinin[174], L.V. Kalinovskaya[65], S. Kama[39], N. Kanaya[155], M. Kaneda[29], T. Kanno[157], V.A. Kantserov[96], J. Kanzaki[66], B. Kaplan[175], A. Kapliy[30], J. Kaplon[29], D. Kar[43], M. Karagoz[118], M. Karnevskiy[41], K. Karr[5], V. Kartvelishvili[71], A.N. Karyukhin[128], L. Kashif[172], A. Kasmi[39], R.D. Kass[109], A. Kastanas[13], M. Kataoka[4], Y. Kataoka[155], E. Katsoufis[9], J. Katzy[41], V. Kaushik[6], K. Kawagoe[67], T. Kawamoto[155], G. Kawamura[81], M.S. Kayl[105], V.A. Kazanin[107], M.Y. Kazarinov[65], J.R. Keates[82], R. Keeler[169], R. Kehoe[39], M. Keil[54], G.D. Kekelidze[65], M. Kelly[82], J. Kennedy[98], C.J. Kenney[143], M. Kenyon[53], O. Kepka[125], N. Kerschen[29], B.P. Kerševan[74], S. Kersten[174], K. Kessoku[155], C. Ketterer[48], J. Keung[158], M. Khakzad[28], F. Khalil-zada[10], H. Khandanyan[165], A. Khanov[112], D. Kharchenko[65], A. Khodinov[96], A.G. Kholodenko[128], A. Khomich[58a], T.J. Khoo[27], G. Khoriauli[20], A. Khoroshilov[174], N. Khovanskiy[65], V. Khovanskiy[95], E. Khramov[65], J. Khubua[51], H. Kim[7], M.S. Kim[2], P.C. Kim[143], S.H. Kim[160], N. Kimura[170], O. Kind[15], B.T. King[73], M. King[67], R.S.B. King[118], J. Kirk[129], G.P. Kirsch[118], L.E. Kirsch[22], A.E. Kiryunin[99], T. Kishimoto[67], D. Kisielewska[37], T. Kittelmann[123], A.M. Kiver[128], H. Kiyamura[67], E. Kladiva[144b], J. Klaiber-Lodewigs[42], M. Klein[73], U. Klein[73], K. Kleinknecht[81], M. Klemetti[85], A. Klier[171], A. Klimentov[24], R. Klingenberg[42], E.B. Klinkby[35], T. Klioutchnikova[29], P.F. Klok[104], S. Klous[105], E.-E. Kluge[58a], T. Kluge[73], P. Kluit[105], S. Kluth[99], N.S. Knecht[158], E. Kneringer[62], J. Knobloch[29], E.B.F.G. Knoops[83], A. Knue[54], B.R. Ko[44], T. Kobayashi[155], M. Kobel[43], M. Kocian[143], A. Kocnar[113], P. Kodys[126], K. Köneke[29], A.C. König[104], S. Koenig[81], L. Köpke[81], F. Koetsveld[104], P. Koevesarki[20], T. Koffas[29], E. Koffeman[105], F. Kohn[54], Z. Kohout[127], T. Kohriki[66], T. Koi[143], T. Kokott[20], G.M. Kolachev[107], H. Kolanoski[15], V. Kolesnikov[65], I. Koletsou[89a], J. Koll[88], D. Kollar[29], M. Kollefrath[48], S.D. Kolya[82], A.A. Komar[94], J.R. Komaragiri[142], Y. Komori[155], T. Kondo[66], T. Kono[41,o], A.I. Kononov[48], R. Konoplich[108,p], N. Konstantinidis[77], A. Kootz[174], S. Koperny[37], S.V. Kopikov[128], K. Korcyl[38], K. Kordas[154], V. Koreshev[128], A. Korn[14], A. Korol[107], I. Korolkov[11], E.V. Korolkova[139], V.A. Korotkov[128], O. Kortner[99], S. Kortner[99], V.V. Kostyukhin[20], M.J. Kotamäki[29], S. Kotov[99], V.M. Kotov[65], A. Kotwal[44], C. Kourkoumelis[8], V. Kouskoura[154], A. Koutsman[105], R. Kowalewski[169], T.Z. Kowalski[37], W. Kozanecki[136], A.S. Kozhin[128], V. Kral[127], V.A. Kramarenko[97], G. Kramberger[74], M.W. Krasny[78], A. Krasznahorkay[108], J. Kraus[88], A. Kreisel[153], F. Krejci[127], J. Kretzschmar[73], N. Krieger[54], P. Krieger[158], K. Kroeninger[54], H. Kroha[99], J. Kroll[120], J. Kroseberg[20], J. Krstic[12a], U. Kruchonak[65], H. Krüger[20], T. Kruker[16], Z.V. Krumshteyn[65], A. Kruth[20], T. Kubota[86], S. Kuehn[48], A. Kugel[58c], T. Kuhl[41], D. Kuhn[62], V. Kukhtin[65], Y. Kulchitsky[90], S. Kuleshov[31b], C. Kummer[98], M. Kuna[78], N. Kundu[118], J. Kunkle[120], A. Kupco[125], H. Kurashige[67], M. Kurata[160], Y.A. Kurochkin[90], V. Kus[125], W. Kuykendall[138], M. Kuze[157], P. Kuzhir[91], J. Kvita[29], R. Kwee[15], A. La Rosa[172], L. La Rotonda[36a,36b], L. Labarga[80], J. Labbe[4], S. Lablak[135a], C. Lacasta[167], F. Lacava[132a,132b], H. Lacker[15], D. Lacour[78], V.R. Lacuesta[167], E. Ladygin[65], R. Lafaye[4], B. Laforge[78], T. Lagouri[80], S. Lai[48], E. Laisne[55], M. Lamanna[29], C.L. Lampen[6], W. Lampl[6], E. Lancon[136], U. Landgraf[48], M.P.J. Landon[75], H. Landsman[152], J.L. Lane[82], C. Lange[41], A.J. Lankford[163], F. Lanni[24], K. Lantzsch[29], S. Laplace[78], C. Lapoire[20], J.F. Laporte[136], T. Lari[89a], A.V. Larionov [128], A. Larner[118], C. Lasseur[29], M. Lassnig[29], P. Laurelli[47], A. Lavorato[118], W. Lavrijsen[14], P. Laycock[73], A.B. Lazarev[65], O. Le Dortz[78], E. Le Guirriec[83], C. Le Maner[158], E. Le Menedeu[136], C. Lebel[93], T. LeCompte[5], F. Ledroit-Guillon[55], H. Lee[105], J.S.H. Lee[150], S.C. Lee[151], L. Lee[175], M. Lefebvre[169], M. Legendre[136], A. Leger[49], B.C. LeGeyt[120], F. Legger[98], C. Leggett[14], M. Lehmacher[20], G. Lehmann Miotto[29], X. Lei[6], M.A.L. Leite[23d], R. Leitner[126], D. Lellouch[171], M. Leltchouk[34], B. Lemmer[54], V. Lendermann[58a], K.J.C. Leney[145b], T. Lenz[105], G. Lenzen[174], B. Lenzi[29], K. Leonhardt[43], S. Leontsinis[9], C. Leroy[93], J-R. Lessard[169], J. Lesser[146a], C.G. Lester[27], A. Leung Fook Cheong[172], J. Levêque[4], D. Levin[87], L.J. Levinson[171], M.S. Levitski[128], M. Lewandowska[21], A. Lewis[118], G.H. Lewis[108], A.M. Leyko[20], M. Leyton[15], B. Li[83], H. Li[172], S. Li[32b,d], X. Li[87], Z. Liang[39], Z. Liang[118,q], B. Liberti[133a], P. Lichard[29], M. Lichtnecker[98], K. Lie[165], W. Liebig[13], R. Lifshitz[152], J.N. Lilley[17], C. Limbach[20], A. Limosani[86], M. Limper[63], S.C. Lin[151,r], F. Linde[105], J.T. Linnemann[88], E. Lipeles[120], L. Lipinsky[125], A. Lipniacka[13], T.M. Liss[165], D. Lissauer[24], A. Lister[49], A.M. Litke[137], C. Liu[28], D. Liu[151,s], H. Liu[87], J.B. Liu[87], M. Liu[32b], S. Liu[2], Y. Liu[32b], M. Livan[119a,119b], S.S.A. Livermore[118], A. Lleres[55], J. Llorente Merino[80], S.L. Lloyd[75], E. Lobodzinska[41], P. Loch[6], W.S. Lockman[137], S. Lockwitz[175], T. Loddenkoetter[20], F.K. Loebinger[82], A. Loginov[175], C.W. Loh[168], T. Lohse[15], K. Lohwasser[48], M. Lokajicek[125], J. Loken [118], V.P. Lombardo[4], R.E. Long[71], L. Lopes[124a,b], D. Lopez Mateos[57], M. Losada[162], P. Loscutoff[14], F. Lo Sterzo[132a,132b], M.J. Losty[159a], X. Lou[40], A. Lounis[115], K.F. Loureiro[162], J. Love[21], P.A. Love[71], A.J. Lowe[143,f], F. Lu[32a], H.J. Lubatti[138], C. Luci[132a,132b], A. Lucotte[55], A. Ludwig[43], D. Ludwig[41], I. Ludwig[48], J. Ludwig[48], F. Luehring[61], G. Luijckx[105], D. Lumb[48], L. Luminari[132a], E. Lund[117], B. Lund-Jensen[147], B. Lundberg[79], J. Lundberg[146a,146b], J. Lundquist[35], M. Lungwitz[81], A. Lupi[122a,122b], G. Lutz[99], D. Lynn[24], J. Lys[14], E. Lytken[79], H. Ma[24], L.L. Ma[172], J.A. Macana Goia[93], G. Maccarrone[47], A. Macchiolo[99], B. Maček[74], J. Machado Miguens[124a], R. Mackeprang[35], R.J. Madaras[14], W.F. Mader[43], R. Maenner[58c], T. Maeno[24],

P. Mättig[174], S. Mättig[41], P.J. Magalhaes Martins[124a,h], L. Magnoni[29], E. Magradze[54], Y. Mahalalel[153], K. Mahboubi[48], G. Mahout[17], C. Maiani[132a,132b], C. Maidantchik[23a], A. Maio[124a,b], S. Majewski[24], Y. Makida[66], N. Makovec[115], P. Mal[6], Pa. Malecki[38], P. Malecki[38], V.P. Maleev[121], F. Malek[55], U. Mallik[63], D. Malon[5], S. Maltezos[9], V. Malyshev[107], S. Malyukov[29], R. Mameghani[98], J. Mamuzic[12b], A. Manabe[66], L. Mandelli[89a], I. Mandić[74], R. Mandrysch[15], J. Maneira[124a], P.S. Mangeard[88], I.D. Manjavidze[65], A. Mann[54], P.M. Manning[137], A. Manousakis-Katsikakis[8], B. Mansoulie[136], A. Manz[99], A. Mapelli[29], L. Mapelli[29], L. March [80], J.F. Marchand[29], F. Marchese[133a,133b], G. Marchiori[78], M. Marcisovsky[125], A. Marin[21,*], C.P. Marino[61], F. Marroquim[23a], R. Marshall[82], Z. Marshall[29], F.K. Martens[158], S. Marti-Garcia[167], A.J. Martin[175], B. Martin[29], B. Martin[88], F.F. Martin[120], J.P. Martin[93], Ph. Martin[55], T.A. Martin[17], B. Martin dit Latour[49], S. Martin–Haugh[149], M. Martinez[11], V. Martinez Outschoorn[57], A.C. Martyniuk[82], M. Marx[82], F. Marzano[132a], A. Marzin[111], L. Masetti[81], T. Mashimo[155], R. Mashinistov[94], J. Masik[82], A.L. Maslennikov[107], I. Massa[19a,19b], G. Massaro[105], N. Massol[4], P. Mastrandrea[132a,132b], A. Mastroberardino[36a,36b], T. Masubuchi[155], M. Mathes[20], P. Matricon[115], H. Matsumoto[155], H. Matsunaga[155], T. Matsushita[67], C. Mattravers[118,c], J.M. Maugain[29], J. Maurer[83], S.J. Maxfield[73], D.A. Maximov[107], E.N. May[5], A. Mayne[139], R. Mazini[151], M. Mazur[20], M. Mazzanti[89a], E. Mazzoni[122a,122b], S.P. Mc Kee[87], A. McCarn[165], R.L. McCarthy[148], T.G. McCarthy[28], N.A. McCubbin[129], K.W. McFarlane[56], J.A. Mcfayden[139], H. McGlone[53], G. Mchedlidze[51], R.A. McLaren[29], T. Mclaughlan[17], S.J. McMahon[129], R.A. McPherson[169,j], A. Meade[84], J. Mechnich[105], M. Mechtel[174], M. Medinnis[41], R. Meera-Lebbai[111], T. Meguro[116], R. Mehdiyev[93], S. Mehlhase[35], A. Mehta[73], K. Meier[58a], J. Meinhardt[48], B. Meirose[79], C. Melachrinos[30], B.R. Mellado Garcia[172], L. Mendoza Navas[162], Z. Meng[151,s], A. Mengarelli[19a,19b], S. Menke[99], C. Menot[29], E. Meoni[11], K.M. Mercurio[57], P. Mermod[118], L. Merola[102a,102b], C. Meroni[89a], F.S. Merritt[30], A. Messina[29], J. Metcalfe[103], A.S. Mete[64], S. Meuser[20], C. Meyer[81], J-P. Meyer[136], J. Meyer[173], J. Meyer[54], T.C. Meyer[29], W.T. Meyer[64], J. Miao[32d], S. Michal[29], L. Micu[25a], R.P. Middleton[129], P. Miele[29], S. Migas[73], L. Mijović[41], G. Mikenberg[171], M. Mikestikova[125], M. Mikuž[74], D.W. Miller[143], R.J. Miller[88], W.J. Mills[168], C. Mills[57], A. Milov[171], D.A. Milstead[146a,146b], D. Milstein[171], A.A. Minaenko[128], M. Miñano[167], I.A. Minashvili[65], A.I. Mincer[108], B. Mindur[37], M. Mineev[65], Y. Ming[130], L.M. Mir[11], G. Mirabelli[132a], L. Miralles Verge[11], A. Misiejuk[76], J. Mitrevski[137], G.Y. Mitrofanov[128], V.A. Mitsou[167], S. Mitsui[66], P.S. Miyagawa[139], K. Miyazaki[67], J.U. Mjörnmark[79], T. Moa[146a,146b], P. Mockett[138], S. Moed[57], V. Moeller[27], K. Mönig[41], N. Möser[20], S. Mohapatra[148], W. Mohr[48], S. Mohrdieck-Möck[99], A.M. Moisseev[128,*], R. Moles-Valls[167], J. Molina-Perez[29], J. Monk[77], E. Monnier[83], S. Montesano[89a,89b], F. Monticelli[70], S. Monzani[19a,19b], R.W. Moore[2], G.F. Moorhead[86], C. Mora Herrera[49], A. Moraes[53], N. Morange[136], J. Morel[54], G. Morello[36a,36b], D. Moreno[81], M. Moreno Llácer[167], P. Morettini[50a], M. Morii[57], J. Morin[75], Y. Morita[66], A.K. Morley[29], G. Mornacchi[29], S.V. Morozov[96], J.D. Morris[75], L. Morvaj[101], H.G. Moser[99], M. Mosidze[51], J. Moss[109], R. Mount[143], E. Mountricha[136], S.V. Mouraviev[94], E.J.W. Moyse[84], M. Mudrinic[12b], F. Mueller[58a], J. Mueller[123], K. Mueller[20], T.A. Müller[98], D. Muenstermann[29], A. Muir[168], Y. Munwes[153], W.J. Murray[129], I. Mussche[105], E. Musto[102a,102b], A.G. Myagkov[128], M. Myska[125], J. Nadal[11], K. Nagai[160], K. Nagano[66], Y. Nagasaka[60], A.M. Nairz[29], Y. Nakahama[29], K. Nakamura[155], I. Nakano[110], G. Nanava[20], A. Napier[161], M. Nash[77,c], N.R. Nation[21], T. Nattermann[20], T. Naumann[41], G. Navarro[162], H.A. Neal[87], E. Nebot[80], P.Yu. Nechaeva[94], A. Negri[119a,119b], G. Negri[29], S. Nektarijevic[49], S. Nelson[143], T.K. Nelson[143], S. Nemecek[125], P. Nemethy[108], A.A. Nepomuceno[23a], M. Nessi[29,t], S.Y. Nesterov[121], M.S. Neubauer[165], A. Neusiedl[81], R.M. Neves[108], P. Nevski[24], P.R. Newman[17], V. Nguyen Thi Hong[136], R.B. Nickerson[118], R. Nicolaidou[136], L. Nicolas[139], B. Nicquevert[29], F. Niedercorn[115], J. Nielsen[137], T. Niinikoski[29], N. Nikiforou[34], A. Nikiforov[15], V. Nikolaenko[128], K. Nikolaev[65], I. Nikolic-Audit[78], K. Nikolics[49], K. Nikolopoulos[24], H. Nilsen[48], P. Nilsson[7], Y. Ninomiya [155], A. Nisati[132a], T. Nishiyama[67], R. Nisius[99], L. Nodulman[5], M. Nomachi[116], I. Nomidis[154], M. Nordberg[29], B. Nordkvist[146a,146b], P.R. Norton[129], J. Novakova[126], M. Nozaki[66], M. Nožička[41], L. Nozka[113], I.M. Nugent[159a], A.-E. Nuncio-Quiroz[20], G. Nunes Hanninger[86], T. Nunnemann[98], E. Nurse[77], T. Nyman[29], B.J. O'Brien[45], S.W. O'Neale[17,*], D.C. O'Neil[142], V. O'Shea[53], F.G. Oakham[28,e], H. Oberlack[99], J. Ocariz[78], A. Ochi[67], S. Oda[155], S. Odaka[66], J. Odier[83], H. Ogren[61], A. Oh[82], S.H. Oh[44], C.C. Ohm[146a,146b], T. Ohshima[101], H. Ohshita[140], T.K. Ohska[66], T. Ohsugi[59], S. Okada[67], H. Okawa[163], Y. Okumura[101], T. Okuyama[155], M. Olcese[50a], A.G. Olchevski[65], M. Oliveira[124a,h], D. Oliveira Damazio[24], E. Oliver Garcia[167], D. Olivito[120], A. Olszewski[38], J. Olszowska[38], C. Omachi[67], A. Onofre[124a,u], P.U.E. Onyisi[30], C.J. Oram[159a], M.J. Oreglia[30], Y. Oren[153], D. Orestano[134a,134b], I. Orlov[107], C. Oropeza Barrera[53], R.S. Orr[158], B. Osculati[50a,50b], R. Ospanov[120], C. Osuna[11], G. Otero y Garzon[26], J.P Ottersbach[105], M. Ouchrif[135d], F. Ould-Saada[117], A. Ouraou[136], Q. Ouyang[32a], M. Owen[82], S. Owen[139], V.E. Ozcan[18a], N. Ozturk[7], A. Pacheco Pages[11], C. Padilla Aranda[11], S. Pagan Griso[14], E. Paganis[139], F. Paige[24], K. Pajchel[117], G. Palacino[159b], C.P. Paleari[6], S. Palestini[29], D. Pallin[33], A. Palma[124a,b], J.D. Palmer[17], Y.B. Pan[172], E. Panagiotopoulou[9], B. Panes[31a], N. Panikashvili[87], S. Panitkin[24], D. Pantea[25a], M. Panuskova[125], V. Paolone[123], A. Papadelis[146a], Th.D. Papadopoulou[9], A. Paramonov[5], W. Park[24,v], M.A. Parker[27], F. Parodi[50a,50b], J.A. Parsons[34], U. Parzefall[48], E. Pasqualucci[132a], A. Passeri[134a], F. Pastore[134a,134b], Fr. Pastore[29], G. Pásztor [49,w], S. Pataraia[172], N. Patel[150], J.R. Pater[82], S. Patricelli[102a,102b], T. Pauly[29], M. Pecsy[144a], M.I. Pedraza Morales[172], S.V. Peleganchuk[107], H. Peng[32b], R. Pengo[29], A. Penson[34], J. Penwell[61], M. Perantoni[23a], K. Perez[34,x],

T. Perez Cavalcanti[41], E. Perez Codina[11], M.T. Pérez García-Estañ[167], V. Perez Reale[34], L. Perini[89a,89b], H. Pernegger[29], R. Perrino[72a], P. Perrodo[4], S. Persembe[3a], V.D. Peshekhonov[65], B.A. Petersen[29], J. Petersen[29], T.C. Petersen[35], E. Petit[83], A. Petridis[154], C. Petridou[154], E. Petrolo[132a], F. Petrucci[134a,134b], D. Petschull[41], M. Petteni[142], R. Pezoa[31b], A. Phan[86], A.W. Phillips[27], P.W. Phillips[129], G. Piacquadio[29], E. Piccaro[75], M. Piccinini[19a,19b], A. Pickford[53], S.M. Piec[41], R. Piegaia[26], J.E. Pilcher[30], A.D. Pilkington[82], J. Pina[124a,b], M. Pinamonti[164a,164c], A. Pinder[118], J.L. Pinfold[2], J. Ping[32c], B. Pinto[124a,b], O. Pirotte[29], C. Pizio[89a,89b], R. Placakyte[41], M. Plamondon[169], W.G. Plano[82], M.-A. Pleier[24], A.V. Pleskach[128], A. Poblaguev[24], S. Poddar[58a], F. Podlyski[33], L. Poggioli[115], T. Poghosyan[20], M. Pohl[49], F. Polci[55], G. Polesello[119a], A. Policicchio[138], A. Polini[19a], J. Poll[75], V. Polychronakos[24], D.M. Pomarede[136], D. Pomeroy[22], K. Pommès[29], L. Pontecorvo[132a], B.G. Pope[88], G.A. Popeneciu[25a], D.S. Popovic[12a], A. Poppleton[29], X. Portell Bueso[29], R. Porter[163], C. Posch[21], G.E. Pospelov[99], S. Pospisil[127], I.N. Potrap[99], C.J. Potter[149], C.T. Potter[114], G. Poulard[29], J. Poveda[172], R. Prabhu[77], P. Pralavorio[83], S. Prasad[57], R. Pravahan[7], S. Prell[64], K. Pretzl[16], L. Pribyl[29], D. Price[61], L.E. Price[5], M.J. Price[29], P.M. Prichard[73], D. Prieur[123], M. Primavera[72a], K. Prokofiev[108], F. Prokoshin[31b], S. Protopopescu[24], J. Proudfoot[5], X. Prudent[43], H. Przysiezniak[4], S. Psoroulas[20], E. Ptacek[114], E. Pueschel[84], J. Purdham[87], M. Purohit[24,v], P. Puzo[115], Y. Pylypchenko[117], J. Qian[87], Z. Qian[83], Z. Qin[41], A. Quadt[54], D.R. Quarrie[14], W.B. Quayle[172], F. Quinonez[31a], M. Raas[104], V. Radescu[58b], B. Radics[20], T. Rador[18a], F. Ragusa[89a,89b], G. Rahal[177], A.M. Rahimi[109], D. Rahm[24], S. Rajagopalan[24], M. Rammensee[48], M. Rammes[141], M. Ramstedt[146a,146b], A.S. Randle-Conde[39], K. Randrianarivony[28], P.N. Ratoff[71], F. Rauscher[98], E. Rauter[99], M. Raymond[29], A.L. Read[117], D.M. Rebuzzi[119a,119b], A. Redelbach[173], G. Redlinger[24], R. Reece[120], K. Reeves[40], A. Reichold[105], E. Reinherz-Aronis[153], A. Reinsch[114], I. Reisinger[42], D. Reljic[12a], C. Rembser[29], Z.L. Ren[151], A. Renaud[115], P. Renkel[39], M. Rescigno[132a], S. Resconi[89a], B. Resende[136], P. Reznicek[98], R. Rezvani[158], A. Richards[77], R. Richter[99], E. Richter-Was[38,y], M. Ridel[78], S. Rieke[81], M. Rijpstra[105], M. Rijssenbeek[148], A. Rimoldi[119a,119b], L. Rinaldi[19a], R.R. Rios[39], I. Riu[11], G. Rivoltella[89a,89b], F. Rizatdinova[112], E. Rizvi[75], S.H. Robertson[85,j], A. Robichaud-Veronneau[49], D. Robinson[27], J.E.M. Robinson[77], M. Robinson[114], A. Robson[53], J.G. Rocha de Lima[106], C. Roda[122a,122b], D. Roda Dos Santos[29], S. Rodier[80], D. Rodriguez[162], A. Roe[54], S. Roe[29], O. Røhne[117], V. Rojo[1], S. Rolli[161], A. Romaniouk[96], V.M. Romanov[65], G. Romeo[26], L. Roos[78], E. Ros[167], S. Rosati[132a,132b], K. Rosbach[49], A. Rose[149], M. Rose[76], G.A. Rosenbaum[158], E.I. Rosenberg[64], P.L. Rosendahl[13], O. Rosenthal[141], L. Rosselet[49], V. Rossetti[11], E. Rossi[102a,102b], L.P. Rossi[50a], L. Rossi[89a,89b], M. Rotaru[25a], I. Roth[171], J. Rothberg[138], D. Rousseau[115], C.R. Royon[136], A. Rozanov[83], Y. Rozen[152], X. Ruan[115], I. Rubinskiy[41], B. Ruckert[98], N. Ruckstuhl[105], V.I. Rud[97], C. Rudolph[43], G. Rudolph[62], F. Rühr[6], F. Ruggieri[134a,134b], A. Ruiz-Martinez[64], E. Rulikowska-Zarebska[37], V. Rumiantsev[91,*], L. Rumyantsev[65], K. Runge[48], O. Runolfsson[20], Z. Rurikova[48], N.A. Rusakovich[65], D.R. Rust[61], J.P. Rutherfoord[6], C. Ruwiedel[14], P. Ruzicka[125], Y.F. Ryabov[121], V. Ryadovikov[128], P. Ryan[88], M. Rybar[126], G. Rybkin[115], N.C. Ryder[118], S. Rzaeva[10], A.F. Saavedra[150], I. Sadeh[153], H.F-W. Sadrozinski[137], R. Sadykov[65], F. Safai Tehrani[132a,132b], H. Sakamoto[155], G. Salamanna[75], A. Salamon[133a], M. Saleem[111], D. Salihagic[99], A. Salnikov[143], J. Salt[167], B.M. Salvachua Ferrando[5], D. Salvatore[36a,36b], F. Salvatore[149], A. Salvucci[104], A. Salzburger[29], D. Sampsonidis[154], B.H. Samset[117], A. Sanchez[102a,102b], H. Sandaker[13], H.G. Sander[81], M.P. Sanders[98], M. Sandhoff[174], T. Sandoval[27], C. Sandoval [162], R. Sandstroem[99], S. Sandvoss[174], D.P.C. Sankey[129], A. Sansoni[47], C. Santamarina Rios[85], C. Santoni[33], R. Santonico[133a,133b], H. Santos[124a], J.G. Saraiva[124a,b], T. Sarangi[172], E. Sarkisyan-Grinbaum[7], F. Sarri[122a,122b], G. Sartisohn[174], O. Sasaki[66], T. Sasaki[66], N. Sasao[68], I. Satsounkevitch[90], G. Sauvage[4], E. Sauvan[4], J.B. Sauvan[115], P. Savard[158,e], V. Savinov[123], D.O. Savu[29], P. Savva [9], L. Sawyer[24,l], D.H. Saxon[53], L.P. Says[33], C. Sbarra[19a,19b], A. Sbrizzi[19a,19b], O. Scallon[93], D.A. Scannicchio[163], J. Schaarschmidt[115], P. Schacht[99], U. Schäfer[81], S. Schaepe[20], S. Schaetzel[58b], A.C. Schaffer[115], D. Schaile[98], R.D. Schamberger[148], A.G. Schamov[107], V. Scharf[58a], V.A. Schegelsky[121], D. Scheirich[87], M. Schernau[163], M.I. Scherzer[14], C. Schiavi[50a,50b], J. Schieck[98], M. Schioppa[36a,36b], S. Schlenker[29], J.L. Schlereth[5], E. Schmidt[48], K. Schmieden[20], C. Schmitt[81], S. Schmitt[58b], M. Schmitz[20], A. Schöning[58b], M. Schott[29], D. Schouten[142], J. Schovancova[125], M. Schram[85], C. Schroeder[81], N. Schroer[58c], S. Schuh[29], G. Schuler[29], J. Schultes[174], H.-C. Schultz-Coulon[58a], H. Schulz[15], J.W. Schumacher[20], M. Schumacher[48], B.A. Schumm[137], Ph. Schune[136], C. Schwanenberger[82], A. Schwartzman[143], Ph. Schwemling[78], R. Schwienhorst[88], R. Schwierz[43], J. Schwindling[136], T. Schwindt[20], W.G. Scott[129], J. Searcy[114], E. Sedykh[121], E. Segura[11], S.C. Seidel[103], A. Seiden[137], F. Seifert[43], J.M. Seixas[23a], G. Sekhniaidze[102a], D.M. Seliverstov[121], B. Sellden[146a], G. Sellers[73], M. Seman[144b], N. Semprini-Cesari[19a,19b], C. Serfon[98], L. Serin[115], R. Seuster[99], H. Severini[111], M.E. Sevior[86], A. Sfyrla[29], E. Shabalina[54], M. Shamim[114], L.Y. Shan[32a], J.T. Shank[21], Q.T. Shao[86], M. Shapiro[14], P.B. Shatalov[95], L. Shaver[6], K. Shaw[164a,164c], D. Sherman[175], P. Sherwood[77], A. Shibata[108], H. Shichi[101], S. Shimizu[29], M. Shimojima[100], T. Shin[56], A. Shmeleva[94], M.J. Shochet[30], D. Short[118], M.A. Shupe[6], P. Sicho[125], A. Sidoti[132a,132b], A. Siebel[174], F. Siegert[48], J. Siegrist[14], Dj. Sijacki[12a], O. Silbert[171], J. Silva[124a,b], Y. Silver[153], D. Silverstein[143], S.B. Silverstein[146a], V. Simak[127], O. Simard[136], Lj. Simic[12a], S. Simion[115], B. Simmons[77], M. Simonyan[35], P. Sinervo[158], N.B. Sinev[114], V. Sipica[141], G. Siragusa[173], A. Sircar[24], A.N. Sisakyan[65], S.Yu. Sivoklokov[97], J. Sjölin[146a,146b], T.B. Sjursen[13], L.A. Skinnari[14], K. Skovpen[107], P. Skubic[111], N. Skvorodnev[22], M. Slater[17], T. Slavicek[127], K. Sliwa[161], T.J. Sloan[71], J. Sloper[29], V. Smakhtin[171],

S.Yu. Smirnov[96], L.N. Smirnova[97], O. Smirnova[79], B.C. Smith[57], D. Smith[143], K.M. Smith[53], M. Smizanska[71], K. Smolek[127], A.A. Snesarev[94], S.W. Snow[82], J. Snow[111], J. Snuverink[105], S. Snyder[24], M. Soares[124a], R. Sobie[169,j], J. Sodomka[127], A. Soffer[153], C.A. Solans[167], M. Solar[127], J. Solc[127], E. Soldatov[96], U. Soldevila[167], E. Solfaroli Camillocci[132a,132b], A.A. Solodkov[128], O.V. Solovyanov[128], J. Sondericker[24], N. Soni[2], V. Sopko[127], B. Sopko[127], M. Sorbi[89a,89b], M. Sosebee[7], A. Soukharev[107], S. Spagnolo[72a,72b], F. Spanò[76], R. Spighi[19a], G. Spigo[29], F. Spila[132a,132b], E. Spiriti[134a], R. Spiwoks[29], M. Spousta[126], T. Spreitzer[158], B. Spurlock[7], R.D. St. Denis[53], T. Stahl[141], J. Stahlman[120], R. Stamen[58a], E. Stanecka[29], R.W. Stanek[5], C. Stanescu[134a], S. Stapnes[117], E.A. Starchenko[128], J. Stark[55], P. Staroba[125], P. Starovoitov[91], A. Staude[98], P. Stavina[144a], G. Stavropoulos[14], G. Steele[53], P. Steinbach[43], P. Steinberg[24], I. Stekl[127], B. Stelzer[142], H.J. Stelzer[88], O. Stelzer-Chilton[159a], H. Stenzel[52], K. Stevenson[75], G.A. Stewart[29], J.A. Stillings[20], T. Stockmanns[20], M.C. Stockton[29], K. Stoerig[48], G. Stoicea[25a], S. Stonjek[99], P. Strachota[126], A.R. Stradling[7], A. Straessner[43], J. Strandberg[147], S. Strandberg[146a,146b], A. Strandlie[117], M. Strang[109], E. Strauss[143], M. Strauss[111], P. Strizenec[144b], R. Ströhmer[173], D.M. Strom[114], J.A. Strong[76,*], R. Stroynowski[39], J. Strube[129], B. Stugu[13], I. Stumer[24,*], J. Stupak[148], P. Sturm[174], D.A. Soh[151,q], D. Su[143], HS. Subramania[2], A. Succurro[11], Y. Sugaya[116], T. Sugimoto[101], C. Suhr[106], K. Suita[67], M. Suk[126], V.V. Sulin[94], S. Sultansoy[3d], T. Sumida[29], X. Sun[55], J.E. Sundermann[48], K. Suruliz[139], S. Sushkov[11], G. Susinno[36a,36b], M.R. Sutton[149], Y. Suzuki[66], Y. Suzuki[67], M. Svatos[125], Yu.M. Sviridov[128], S. Swedish[168], I. Sykora[144a], T. Sykora[126], B. Szeless[29], J. Sánchez[167], D. Ta[105], K. Tackmann[41], A. Taffard[163], R. Tafirout[159a], A. Taga[117], N. Taiblum[153], Y. Takahashi[101], H. Takai[24], R. Takashima[69], H. Takeda[67], T. Takeshita[140], M. Talby[83], A. Talyshev[107], M.C. Tamsett[24], J. Tanaka[155], R. Tanaka[115], S. Tanaka[131], S. Tanaka[66], Y. Tanaka[100], K. Tani[67], N. Tannoury[83], G.P. Tappern[29], S. Tapprogge[81], D. Tardif[158], S. Tarem[152], F. Tarrade[28], G.F. Tartarelli[89a], P. Tas[126], M. Tasevsky[125], E. Tassi[36a,36b], M. Tatarkhanov[14], C. Taylor[77], F.E. Taylor[92], G.N. Taylor[86], W. Taylor[159b], M. Teinturier[115], M. Teixeira Dias Castanheira[75], P. Teixeira-Dias[76], K.K. Temming[48], H. Ten Kate[29], P.K. Teng[151], S. Terada[66], K. Terashi[155], J. Terron[80], M. Terwort[41,o], M. Testa[47], R.J. Teuscher[158,j], J. Thadome[174], J. Therhaag[20], T. Theveneaux-Pelzer[78], M. Thioye[175], S. Thoma[48], J.P. Thomas[17], E.N. Thompson[84], P.D. Thompson[17], P.D. Thompson[158], A.S. Thompson[53], E. Thomson[120], M. Thomson[27], R.P. Thun[87], F. Tian[34], T. Tic[125], V.O. Tikhomirov[94], Y.A. Tikhonov[107], C.J.W.P. Timmermans[104], P. Tipton[175], F.J. Tique Aires Viegas[29], S. Tisserant[83], J. Tobias[48], B. Toczek[37], T. Todorov[4], S. Todorova-Nova[161], B. Toggerson[163], J. Tojo[66], S. Tokár[144a], K. Tokunaga[67], K. Tokushuku[66], K. Tollefson[88], M. Tomoto[101], L. Tompkins[14], K. Toms[103], G. Tong[32a], A. Tonoyan[13], C. Topfel[16], N.D. Topilin[65], I. Torchiani[29], E. Torrence[114], H. Torres[78], E. Torró Pastor[167], J. Toth[83,w], F. Touchard[83], D.R. Tovey[139], D. Traynor[75], T. Trefzger[173], L. Tremblet[29], A. Tricoli[29], I.M. Trigger[159a], S. Trincaz-Duvoid[78], T.N. Trinh[78], M.F. Tripiana[70], W. Trischuk[158], A. Trivedi[24,v], B. Trocmé[55], C. Troncon[89a], M. Trottier-McDonald[142], A. Trzupek[38], C. Tsarouchas[29], J.C-L. Tseng[118], M. Tsiakiris[105], P.V. Tsiareshka[90], D. Tsionou[4], G. Tsipolitis[9], V. Tsiskaridze[48], E.G. Tskhadadze[51], I.I. Tsukerman[95], V. Tsulaia[14], J.-W. Tsung[20], S. Tsuno[66], D. Tsybychev[148], A. Tua[139], J.M. Tuggle[30], M. Turala[38], D. Turecek[127], I. Turk Cakir[3e], E. Turlay[105], R. Turra[89a,89b], P.M. Tuts[34], A. Tykhonov[74], M. Tylmad[146a,146b], M. Tyndel[129], H. Tyrvainen[29], G. Tzanakos[8], K. Uchida[20], I. Ueda[155], R. Ueno[28], M. Ugland[13], M. Uhlenbrock[20], M. Uhrmacher[54], F. Ukegawa[160], G. Unal[29], D.G. Underwood[5], A. Undrus[24], G. Unel[163], Y. Unno[66], D. Urbaniec[34], E. Urkovsky[153], P. Urrejola[31a], G. Usai[7], M. Uslenghi[119a,119b], L. Vacavant[83], V. Vacek[127], B. Vachon[85], S. Vahsen[14], J. Valenta[125], P. Valente[132a], S. Valentinetti[19a,19b], S. Valkar[126], E. Valladolid Gallego[167], S. Vallecorsa[152], J.A. Valls Ferrer[167], H. van der Graaf[105], E. van der Kraaij[105], R. Van Der Leeuw[105], E. van der Poel[105], D. van der Ster[29], B. Van Eijk[105], N. van Eldik[84], P. van Gemmeren[5], Z. van Kesteren[105], I. van Vulpen[105], W. Vandelli[29], G. Vandoni[29], A. Vaniachine[5], P. Vankov[41], F. Vannucci[78], F. Varela Rodriguez[29], R. Vari[132a], D. Varouchas[14], A. Vartapetian[7], K.E. Varvell[150], V.I. Vassilakopoulos[56], F. Vazeille[33], G. Vegni[89a,89b], J.J. Veillet[115], C. Vellidis[8], F. Veloso[124a], R. Veness[29], S. Veneziano[132a], A. Ventura[72a,72b], D. Ventura[138], M. Venturi[48], N. Venturi[16], V. Vercesi[119a], M. Verducci[138], W. Verkerke[105], J.C. Vermeulen[105], A. Vest[43], M.C. Vetterli[142,e], I. Vichou[165], T. Vickey[145b,z], G.H.A. Viehhauser[118], S. Viel[168], M. Villa[19a,19b], M. Villaplana Perez[167], E. Vilucchi[47], M.G. Vincter[28], E. Vinek[29], V.B. Vinogradov[65], M. Virchaux[136,*], J. Virzi[14], O. Vitells[171], M. Viti[41], I. Vivarelli[48], F. Vives Vaque[11], S. Vlachos[9], M. Vlasak[127], N. Vlasov[20], A. Vogel[20], P. Vokac[127], G. Volpi[47], M. Volpi[86], G. Volpini[89a], H. von der Schmitt[99], J. von Loeben[99], H. von Radziewski[48], E. von Toerne[20], V. Vorobel[126], A.P. Vorobiev[128], V. Vorwerk[11], M. Vos[167], R. Voss[29], T.T. Voss[174], J.H. Vossebeld[73], N. Vranjes[12a], M. Vranjes Milosavljevic[105], V. Vrba[125], M. Vreeswijk[105], T. Vu Anh[81], R. Vuillermet[29], I. Vukotic[115], W. Wagner[174], P. Wagner[120], H. Wahlen[174], J. Wakabayashi[101], J. Walbersloh[42], S. Walch[87], J. Walder[71], R. Walker[98], W. Walkowiak[141], R. Wall[175], P. Waller[73], C. Wang[44], H. Wang[172], H. Wang[32b,aa], J. Wang[151], J. Wang[32d], J.C. Wang[138], R. Wang[103], S.M. Wang[151], A. Warburton[85], C.P. Ward[27], M. Warsinsky[48], P.M. Watkins[17], A.T. Watson[17], M.F. Watson[17], G. Watts[138], S. Watts[82], A.T. Waugh[150], B.M. Waugh[77], J. Weber[42], M. Weber[129], M.S. Weber[16], P. Weber[54], A.R. Weidberg[118], P. Weigell[99], J. Weingarten[54], C. Weiser[48], H. Wellenstein[22], P.S. Wells[29], M. Wen[47], T. Wenaus[24], S. Wendler[123], Z. Weng[151,q], T. Wengler[29], S. Wenig[29], N. Wermes[20], M. Werner[48], P. Werner[29], M. Werth[163], M. Wessels[58a], C. Weydert[55], K. Whalen[28], S.J. Wheeler-Ellis[163], S.P. Whitaker[21], A. White[7],

M.J. White[86], S.R. Whitehead[118], D. Whiteson[163], D. Whittington[61], F. Wicek[115], D. Wicke[174], F.J. Wickens[129], W. Wiedenmann[172], M. Wielers[129], P. Wienemann[20], C. Wiglesworth[75], L.A.M. Wiik[48], P.A. Wijeratne[77], A. Wildauer[167], M.A. Wildt[41,o], I. Wilhelm[126], H.G. Wilkens[29], J.Z. Will[98], E. Williams[34], H.H. Williams[120], W. Willis[34], S. Willocq[84], J.A. Wilson[17], M.G. Wilson[143], A. Wilson[87], I. Wingerter-Seez[4], S. Winkelmann[48], F. Winklmeier[29], M. Wittgen[143], M.W. Wolter[38], H. Wolters[124a,h], W.C. Wong[40], G. Wooden[118], B.K. Wosiek[38], J. Wotschack[29], M.J. Woudstra[84], K. Wraight[53], C. Wright[53], B. Wrona[73], S.L. Wu[172], X. Wu[49], Y. Wu[32b,ab], E. Wulf[34], R. Wunstorf[42], B.M. Wynne[45], L. Xaplanteris[9], S. Xella[35], S. Xie[48], Y. Xie[32a], C. Xu[32b,ac], D. Xu[139], G. Xu[32a], B. Yabsley[150], S. Yacoob[145b], M. Yamada[66], H. Yamaguchi[155], A. Yamamoto[66], K. Yamamoto[64], S. Yamamoto[155], T. Yamamura[155], T. Yamanaka[155], J. Yamaoka[44], T. Yamazaki[155], Y. Yamazaki[67], Z. Yan[21], H. Yang[87], U.K. Yang[82], Y. Yang[61], Y. Yang[32a], Z. Yang[146a,146b], S. Yanush[91], W-M. Yao[14], Y. Yao[14], Y. Yasu[66], G.V. Ybeles Smit[130], J. Ye[39], S. Ye[24], M. Yilmaz[3c], R. Yoosoofmiya[123], K. Yorita[170], R. Yoshida[5], C. Young[143], S. Youssef[21], D. Yu[24], J. Yu[7], J. Yu[32c,ac], L. Yuan[32a,ad], A. Yurkewicz[148], V.G. Zaets [128], R. Zaidan[63], A.M. Zaitsev[128], Z. Zajacova[29], Yo.K. Zalite [121], L. Zanello[132a,132b], P. Zarzhitsky[39], A. Zaytsev[107], C. Zeitnitz[174], M. Zeller[175], M. Zeman[125], A. Zemla[38], C. Zendler[20], O. Zenin[128], T. Ženiš[144a], Z. Zenonos[122a,122b], S. Zenz[14], D. Zerwas[115], G. Zevi della Porta[57], Z. Zhan[32d], D. Zhang[32b,aa], H. Zhang[88], J. Zhang[5], X. Zhang[32d], Z. Zhang[115], L. Zhao[108], T. Zhao[138], Z. Zhao[32b], A. Zhemchugov[65], S. Zheng[32a], J. Zhong[151,ae], B. Zhou[87], N. Zhou[163], Y. Zhou[151], C.G. Zhu[32d], H. Zhu[41], J. Zhu[87], Y. Zhu[172], X. Zhuang[98], V. Zhuravlov[99], D. Zieminska[61], R. Zimmermann[20], S. Zimmermann[20], S. Zimmermann[48], M. Ziolkowski[141], R. Zitoun[4], L. Živković[34], V.V. Zmouchko[128,*], G. Zobernig[172], A. Zoccoli[19a,19b], Y. Zolnierowski[4], A. Zsenei[29], M. zur Nedden[15], V. Zutshi[106], L. Zwalinski[29].

[1] University at Albany, Albany NY, United States of America
[2] Department of Physics, University of Alberta, Edmonton AB, Canada
[3] [(a)]Department of Physics, Ankara University, Ankara; [(b)]Department of Physics, Dumlupinar University, Kutahya; [(c)]Department of Physics, Gazi University, Ankara; [(d)]Division of Physics, TOBB University of Economics and Technology, Ankara; [(e)]Turkish Atomic Energy Authority, Ankara, Turkey
[4] LAPP, CNRS/IN2P3 and Université de Savoie, Annecy-le-Vieux, France
[5] High Energy Physics Division, Argonne National Laboratory, Argonne IL, United States of America
[6] Department of Physics, University of Arizona, Tucson AZ, United States of America
[7] Department of Physics, The University of Texas at Arlington, Arlington TX, United States of America
[8] Physics Department, University of Athens, Athens, Greece
[9] Physics Department, National Technical University of Athens, Zografou, Greece
[10] Institute of Physics, Azerbaijan Academy of Sciences, Baku, Azerbaijan
[11] Institut de Física d'Altes Energies and Departament de Física de la Universitat Autònoma de Barcelona and ICREA, Barcelona, Spain
[12] [(a)]Institute of Physics, University of Belgrade, Belgrade; [(b)]Vinca Institute of Nuclear Sciences, Belgrade, Serbia
[13] Department for Physics and Technology, University of Bergen, Bergen, Norway
[14] Physics Division, Lawrence Berkeley National Laboratory and University of California, Berkeley CA, United States of America
[15] Department of Physics, Humboldt University, Berlin, Germany
[16] Albert Einstein Center for Fundamental Physics and Laboratory for High Energy Physics, University of Bern, Bern, Switzerland
[17] School of Physics and Astronomy, University of Birmingham, Birmingham, United Kingdom
[18] [(a)]Department of Physics, Bogazici University, Istanbul; [(b)]Division of Physics, Dogus University, Istanbul; [(c)]Department of Physics Engineering, Gaziantep University, Gaziantep; [(d)]Department of Physics, Istanbul Technical University, Istanbul, Turkey
[19] [(a)]INFN Sezione di Bologna; [(b)]Dipartimento di Fisica, Università di Bologna, Bologna, Italy
[20] Physikalisches Institut, University of Bonn, Bonn, Germany
[21] Department of Physics, Boston University, Boston MA, United States of America
[22] Department of Physics, Brandeis University, Waltham MA, United States of America
[23] [(a)]Universidade Federal do Rio De Janeiro COPPE/EE/IF, Rio de Janeiro; [(b)]Federal University of Juiz de Fora (UFJF), Juiz de Fora; [(c)]Federal University of Sao Joao del Rei (UFSJ), Sao Joao del Rei; [(d)]Instituto de Fisica, Universidade de Sao Paulo, Sao Paulo, Brazil
[24] Physics Department, Brookhaven National Laboratory, Upton NY, United States of America
[25] [(a)]National Institute of Physics and Nuclear Engineering, Bucharest; [(b)]University Politehnica Bucharest, Bucharest; [(c)]West University in Timisoara, Timisoara, Romania
[26] Departamento de Física, Universidad de Buenos Aires, Buenos Aires, Argentina
[27] Cavendish Laboratory, University of Cambridge, Cambridge, United Kingdom
[28] Department of Physics, Carleton University, Ottawa ON, Canada
[29] CERN, Geneva, Switzerland

[30] Enrico Fermi Institute, University of Chicago, Chicago IL, United States of America
[31] [(a)]Departamento de Fisica, Pontificia Universidad Católica de Chile, Santiago; [(b)]Departamento de Física, Universidad Técnica Federico Santa María, Valparaíso, Chile
[32] [(a)]Institute of High Energy Physics, Chinese Academy of Sciences, Beijing; [(b)]Department of Modern Physics, University of Science and Technology of China, Anhui; [(c)]Department of Physics, Nanjing University, Jiangsu; [(d)]High Energy Physics Group, Shandong University, Shandong, China
[33] Laboratoire de Physique Corpusculaire, Clermont Université and Université Blaise Pascal and CNRS/IN2P3, Aubiere Cedex, France
[34] Nevis Laboratory, Columbia University, Irvington NY, United States of America
[35] Niels Bohr Institute, University of Copenhagen, Kobenhavn, Denmark
[36] [(a)]INFN Gruppo Collegato di Cosenza; [(b)]Dipartimento di Fisica, Università della Calabria, Arcavata di Rende, Italy
[37] Faculty of Physics and Applied Computer Science, AGH-University of Science and Technology, Krakow, Poland
[38] The Henryk Niewodniczanski Institute of Nuclear Physics, Polish Academy of Sciences, Krakow, Poland
[39] Physics Department, Southern Methodist University, Dallas TX, United States of America
[40] Physics Department, University of Texas at Dallas, Richardson TX, United States of America
[41] DESY, Hamburg and Zeuthen, Germany
[42] Institut für Experimentelle Physik IV, Technische Universität Dortmund, Dortmund, Germany
[43] Institut für Kern- und Teilchenphysik, Technical University Dresden, Dresden, Germany
[44] Department of Physics, Duke University, Durham NC, United States of America
[45] SUPA - School of Physics and Astronomy, University of Edinburgh, Edinburgh, United Kingdom
[46] Fachhochschule Wiener Neustadt, Johannes Gutenbergstrasse 3, 2700 Wiener Neustadt, Austria
[47] INFN Laboratori Nazionali di Frascati, Frascati, Italy
[48] Fakultät für Mathematik und Physik, Albert-Ludwigs-Universität, Freiburg i.Br., Germany
[49] Section de Physique, Université de Genève, Geneva, Switzerland
[50] [(a)]INFN Sezione di Genova; [(b)]Dipartimento di Fisica, Università di Genova, Genova, Italy
[51] Institute of Physics and HEP Institute, Georgian Academy of Sciences and Tbilisi State University, Tbilisi, Georgia
[52] II Physikalisches Institut, Justus-Liebig-Universität Giessen, Giessen, Germany
[53] SUPA - School of Physics and Astronomy, University of Glasgow, Glasgow, United Kingdom
[54] II Physikalisches Institut, Georg-August-Universität, Göttingen, Germany
[55] Laboratoire de Physique Subatomique et de Cosmologie, Université Joseph Fourier and CNRS/IN2P3 and Institut National Polytechnique de Grenoble, Grenoble, France
[56] Department of Physics, Hampton University, Hampton VA, United States of America
[57] Laboratory for Particle Physics and Cosmology, Harvard University, Cambridge MA, United States of America
[58] [(a)]Kirchhoff-Institut für Physik, Ruprecht-Karls-Universität Heidelberg, Heidelberg; [(b)]Physikalisches Institut, Ruprecht-Karls-Universität Heidelberg, Heidelberg; [(c)]ZITI Institut für technische Informatik, Ruprecht-Karls-Universität Heidelberg, Mannheim, Germany
[59] Faculty of Science, Hiroshima University, Hiroshima, Japan
[60] Faculty of Applied Information Science, Hiroshima Institute of Technology, Hiroshima, Japan
[61] Department of Physics, Indiana University, Bloomington IN, United States of America
[62] Institut für Astro- und Teilchenphysik, Leopold-Franzens-Universität, Innsbruck, Austria
[63] University of Iowa, Iowa City IA, United States of America
[64] Department of Physics and Astronomy, Iowa State University, Ames IA, United States of America
[65] Joint Institute for Nuclear Research, JINR Dubna, Dubna, Russia
[66] KEK, High Energy Accelerator Research Organization, Tsukuba, Japan
[67] Graduate School of Science, Kobe University, Kobe, Japan
[68] Faculty of Science, Kyoto University, Kyoto, Japan
[69] Kyoto University of Education, Kyoto, Japan
[70] Instituto de Física La Plata, Universidad Nacional de La Plata and CONICET, La Plata, Argentina
[71] Physics Department, Lancaster University, Lancaster, United Kingdom
[72] [(a)]INFN Sezione di Lecce; [(b)]Dipartimento di Fisica, Università del Salento, Lecce, Italy
[73] Oliver Lodge Laboratory, University of Liverpool, Liverpool, United Kingdom
[74] Department of Physics, Jožef Stefan Institute and University of Ljubljana, Ljubljana, Slovenia
[75] Department of Physics, Queen Mary University of London, London, United Kingdom
[76] Department of Physics, Royal Holloway University of London, Surrey, United Kingdom
[77] Department of Physics and Astronomy, University College London, London, United Kingdom
[78] Laboratoire de Physique Nucléaire et de Hautes Energies, UPMC and Université Paris-Diderot and CNRS/IN2P3, Paris, France

[79] Fysiska institutionen, Lunds universitet, Lund, Sweden
[80] Departamento de Fisica Teorica C-15, Universidad Autonoma de Madrid, Madrid, Spain
[81] Institut für Physik, Universität Mainz, Mainz, Germany
[82] School of Physics and Astronomy, University of Manchester, Manchester, United Kingdom
[83] CPPM, Aix-Marseille Université and CNRS/IN2P3, Marseille, France
[84] Department of Physics, University of Massachusetts, Amherst MA, United States of America
[85] Department of Physics, McGill University, Montreal QC, Canada
[86] School of Physics, University of Melbourne, Victoria, Australia
[87] Department of Physics, The University of Michigan, Ann Arbor MI, United States of America
[88] Department of Physics and Astronomy, Michigan State University, East Lansing MI, United States of America
[89] [(a)]INFN Sezione di Milano; [(b)]Dipartimento di Fisica, Università di Milano, Milano, Italy
[90] B.I. Stepanov Institute of Physics, National Academy of Sciences of Belarus, Minsk, Republic of Belarus
[91] National Scientific and Educational Centre for Particle and High Energy Physics, Minsk, Republic of Belarus
[92] Department of Physics, Massachusetts Institute of Technology, Cambridge MA, United States of America
[93] Group of Particle Physics, University of Montreal, Montreal QC, Canada
[94] P.N. Lebedev Institute of Physics, Academy of Sciences, Moscow, Russia
[95] Institute for Theoretical and Experimental Physics (ITEP), Moscow, Russia
[96] Moscow Engineering and Physics Institute (MEPhI), Moscow, Russia
[97] Skobeltsyn Institute of Nuclear Physics, Lomonosov Moscow State University, Moscow, Russia
[98] Fakultät für Physik, Ludwig-Maximilians-Universität München, München, Germany
[99] Max-Planck-Institut für Physik (Werner-Heisenberg-Institut), München, Germany
[100] Nagasaki Institute of Applied Science, Nagasaki, Japan
[101] Graduate School of Science, Nagoya University, Nagoya, Japan
[102] [(a)]INFN Sezione di Napoli; [(b)]Dipartimento di Scienze Fisiche, Università di Napoli, Napoli, Italy
[103] Department of Physics and Astronomy, University of New Mexico, Albuquerque NM, United States of America
[104] Institute for Mathematics, Astrophysics and Particle Physics, Radboud University Nijmegen/Nikhef, Nijmegen, Netherlands
[105] Nikhef National Institute for Subatomic Physics and University of Amsterdam, Amsterdam, Netherlands
[106] Department of Physics, Northern Illinois University, DeKalb IL, United States of America
[107] Budker Institute of Nuclear Physics (BINP), Novosibirsk, Russia
[108] Department of Physics, New York University, New York NY, United States of America
[109] Ohio State University, Columbus OH, United States of America
[110] Faculty of Science, Okayama University, Okayama, Japan
[111] Homer L. Dodge Department of Physics and Astronomy, University of Oklahoma, Norman OK, United States of America
[112] Department of Physics, Oklahoma State University, Stillwater OK, United States of America
[113] Palacký University, RCPTM, Olomouc, Czech Republic
[114] Center for High Energy Physics, University of Oregon, Eugene OR, United States of America
[115] LAL, Univ. Paris-Sud and CNRS/IN2P3, Orsay, France
[116] Graduate School of Science, Osaka University, Osaka, Japan
[117] Department of Physics, University of Oslo, Oslo, Norway
[118] Department of Physics, Oxford University, Oxford, United Kingdom
[119] [(a)]INFN Sezione di Pavia; [(b)]Dipartimento di Fisica Nucleare e Teorica, Università di Pavia, Pavia, Italy
[120] Department of Physics, University of Pennsylvania, Philadelphia PA, United States of America
[121] Petersburg Nuclear Physics Institute, Gatchina, Russia
[122] [(a)]INFN Sezione di Pisa; [(b)]Dipartimento di Fisica E. Fermi, Università di Pisa, Pisa, Italy
[123] Department of Physics and Astronomy, University of Pittsburgh, Pittsburgh PA, United States of America
[124] [(a)]Laboratorio de Instrumentacao e Fisica Experimental de Particulas - LIP, Lisboa, Portugal; [(b)]Departamento de Fisica Teorica y del Cosmos and CAFPE, Universidad de Granada, Granada, Spain
[125] Institute of Physics, Academy of Sciences of the Czech Republic, Praha, Czech Republic
[126] Faculty of Mathematics and Physics, Charles University in Prague, Praha, Czech Republic
[127] Czech Technical University in Prague, Praha, Czech Republic
[128] State Research Center Institute for High Energy Physics, Protvino, Russia
[129] Particle Physics Department, Rutherford Appleton Laboratory, Didcot, United Kingdom
[130] Physics Department, University of Regina, Regina SK, Canada
[131] Ritsumeikan University, Kusatsu, Shiga, Japan
[132] [(a)]INFN Sezione di Roma I; [(b)]Dipartimento di Fisica, Università La Sapienza, Roma, Italy
[133] [(a)]INFN Sezione di Roma Tor Vergata; [(b)]Dipartimento di Fisica, Università di Roma Tor Vergata, Roma, Italy
[134] [(a)]INFN Sezione di Roma Tre; [(b)]Dipartimento di Fisica, Università Roma Tre, Roma, Italy

[135] [(a)]Faculté des Sciences Ain Chock, Réseau Universitaire de Physique des Hautes Energies - Université Hassan II, Casablanca; [(b)]Centre National de l'Energie des Sciences Techniques Nucleaires, Rabat; [(c)]Université Cadi Ayyad, Faculté des sciences Semlalia Département de Physique, B.P. 2390 Marrakech 40000; [(d)]Faculté des Sciences, Université Mohamed Premier and LPTPM, Oujda; [(e)]Faculté des Sciences, Université Mohammed V, Rabat, Morocco
[136] DSM/IRFU (Institut de Recherches sur les Lois Fondamentales de l'Univers), CEA Saclay (Commissariat a l'Energie Atomique), Gif-sur-Yvette, France
[137] Santa Cruz Institute for Particle Physics, University of California Santa Cruz, Santa Cruz CA, United States of America
[138] Department of Physics, University of Washington, Seattle WA, United States of America
[139] Department of Physics and Astronomy, University of Sheffield, Sheffield, United Kingdom
[140] Department of Physics, Shinshu University, Nagano, Japan
[141] Fachbereich Physik, Universität Siegen, Siegen, Germany
[142] Department of Physics, Simon Fraser University, Burnaby BC, Canada
[143] SLAC National Accelerator Laboratory, Stanford CA, United States of America
[144] [(a)]Faculty of Mathematics, Physics & Informatics, Comenius University, Bratislava; [(b)]Department of Subnuclear Physics, Institute of Experimental Physics of the Slovak Academy of Sciences, Kosice, Slovak Republic
[145] [(a)]Department of Physics, University of Johannesburg, Johannesburg; [(b)]School of Physics, University of the Witwatersrand, Johannesburg, South Africa
[146] [(a)]Department of Physics, Stockholm University; [(b)]The Oskar Klein Centre, Stockholm, Sweden
[147] Physics Department, Royal Institute of Technology, Stockholm, Sweden
[148] Department of Physics and Astronomy, Stony Brook University, Stony Brook NY, United States of America
[149] Department of Physics and Astronomy, University of Sussex, Brighton, United Kingdom
[150] School of Physics, University of Sydney, Sydney, Australia
[151] Institute of Physics, Academia Sinica, Taipei, Taiwan
[152] Department of Physics, Technion: Israel Inst. of Technology, Haifa, Israel
[153] Raymond and Beverly Sackler School of Physics and Astronomy, Tel Aviv University, Tel Aviv, Israel
[154] Department of Physics, Aristotle University of Thessaloniki, Thessaloniki, Greece
[155] International Center for Elementary Particle Physics and Department of Physics, The University of Tokyo, Tokyo, Japan
[156] Graduate School of Science and Technology, Tokyo Metropolitan University, Tokyo, Japan
[157] Department of Physics, Tokyo Institute of Technology, Tokyo, Japan
[158] Department of Physics, University of Toronto, Toronto ON, Canada
[159] [(a)]TRIUMF, Vancouver BC; [(b)]Department of Physics and Astronomy, York University, Toronto ON, Canada
[160] Institute of Pure and Applied Sciences, University of Tsukuba, Ibaraki, Japan
[161] Science and Technology Center, Tufts University, Medford MA, United States of America
[162] Centro de Investigaciones, Universidad Antonio Narino, Bogota, Colombia
[163] Department of Physics and Astronomy, University of California Irvine, Irvine CA, United States of America
[164] [(a)]INFN Gruppo Collegato di Udine; [(b)]ICTP, Trieste; [(c)]Dipartimento di Fisica, Università di Udine, Udine, Italy
[165] Department of Physics, University of Illinois, Urbana IL, United States of America
[166] Department of Physics and Astronomy, University of Uppsala, Uppsala, Sweden
[167] Instituto de Física Corpuscular (IFIC) and Departamento de Física Atómica, Molecular y Nuclear and Departamento de Ingenierá Electrónica and Instituto de Microelectrónica de Barcelona (IMB-CNM), University of Valencia and CSIC, Valencia, Spain
[168] Department of Physics, University of British Columbia, Vancouver BC, Canada
[169] Department of Physics and Astronomy, University of Victoria, Victoria BC, Canada
[170] Waseda University, Tokyo, Japan
[171] Department of Particle Physics, The Weizmann Institute of Science, Rehovot, Israel
[172] Department of Physics, University of Wisconsin, Madison WI, United States of America
[173] Fakultät für Physik und Astronomie, Julius-Maximilians-Universität, Würzburg, Germany
[174] Fachbereich C Physik, Bergische Universität Wuppertal, Wuppertal, Germany
[175] Department of Physics, Yale University, New Haven CT, United States of America
[176] Yerevan Physics Institute, Yerevan, Armenia
[177] Domaine scientifique de la Doua, Centre de Calcul CNRS/IN2P3, Villeurbanne Cedex, France
[a] Also at Laboratorio de Instrumentacao e Fisica Experimental de Particulas - LIP, Lisboa, Portugal
[b] Also at Faculdade de Ciencias and CFNUL, Universidade de Lisboa, Lisboa, Portugal
[c] Also at Particle Physics Department, Rutherford Appleton Laboratory, Didcot, United Kingdom
[d] Also at CPPM, Aix-Marseille Université and CNRS/IN2P3, Marseille, France
[e] Also at TRIUMF, Vancouver BC, Canada

[f] Also at Department of Physics, California State University, Fresno CA, United States of America
[g] Also at Faculty of Physics and Applied Computer Science, AGH-University of Science and Technology, Krakow, Poland
[h] Also at Department of Physics, University of Coimbra, Coimbra, Portugal
[i] Also at Università di Napoli Parthenope, Napoli, Italy
[j] Also at Institute of Particle Physics (IPP), Canada
[k] Also at Department of Physics, Middle East Technical University, Ankara, Turkey
[l] Also at Louisiana Tech University, Ruston LA, United States of America
[m] Also at Group of Particle Physics, University of Montreal, Montreal QC, Canada
[n] Also at Institute of Physics, Azerbaijan Academy of Sciences, Baku, Azerbaijan
[o] Also at Institut für Experimentalphysik, Universität Hamburg, Hamburg, Germany
[p] Also at Manhattan College, New York NY, United States of America
[q] Also at School of Physics and Engineering, Sun Yat-sen University, Guanzhou, China
[r] Also at Academia Sinica Grid Computing, Institute of Physics, Academia Sinica, Taipei, Taiwan
[s] Also at High Energy Physics Group, Shandong University, Shandong, China
[t] Also at Section de Physique, Université de Genève, Geneva, Switzerland
[u] Also at Departamento de Fisica, Universidade de Minho, Braga, Portugal
[v] Also at Department of Physics and Astronomy, University of South Carolina, Columbia SC, United States of America
[w] Also at KFKI Research Institute for Particle and Nuclear Physics, Budapest, Hungary
[x] Also at California Institute of Technology, Pasadena CA, United States of America
[y] Also at Institute of Physics, Jagiellonian University, Krakow, Poland
[z] Also at Department of Physics, Oxford University, Oxford, United Kingdom
[aa] Also at Institute of Physics, Academia Sinica, Taipei, Taiwan
[ab] Also at Department of Physics, The University of Michigan, Ann Arbor MI, United States of America
[ac] Also at DSM/IRFU (Institut de Recherches sur les Lois Fondamentales de l'Univers), CEA Saclay (Commissariat a l'Energie Atomique), Gif-sur-Yvette, France
[ad] Also at Laboratoire de Physique Nucléaire et de Hautes Energies, UPMC and Université Paris-Diderot and CNRS/IN2P3, Paris, France
[ae] Also at Department of Physics, Nanjing University, Jiangsu, China
* Deceased